



LANCASTER UNIVERSITY
DEPARTMENT OF ENGINEERING

Surface Temperature Equalisation Through Automated Laser Vaporisation of Thick Film Electrical Heating Elements

Author:
JOSHUA INGHAM

Supervisor:
DR. DAVID CHENELER

*A thesis submitted in fulfilment of the requirements
for the degree of Master of Research*

January 2019



**Centre
for Global
Eco-Innovation**



European Union
European Regional
Development Fund

Dedication

Dedicated to my mother Suellen Ingham, father Michael Ingham, sister Rebekah Ingham, and partner Miriam Luft, without all their love and support this thesis would not have been possible.

Declaration of Authorship

I hereby declare that except where specific reference is made to the work of others, the contents of this dissertation are original and have not been submitted in whole or in part for consideration for any other degree or qualification in this, or any other university. This dissertation is my own work and contains nothing which is the outcome of work done in collaboration with others, except as specified in the text and Acknowledgements. This dissertation contains no more than 35,000 words including appendices, bibliography, footnotes, tables and equations and has fewer than 150 figures.

Joshua Ingham

April 2018

Abstract

The increasing proportion of energy used by electric heating devices creates an ever-growing demand for more efficient heating technology. This research project investigated the CO₂ laser ablation of partially oxidised Ni-Fe-Cr-NiO flame sprayed electrical heating elements in order to develop an automated system to optimise the surface temperature profile of thin film electrical heating elements. The optimisation technique used was the targeted local resistance change across the surface of a heating element's film so that the element temperature profile produced through the joule heating of the conductor is uniform and evenly distributed. Various surface treatment processing methods were developed that were used for the automated treatment of the element. These processing methods were compared and analysed through the standard deviation and kurtosis of the element's surface temperature distribution, the greatest improvement of all the processing methods showed a 71% reduction in standard deviation of the surface temperature distribution of the heating element.

Acknowledgements

Thank you for the guidance and inspiration from Dr. David Cheneler who kept me on track throughout the project and highlighted what was important.

Thank you to the team from 2DHeat LTD; Marcus Rutherford, John Lewis and Steve Keating, for their unwavering belief, positivity and drive in working with myself on this project and for their funding provided towards the project.

Thank you to Dr. Xingzhong Liang and Dr. Pedro Riviera who trained and allowed myself to use their optical microscopy and polishing facilities in the Department of Engineering at Lancaster University.

A grateful acknowledgement to Dr. Nathan Halcovitch and Dr. Sara Baldock who provided great assistance using the XRD and SEM in the Department of Chemistry at Lancaster and for their patience with the flurry of questions I asked.

Thank you to Dr. Alex Robson, who provided support and help in the microscopy of the material in collaboration with Lancaster Material Analysis Ltd.

This project was supported by 2DHeat LTD, the Centre for Global Eco-Innovation and is part-financed by the European Regional Development Fund.

A special thank you to my grandfather Stewart Ingham who provided me with a Linux development environment to carry out initial tests with the thermal camera.

Contents

1	Introduction	1
1.1	Background	4
1.2	Motivation	6
1.2.1	Environmental Benefits	6
1.2.2	Technological Benefits	8
1.3	Objectives	10
1.4	Organisation of the thesis	11
2	Literature Review	13
2.1	Flame Sprayed Heating Element Characterisation	14
2.1.1	Characterisation of the Alloy Particles Used for Flame Spray	15
2.1.2	Oxidation of Metals and Alloys	15
2.1.3	Prepared Powder for Flame Spray	16
2.1.4	Morphology of the Spray Material	17
2.1.5	Thermal Properties of the Element Components	21
2.2	The Heat Production through Joule Heating of Plane Conductors	22
2.3	Light Amplification Through Stimulated Emission of Radiation	24
2.4	Laser Beam Optics	26
2.4.1	Definitions of the Energy, Power and Fluence of Pulsed and Continuous Lasers	28
2.5	Laser Ablation of Solids	30
2.5.1	Absorption of Laser Radiation	30

2.6	Laser Ablation of Films	35
2.6.1	Material Change After Laser Irradiation	36
2.6.2	Surface Factors Affecting Laser Treatments	37
2.6.3	Laser Ablation of the Heating Element Film	40
2.6.4	Experimental Literature on the Material After Heat Treatments	42
2.6.5	Justification of the Choice of Laser for Further Experimentation	42
2.7	Model of Targeted Conduction Pathway Reduction of Conductors for Uniform Surface Joule Heating of Conductors	44
2.7.1	Laser Ablation for the Increase in Uniformity of Heat Output of the Element.	44
3	Methods	46
3.1	Optical Microscopy	46
3.2	X-ray Techniques	48
3.2.1	X-ray Diffraction	48
3.2.2	Energy Dispersive X-Ray Fluorescence	50
3.3	Scanning Electron Microscopy	51
3.4	Scanning Electron Microscopy with Energy Dispersive Spectroscopy	53
3.5	Optical Scanning Profilometry	55
3.6	Microscopy Sample Preparation	58
3.7	Resistance Measurement through the Four-Probe Method	59
3.8	Statistical Techniques	60
4	Experimental System Design Experiments	64
4.1	Properties of the intrinsic film	65
4.2	Surface Roughness of the Element	66
4.3	Preliminary Ablation Tests	68
4.4	Morphology Changes from the Interaction of the Laser and Film	74
4.5	X-ray Diffraction of Samples	77

4.6	SEM & EDX Microscopy	80
4.6.1	Summary of the Experimental System Design Experiments	85
4.7	Processing Method Design Model	87
5	Implementation of System Design	88
5.1	System overview	88
5.2	Infrared Thermography	90
5.3	Infrared Camera Integration	93
5.4	Infrared Camera Calibration	96
5.4.1	Flat Field Correction to the Thermal Camera	96
5.4.2	Temperature and Emissivity Calibration	96
5.5	Software Implementation	99
5.5.1	Image Acquisition	99
5.5.2	Image Processing	99
5.5.3	Selection of the Region of Interest	101
5.5.4	Image Distortion Calibration	102
5.5.5	Image Scaling	104
5.6	Laser Control Engineering	106
5.6.1	Laser Gantry Control	106
5.6.2	Software Path Control	107
5.7	Laser Processing	108
5.7.1	Laser profile	108
5.7.2	Laser Power Output and Delivery to Worktop	109
5.7.3	Mirror and Lens System	112
5.7.4	Mirror and Lens Radiation Transmission Efficiency	114
5.8	Accessory System Engineering	115
5.8.1	Laser Tube Cooling system	116

5.8.2	Ventilation System	119
5.8.3	Interlock Safety System	120
5.8.4	Element Electrical Connection and Clamping System.	121
5.8.5	Mirror Alignment	123
5.9	System Validation and Calibration	124
5.9.1	Depth of Pulsed Spots on the Material	124
5.9.2	Greyscale Pulsed Output Implementation	126
5.9.3	Time to Reach Steady State Investigation	129
5.10	Resistance Experiments	131
5.11	Maintenance of power output as element resistance changes	133
5.12	Laser-Treatment Processing methods	134
5.12.1	Abrasion baseline	134
5.12.2	20% Threshold (20%) Temperature Profile Measurements	137
5.12.3	50% Threshold (50%) Method	139
5.12.4	Greyscale (GS) Method	141
5.12.5	Greyscale-Threshold(GT) Temperature Profile Measurements	143
5.12.6	Greyscale Threshold + Memory (GM)	147
5.13	Processing Method Metrics	148
5.13.1	Resistance Change Through Various Processing Methods	152
5.14	Discussion of the Various Processing Methods	155
6	Conclusion	157
6.1	Further Work to be Done	163
A	Appendix	164

List of Figures

1.1	Image of the element surface produced by 2D Heat Ltd, the grey areas on the edges are silver contact paste, the larger, black region is the flame sprayed element.	2
1.2	The surface temperature of the thin film heating element with 3A and 6VDC applied across the ends of the element. Imaged with the thermal camera used within this project.	3
2.1	Ternary Ni-Cr-Fe phase diagrams of an isothermal section (650°C) and a liquidus projection respectively [13]	19
2.2	Fe-Ni-O and Cr-Ni-O pseudo binary phase diagrams [13] [14]	19
2.3	A model of a Gaussian beam width ($w(z)$) as a function of distance (z) along the beam with beam waist w_0 , the depth of focus b , Rayleigh range z_R and total angular spread θ [20].	24
2.4	A Gaussian beam profile, indicating a higher energy density from blue (lowest) to red (highest).	27
2.5	Diagram modelling the laser vaporisation process with plasma formation occurring at high laser intensities.	31
2.6	A diagram showing the internal reflection of light at interfaces of varying refractive indices	38
3.1	Example of the optical micrograph of a section of film with the metallic regions highlighted. Film thickness of 39 μm for the image scale.	47
3.2	Visualisation of the constructive interference of X-rays by an atomic lattice [42]. . .	48

3.3	Diagram of a XRD diffraction experiment.	49
3.4	A diagram of an electron beam interacting with a material and a visualisation of the resulting effects. Adapted from [45].	52
3.5	A diagram of a Scanning Electron Microscope in operation to image a sample [46].	52
3.6	Surface roughness parameters indicated on a profile plot of an arbitrary rough sample.	56
3.7	Diagram of the methodology of the resistance measurements of the element.	59
3.8	The plots of various distributions with mean 0, variance 1, and against the excess kurtosis where 0 excess kurtosis indicates absolute an kurtosis of 3). The normal distribution is labelled with an excess kurtosis of 0 and an absolute kurtosis of 3 as is the definition of the kurtosis [49].	62
4.1	An optical image of the cross section of the film after mounting and polishing. The film thickness was found to be $39 \pm 8 \mu\text{m}$	65
4.2	A 3D re-projection of the profilometer data of the surface heights across an 10x20mm section of the element compared against a mean level, heights not to scale with the width and length of the element.	67
4.3	A matrix of continuous wave carbon dioxide laser irradiation of the flame sprayed element at various speeds and powers of laser using the PIRANHA system.	69
4.4	Tabulation of the effect of the continuous wave laser on the material at various powers and speeds.	71
4.5	Tabulation of the calculation of the fluence (J/mm^2) applied to each spot size (0.2mm) within each experiment. The green coloured cells indicate the transition between damage cases from the colouration of the surface to light ablation of the surface, the yellow cells indicate the transition between light ablation and heavy ablation and the orange cells indicate the transition between heavy ablation and ablation all the way to the substrate.	72

4.6	An optical image of squares of ablation after mounting and polishing the upper surface. The fluence of each is shown in figure 4.5.	75
4.7	Optical images of the cross section of the film before ablation at the same magnification as 4.8.	76
4.8	Optical images of the cross section of the film after ablation. The ablated sections cut across the lines of ablation with the beam having a slight overlap in each line of ablation.	76
4.9	XRD results shown with the miller indices indicated for various shown species. A:Prepared Pre-flame sprayed powder, B: Flame sprayed element, C: Laser ablated element, D: Heavily laser ablated flake.	78
4.10	A SEM image of the raw surface roughness and four EDX elemental maps of the distribution of Ni O Cr and Fe on the rough sample.	81
4.11	A SEM image and four EDX elemental maps of the distribution of Ni,O,Cr and Fe of a polished sample of a raw element.	81
4.12	A SEM image and four EDX elemental maps of the distribution of Ni,O,Cr and Fe of a continuous laser ablated line at 25W at 300mm/s with a 0.2 mm spot size.	82
4.13	A SEM image and four EDX elemental maps of the distribution of Ni,O,Cr and Fe of two laser ablated rastered lines each at 25W and 300mm/s with a 0.2 mm spot size.	83
4.14	A SEM image and four EDX elemental maps of the distribution of Ni,O,Cr and Fe of a polished laser track ablated with a continuous laser at 25W and 300mm/s with a 0.2 mm spot size.	84
5.1	This diagram shows how each component communicates with each other to achieve the laser treatment of the element.	89
5.2	Flow chart showing how each process in one treatment cycle operates procedurally.	89
5.3	The apparatus of the thermal camera visualising the heating element, with the key variables in the spot size effect displayed.	91

5.4	Image of the infrared sensor and control circuit which is 2.2x3cm in size.	93
5.5	Graph of the pixel value of the sensor against the values measured by the spot thermometer and the Thermocouple with linear fits added.	97
5.6	Diagram showing the result and the area of influence of bicubic interpolation on a sample greyscale image.	100
5.7	Comparison of the images before and after lens calibration with the corners of the chequerboard indicated by the calibration algorithm.	103
5.8	Image showing the transformation of the thermal camera pixel coordinates to the laser coordinates.	104
5.9	A graph comparing the positions measured in the laser grid and the positions measured in the thermal image.	105
5.10	Laser path and gantry design without worktop placed within, the laser tube is roughly 1m in length with the gantry area encompassing 200x300mm.	107
5.11	Laser pulses onto acrylic media in a line set to only just overlap. Each pulse has a width of $0.13\text{mm} \pm 0.01\text{ mm}$ which corresponds to the beam width.	109
5.12	Graph displaying the power of the laser at various percentages of power selected on the manual power selection knob. Y-axis error bars due to the uncertainty from the power meter recording.	111
5.13	Transmission of infrared radiation through a ZeSe lens [58].	113
5.14	Components connected within the coolant system.	116
5.15	Components connected within the ventilation system.	119
5.16	A labelled diagram of the clamp system in operation.	122
5.17	Pulse overlap definitions are shown in the figure to illustrate the difference between the various overlap definitions.	124
5.18	A thermal image of the element is converted to a greyscale image with the greyscale adjacent to the temperature graph.	126

5.19	A diagram of a greyscale transferred into a pulse map with the corresponding translation between the greyscale and the gap between pulses illustrated.	127
5.20	The output of the conversion of the greyscale to a pulse map which is lasered onto an acrylic sheet.	128
5.21	The standard deviation of the temperature profile over time for an element heated through various heating techniques.	130
5.22	Resistance as a function of temperature normalised by the initial resistance. Error bars result from the uncertainty due to measuring high resistances leading to small voltages with the voltmeter at the range of	132
5.23	The Abrasion method is used to ablate element, contour plots of the surface temperature profile measurements shown after each cycle of ablation. The initial element is seen in the top left plot, reading from left to right in rows the element is ablated in each step, these are marked by numbers in the plots.	136
5.24	20% method used to treat element, contour plots of the surface temperature profile measurements shown after each cycle of ablation. The initial element is seen in the top left plot, reading from left to right in rows the element is ablated in each step, these are marked by numbers in the plots.	138
5.25	50% method used to ablate element, contour plots of the surface temperature profile measurements shown after each cycle of ablation. The initial element is seen in the top left plot, reading from left to right in rows the element is ablated in each step, these are marked by numbers in the plots.	140
5.26	Contour plots of the surface temperature profile measurements after each cycle of ablation using the Greyscale method. The initial element is seen in the top left plot, reading from left to right in rows the element is ablated in each step, these are marked by numbers in the plots.	142

5.27	The first repetition of the Greyscale - threshold hybrid (GH) method is shown in the contour plots of the surface temperature profile measurements shown after each cycle of ablation. The initial element is seen in the top left plot, reading from left to right in rows the element is ablated in each step, these are marked by numbers in the plots.	144
5.28	The Second repetition of the Greyscale - threshold hybrid (GH) method is shown in the contour plots of the surface temperature profile measurements shown after each cycle of ablation. The initial element is seen in the top left plot, reading from left to right in rows the element is ablated in each step, these are marked by numbers in the plots.	145
5.29	The third repetition of the Greyscale - threshold hybrid (GH) method is shown in the contour plots of the surface temperature profile measurements shown after each cycle of ablation. The initial element is seen in the top left plot, reading from left to right in rows the element is ablated in each step, these are marked by numbers in the plots.	146
5.30	The Greyscale - threshold hybrid method plus memory processing is used to treat the element. The result is visualised in contour plots of the surface temperature profile measurements shown after each cycle of ablation. The initial element is seen in the top left plot, reading from left to right in rows the element is ablated in each step, these are marked by numbers in the plots.	147
5.31	The standard deviation of the element after ablation relative to the unablated element.	151
5.32	The kurtosis of each element after each cycle of ablation from various processing methods.	152
5.33	The electrical resistance of the device after ablation by the Greyscale Hybrid method in multiple trials with an averaged line added.	154
5.34	The electrical resistance of the device after each iteration of ablation by various processing methods.	154

List of Tables

2.1	Thermodynamic Material Parameters of the Components of the Flame Sprayed Element	21
2.2	Electrical Material Parameters of the Components of the Flame Sprayed Element . .	23
4.1	Scanning probe measurements of the average surface roughness of the unablated element.	66
4.2	Characterisation of damage to the film surface from the continuous wave laser ablation matrix	69
4.3	XRD results summary of the proportion of various compounds on various materials investigated.	77
5.1	Power output data of the laser tube.	115
5.2	Average depth of pulses ablated onto the film with various overlaps at 2.26 J cm^{-2} , 30 μs pulse, 0.13mm spot size.	125
5.3	Summary of the differences between the processing methods.	135
5.4	The performance metrics of the various processing methods used to compare the total improvement of the temperature profile from the initial element to the optimised profile.	149
5.5	Change in resistance per cycle for various ablation processing methods	153

Chapter 1

Introduction

There is considerable interest into environmental and engineering advantages of improvements to conventional electric heaters. 2D Heat Ltd manufacture metal oxide films that are flame sprayed onto surfaces. The film is formed from an Inconel 600 powder through a flame spray process with the main constituents of Ni-Fe-Cr-O. The film as deposited on a stainless steel substrate on top of an aluminium coating is shown in figure 1.1. Due to the flame spray process, the oxidation of the film is much higher than predicted by the initial metallic Inconel 600 powder. This increases the electrical resistance of the film making it suitable for the incorporation in an electrical heating device such as an electric heating element.

The main advantage of film elements over other electric heating technology is a higher efficiency of heat transfer from the element to the surroundings through reducing the unwanted heat loss to convection and conduction. Due to the current flow through the conductor the element has a hot spot centred on the central region of the element. Figure 1.2 shows the surface temperature profile of an element produced by 2DHeat LTD. It can be seen that the heat profile of the element is non-uniform with a hot spot in the centre.



Figure 1.1: Image of the element surface produced by 2D Heat Ltd, the grey areas on the edges are silver contact paste, the larger, black region is the flame sprayed element.

The goal of the project is to reduce the hot spot size and increase the uniformity of the heat output of the heating element. Currently, the technology is not integrated within any existing technology. By improving the accuracy, and precision of the heat output of 2D Heat's thin film heaters the hope is that the technology becomes more attractive to industry, allowing it to be integrated into existing products.

Various commercial interests have approached 2D Heat LTD such as washer, dryer, and space heating manufacturers as well as interest has even been shown from the large hadron collider at CERN. An application of the technology they are interested in is the application of the film on the beam line vacuum vessels as an integrated heating solution in the 'bakeout' stage when the vessel is purged to a vacuum. This would offer improvements to the energy efficiency, time, and effectiveness of the 'bakeout' process. The development of an automated, reliable and reusable manufacturing process which produces heating elements with high uniformity of heat production and temperature distribution would allow the company to meet this growing demand.

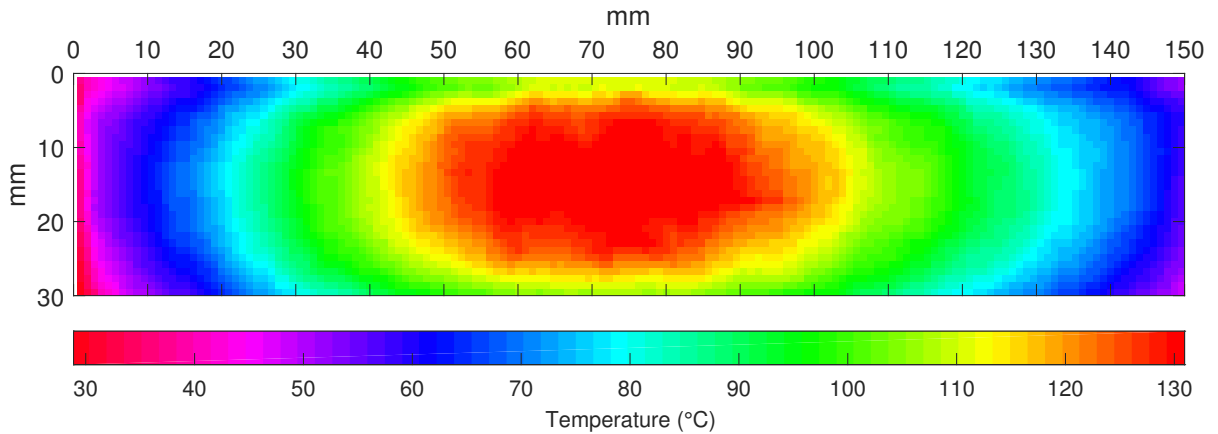


Figure 1.2: The surface temperature of the thin film heating element with 3A and 6VDC applied across the ends of the element. Imaged with the thermal camera used within this project.

This piece of work is part of the current paradigm shift to industry 4.0 which signifies the fourth industrial revolution. The first revolution was mechanisation and steam power, second the invention of electricity and mass production, third the automation of processes, and the fourth defined as integration of cyber-physical systems using AI (artificial intelligence) to monitor physical processes and making decisions on how to optimise a process without human intervention.

This relies upon the interconnection of sensors and tools, collection of data and information from multiple points in the manufacturing process, and decentralisation of decisions within the computer [1]. This project lies on the periphery of this shift through the integration of sensor technology and control automation so that the laser device makes its own decisions on the path and amount of treatment delivered to the element based upon the surface temperature profile recorded by a thermal camera.

1.1 Background

The panels are produced through a flame spray process, which is a process where the powder to be attached to the surface is heated and oxidised within a flame. Through the high pressure and temperature of the powder flow, it adheres to the surface it is being sprayed upon. Through utilisation and optimisation of this process, 2DHeat LTD produce thick film samples of the film on a variety of sizes and geometries from small rectangles to large squares and cylinders.

The powder used within the flame spray process is a Inconel powder (Inconel 600) with approximately 75wt% Ni, 15wt% Cr, 10wt% Fe ($\pm 5\%$) with particle size $25\ \mu\text{m} \pm 23\ \mu\text{m}$ [2], as the powder is sprayed onto the substrate the powder is atomised by the spray, this leads to an in-homogeneous coating as there is a wide range in particle size and morphology.

Each coating layer is approximately $20 \pm 10\ \mu\text{m}$ with multiple coatings added to the surface until the desired thickness is reached. This research has been inspired by the technical obstacle that when a load is applied over the heater, there is a variation in the temperature profile of the heater. The general morphology of this profile is a hot spot usually centred over the central region of the element surrounded by a colder region on the periphery of the element.

Even if all parts of the element produced heat in an exact uniform way it would be expected the temperature profile would have a pattern like this as there is a greater amount of heat loss on the periphery than the centre of the element. This means that the processing method must take into account the thermodynamic load due to the element geometry and structure as well as the heat output. This is achieved by using the temperature profile as the optimised parameter for the processing method thus taking the device thermodynamic geometry and heat output into account.

Initially to reduce the hot spot and increase the uniformity of temperature profile an abrasion technique was developed. This process increases the uniformity of the temperature profile by removing material manually by rubbing abrasive paper along the edges and cold regions of the element. This reduces the thickness of the conductor in that section and as the resistance of a conductor is proportional to its cross-section, the power output and thus temperature profile in that region increases.

The main disadvantage to this process is that it is manually intensive as an experienced technician must analyse each unique temperature profile and the process is time intensive due to the switching on and off of the element and the intermittent time it takes for the element to cool down. It is sought within this research to automate this process of analysis and material removal. It has been specified by the sponsors that a laser treatment is to be investigated to accomplish this goal. The advantages of using a laser machine are it is fast, creates reproducible results, and the element can be kept live whilst being processed. Thus the researchers agree that a laser system is suitable for the automation of this process.

The cycle of automation starts with the powering on of the heating element and the collection of infrared images of the element surface, this data is analysed and a processing algorithm is used to create a path for the laser to treat the surface. After the laser treated the surface, the process repeats itself until the improvement in the standard deviation and kurtosis of each part of the element in each processing cycle has plateaued or falls within a set value.

1.2 Motivation

1.2.1 Environmental Benefits

This project's funding was associated with the research and development of devices that can reduce the emissions of greenhouse gasses. As a result it is pertinent to analyse the environmental benefits of the heating element technology being optimised and how it fits into the general scheme of heating element technology.

In 2017, 75.4% of all energy consumption (excluding transport) was used for the production of heat within the United Kingdom and Northern Ireland [3]. 13% of this heat was produced through electricity, the remainder through a combination of gas (68%), oil (8%), solid fuel(3%), bio-energy and waste(8%) [3]. Electricity is the only component of which a proportion of the energy was derived from low carbon production such as renewable and nuclear energy.

In 2018 the International panel on climate change published a special report on the recommended steps to limit global warming to less than 1.5°. The report states that if this limit is reached there will be catastrophic consequences to the environment. One of the key recommendations was to limit 'net global emissions of long-lived greenhouse gases' including carbon dioxide to zero before the 1.5° limit is reached [4]. Since such a high proportion of the energy utilised within the UK & NI is used in heat production and a low proportion of the energy used in heating operations is produced without the release of greenhouse gasses, the proportion of heat produced through electrical heating must increase significantly to reach the target of zero net global emissions by the 1.5° target.

The greenhouse emissions produced through the production of electrical energy depend upon mixture of electricity production techniques used to provide power to the grid. In 2017 low carbon generation (nuclear and renewables) accounted for 50.4 % of the overall power generation. Additionally, this was a record proportion of low carbon power generation with the proportion of low carbon generation to be increased in the future [5].

Due to the large amount of energy consumed in heat production, the trend towards a more green mix of electricity generation and the low proportion of electricity currently used to produce heat, there is a growing need within the market for electrical heaters. In order to fill this void, new technologies are required that are more efficient, maintain a low economic and environmental cost of production, and have a high engineering versatility such that they can readily be integrated into and replace existing technologies.

One way to reduce the amount of energy produced is decreasing the consumption and losses of energy; Governmental projects have focused on the increase of efficiency of devices and decrease of energy loss. One example is the subsidisation of cavity wall insulation in homes. These projects have been successful, shown by the low growth of energy consumption over the last 20 years[3]. It is forecast that currently 87% of buildings will have improved their Cavity wall insulation to a high standard in the UK. Therefore, in order to deliver the IPCC 1.5° degree target and to limit the growth in energy consumption, the deliverance of more efficient technology is required.

1.2.2 Technological Benefits

Heating elements are usually made from wires or coils of wires and are encased in thermal blocks so heat diffuses from the high temperature wire inside [6]. Due to the high temperature of the wire and its small size it emits heat in a non-uniform fashion and reaches high temperatures (500°C - 1000°C) [6]. Due to the large sizes of the aluminium blocks, it takes a long time for the heater to get to their working temperature (40°C-50°C). Thus consumers then tend to over heat homes through the over driving of the electrical element as the element is slow to reach working temperature and to cool down after deactivation. Furthermore, the temperature of the block needs to be carefully controlled by turning the heater on and off so it does not overheat due to the high temperatures of the wire heater.

Flat panel heaters aim to eliminate this factor by reducing the thermal mass of the heater. Due to the engineering design of these elements, there is usually a coil or pattern of a resistor arranged in an array on the panel surface. This does not produce uniform heat so the heater tends to be turned higher than it would need to be and there is large uncertainty in the temperature of the panel. In addition, a considerable gap between the element and the heated surface needs to be implemented so the device is not too hot to touch. Due to the gap between the element and the surface there is heat loss through convection of heat throughout the heating circuit.

2D Heat LTD have produced a thick film coating that, when a power source is connected to either side of its coating, increases the coating temperature through joule heating. The thermal mass is orders of magnitude smaller than existing technology meaning that once the heater is on it is at its operational temperature. As a result, the time to reach working temperature is between 2-4 minutes. This lowers the time needed to get to the working temperature and subsequently is more efficient in switching between the on and off stages resulting in more efficient use of the device.

The heater delivers the heat over a large area and there is a large degree of controlling the element, which means the heater temperature can be selected more accurately. This reduces the energy use of the heater as the temperature of the heater can be selected more accurately. In addition to providing more efficient heat delivery, there has been interest into these devices from companies looking to provide heating processes within their designs. Such interest has been shown from the vacuum beam line, kitchen appliances, and transport industries.

Respective examples of their use is for the baking out stage of accelerator beam lines, cooking facilities, and for efficient heaters in electric cars. The advantages for these industries are overcoming some of the geometric limitations of conventional heater technology, replacing existing gas driven technology, improving the safety of current products, and improving the uniformity of the heat output.

1.3 Objectives

The goals and objectives for this body of research are listed below:

- Research the effect of lasers on the target material's morphology, resistance, and heat profile.
- To establish the power and duration of laser treatment to improve the heat profile of the heating element.
- To establish techniques of mapping the heat profile of the heating element.
- To create a processing method to alter the heating profile to create a high degree of uniformity of the temperature profile across the element surface.
- To produce an optimised system that accomplishes all the outputs above with the system parameters of being quicker than the previous ablation method, more accurate and with a higher uniformity of temperature profile, with as closed a system loop as possible.

1.4 Organisation of the thesis

Initially the thesis considers the morphology and composition of the flame sprayed element through analysing its manufacture process and constituents in the context of previous literature on similar or same materials. Then various properties of the elements constituents are analysed with respect to their electrical, thermodynamic and optical properties. Then the theory of how laser beams are produced and the optical engineering of lasers is analysed so that the design of laser systems can be understood. Next the theory of laser-material interactions are investigated with a focus on the laser interaction of carbon dioxide lasers with metal / metal oxides.

Finally the heat production of the heating element due to joule heating is considered with the goal of creating a model of laser-material interaction leading to the local resistance change of the element to produce a uniform temperature profile of the element whilst producing heat through joule heating. A methods section is included that analyses the various microscopy techniques used in the project.

A laser processing strategy was developed that states how the laser system treats the element in each region that is selected for treatment. To develop this system design experiments took place. These are discussed in the system design experiments section and investigate the various processes of laser and material interaction such as the increase in oxidation and ablation of the surface. The laser processing strategy is used to form the basis of change on the element.

Then a stand along laser-infrared camera system was developed to fit the parameters specified by the processing strategy. The development and verification of this systems functions and capability is thoroughly documented within the thesis. Several processing methods are then constructed to identify the optimal areas and level of treatment to be delivered to the element.

These are explained and then discussed within the section on processing methods. Through experimental tests of each processing method and analysis through recording the data of the validity, performance metrics and statistical improvement to the element, which in turn allows for the evaluation of the processing methods. Finally this culminates in an conclusion of the whole project with respect to the aims set at the outset of this thesis.

Chapter 2

Literature Review

There are three core topics reviewed within the literature; Firstly, flame sprayed films, followed by the theory of laser ablation, and thirdly the theories behind the production of heat by electrical heating. This is done to provide the necessary background to the project and the theoretical models which were used within the project and which are referenced later within the research to enhance the conclusions of this work. The areas that are reviewed are the characteristics of the flame sprayed element before ablation, how do materials and this material specifically react to laser ablation with a focus on infrared irradiation.

2.1 Flame Sprayed Heating Element Characterisation

There are two stages in the manufacture of the films, the preparation of the powder and the deposition of the powder. Each stage involves the use of powder within a flame spray process. The preparation stage is where the initial powder is oxidised by a flame spray, quenched and then collected. The second stage is where the powder is deposited onto a substrate using the flame spray[7]. For the utilisation of this flame spray process, the sponsor of this research, 2DHeat Ltd, have developed a primarily nickel/nickel oxide coating. This research will refer to the four forms of the film, namely the base material powder, the prepared powder, the flame sprayed film, and the laser ablated film.

The thermal spray method used for the manufacture of these elements is defined as flame powder spraying. A powder is fed into an oxyacetylene-fuel flame so the powder undergoes melting, oxidation, and atomisation and is carried by a mixture of flame and carrier gases to substrate.

Particle velocity is generally less than 100 ms^{-1} , as a result cohesion between the particles and bond strength on the substrate is low, which also introduces voids into the film [7]. Since this project focuses on the optimisation of a company's existing product, changes are not made to the powders or manufacturing process before processing with the laser ablation system so that manufacturing conditions were closely replicated.

2.1.1 Characterisation of the Alloy Particles Used for Flame Spray

Previous research has been extensively done on the flame sprayed film by Duffield(2017) [2], whose research provides much of the initial theory on the properties of the sprayed powder. A powdered alloy (Inconel 600) is the base material for the manufacture of the films. This alloy, before flame spray, is characterised as a powdered Ni-Cr-Fe alloy (approximately 75wt% Ni, 15wt% Cr, 10wt% Fe) [2].

The material science, whilst very complex, has had some in depth examination through work done by Duffield(2017) on these films and powders . They found the particle size distribution through image analysis of the original alloy particles at $25\mu\text{m} \pm 23\mu\text{m}$. Through X-Ray diffraction (XRD), the initial powder was found to have a majority of alloy phases with a small quantity of NiO formation with a calculated lattice parameter of 4.17 \AA . This matches with other research into more pure samples of NiO [8].The base powder used to make the elements in this research is the same powder that Duffield examined, hence their conclusions also apply to this work.

2.1.2 Oxidation of Metals and Alloys

Within the project, a considerable amount of interest is focused on the oxidation of the base alloys as they are the primary factor affecting the resistance of the material. The oxidation of nickel is spurred upon by the migration of cations and electrons from the metal interface to the metal oxide interface, growing topotactically. NiO growth occurs parabolically with the limiting factor on the rate of growth being the diffusion of Ni cations through the oxide layer.

This has been confirmed by Mrowec and Grzesikin (2004) showing that, at temperatures over 1000°C, results within literature generally conform to this model of oxide growth [9]. Through examination of markers at the metal and metal oxide interface, they observed that Ni cations were diffusing outwards throughout the oxide. In addition, experimental parabolic rate constants for nickel oxidation were found to agree with theory.

However, when lower temperatures are considered, the oxidation mechanisms are more complicated. This is due to oxidation no longer following Wagner's theory of oxidation [10]; in some cases rates were found to be over one hundred times higher than predicted [11].

A hypothesis for this is the grain boundaries and dislocations causing 'short circuits' of higher areas of oxide formation [11]. This was found experimentally via the use of isotope markers in the range 500-1300°C where violations to the parabolic oxidation law were observed [11]. This provides evidence that within the thermal processes of the laser treatment, the oxidation within the heat affected zone is likely to increase.

2.1.3 Prepared Powder for Flame Spray

The prepared powder is the powder that is used for the flame spray process. This powder is formed from the base alloy after an oxidation step. The preparation of the powdered alloy consists of increasing the oxidation of the original powder. During this process no other powders are mixed into the original powder. It was found to have a size distribution of $36 \mu\text{m} \pm 20 \mu\text{m}$ which is larger than the base alloy powder, indicating oxidation and structure formation in the powder. Additionally, Duffield found that within the prepared powder, there are still regions of the base alloy present in addition to the oxidised prepared powder, indicating that not all the powder is altered by the preparation step.

For this powder, Duffield used XRD to prove this assumption, a value of the lattice parameter of 3.56 Å) for the Nickel Oxide as well as low alloyed Ni (lattice parameter 3.53 Å). The weak peaks Duffield found indicate a small amount of spinel phases (lattice parameter 8.33 Å) present. Through comparing to other work done on thermal spraying processes, this type of in-homogeneous powder is typical for flame spray material [7].

It is reasonable to consider the conclusions of Duffield(2017) to be appropriate for this project as the samples used in this project are similar to the samples Duffield(2017) investigated and produced under similar conditions. In addition, data is compared to Duffield's data to show where deviations to his data were found.

2.1.4 Morphology of the Spray Material

To characterise the material after flame spray deposition Duffield (2017) used X-ray diffraction and SEM-EDS, which showed a high percentage of Cr and Fe doped NiO as well as the original alloy and low alloyed Ni in addition to a spinel phase. Approximately 62% oxide, 17% metal and 21% voids were recorded by Duffield (2017), using image analysis of the cross section of the film. They then compared the results of the X-ray diffraction patterns to the powder before flame spray, this data suggested that the phases detected in the prepared powder remained present.

The X-ray diffraction data suggested that the metallic material accumulated preferentially during deposition as there was an increase in the peaks of the metallic regions in the diffractogram from XRD. Through work with TEM/STEM analysis they also found an increase in the spinel phase throughout the films compared to the initial base alloy, prepared particles, and flame sprayed material.

Through optical examination of the cross section of the films, they show a variety of morphology in the material. The film has a combination of columnar and equiaxed grain structures cultivated by the temperature difference in flame spray processing [2]. It is characterised as molten particles flattening upon impact and forming columnar grain formations, more solid particles deform less during the deposition process which produces a more equiaxed grain structure in this region[12].

Due to the variance in the processing of the particles in the flame spray process there is a variety of deformation within the film, this is shown most clearly by examining the metallic regions in the film. Due to the variance in the path and temperature experienced by each particle there is a variety of morphology in the film. The particles with a lower temperature at impact and higher metallicity were found to form a spherical morphology in the film. The higher the temperature and the lower the metallicity of the particles, the greater the amount of material that is dispersed upon collision with the substrate.

This led to a more 'milky splat' as the NiO and metallic regions develop better bonds with the material nearby[2]. In addition to the more macro-microscopic morphology, they found microscopic morphology of oxide particles distributed within the metallic regions, and metallic particles dispersed within an outer oxide shells [12].

Duffield (2017) found that the increased intensity of the metallic diffraction peaks relative to the oxide peaks indicate the preferential accumulation of metallic phases during flame spray. He attributed this difference between the metal and oxide deposition rates to the disparity in the materials' melting temperatures.

The proposed mechanism is through a higher proportion of the metallic particles reaching the substrate surface in molten or softened states, deformation and therefore greater bonding efficiency is experienced by the metallic particles so more metallic regions are bound by the prepared powder.

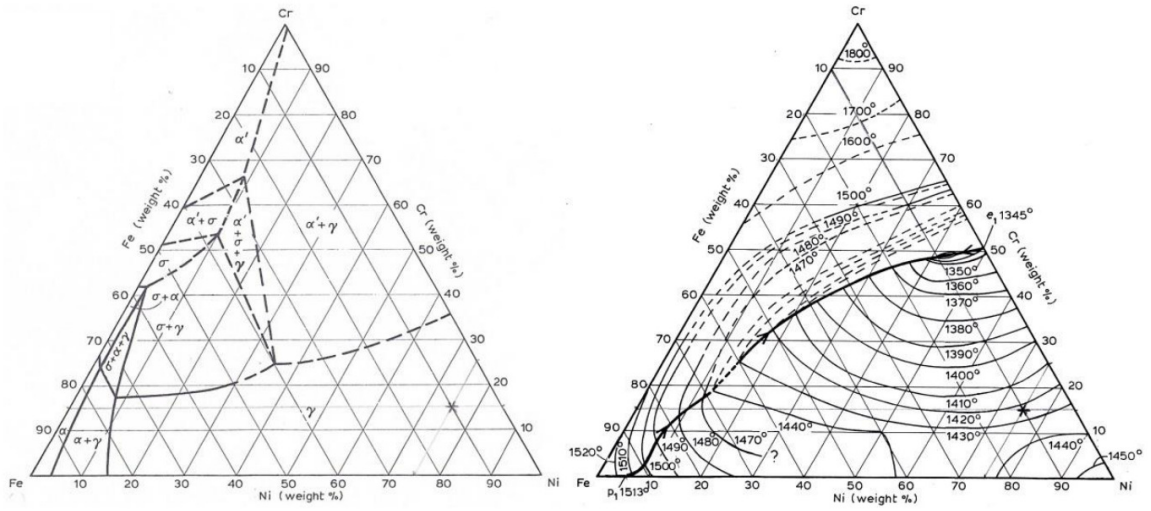


Figure 2.1: Ternary Ni-Cr-Fe phase diagrams of an isothermal section (650°C) and a liquidus projection respectively [13]

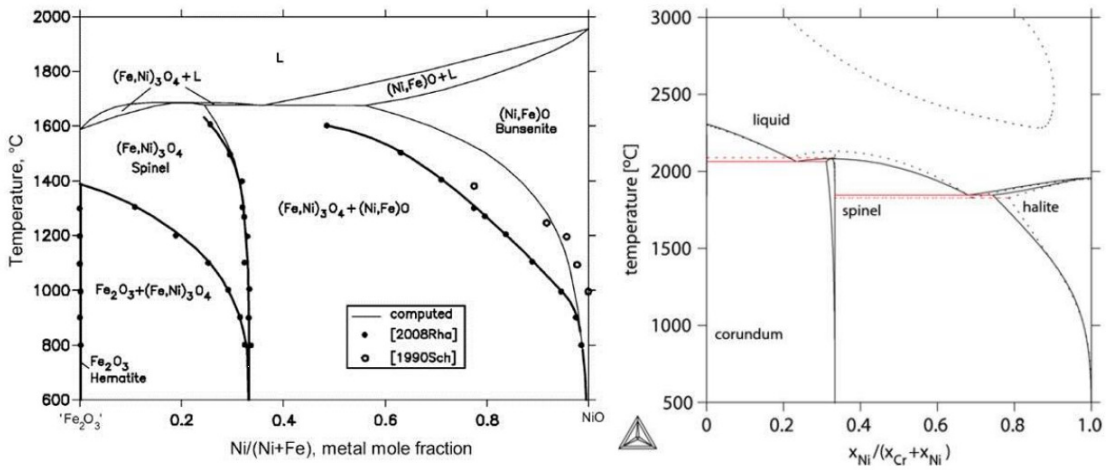


Figure 2.2: Fe-Ni-O and Cr-Ni-O pseudo binary phase diagrams [13] [14]

After the flame spray of the prepared powder, more phases are detectable by XRD. Duffield (2017) found the dominant phase with a NaCl crystal structure comparable to that of NiO. He calculated the lattice parameter of 4.17 Å which is 0.2% off the NiO data file value of 4.178 Å [8]. Duffield also found regions of Ni, Fe and Cr metallicity as well as a spinel phase in low proportion. Within the initial powder there is a variety of elements present but only the three distinct regions can be separated of metallic regions, oxide regions and spinel phase.

This is due to the similar lattice parameters of the Nickel, Iron, and Chromium. Another reason for a lack of iron oxide and chromium oxide in the XRD diffractogram is that the nickel oxide matrix can integrate appreciable quantities of Fe and Cr at high temperatures. This is evident as the Ni-Fe-O [13] and Ni-Cr-O [14] phase diagrams suggest that NiO integrates large quantities of Fe and Cr at high temperatures within the range of parameters in the flame spray process.

The pseudo-binary Ni-Fe-O and Ni-Cr-O phase diagrams (see figure 2.2) was published by Raghavan (2010) [13] and Kjellqvist (2008) [14] respectively, this suggests that NiO can integrate Fe and Cr at high temperatures (conditions similar to oxidation treatment by flame and laser treatment). Fe and Cr have similar ionic radii to Ni [15] therefore can replace Ni atoms in the oxide lattice whilst not significantly altering the lattice parameter. Due to rapid quenching in the thermal spray process, this state can be maintained at room temperature as kinetics limit phase transformation at the low temperature state [11]. High temperatures and quench rates are also found in laser treatments, this indicates that laser treatments can maintain and even grow these phases too.

Table 2.1: Thermodynamic Material Parameters of the Components of the Flame Sprayed Element

Quantity	Nickel	Iron	Chromium	Nickel Oxide
Melting point °C	1400	1800	1900	2000
Thermal Conductivity ($\text{Wm}^{-1} \text{K}$)	90	55	90	15
Density gcm^{-3}	8.9	7.9	7.2	6.7
Specific heat capacity ($\text{Jg}^{-1} \text{K}^{-1}$)	0.444	0.440	0.4	0.7

2.1.5 Thermal Properties of the Element Components

To investigate the thermodynamics of the system, the melting and boiling points, thermal conductivity and density of the various components of the film need to be compared. Table 2.1 compares these parameters. The values for the melting points of the elements and thermal conductivity is given through the Engineering toolbox [16].

This data has been collated from a review of other publications for the use of Engineers and scientists. This allows this research to make qualitative arguments and comparisons of the morphology changes seen later within the thesis. The vast difference between the components is the melting temperature. The metallic Nickel has the lowest melting point with the Iron and Chromium having higher melting points, and the Nickel Oxide having the highest melting point.

From these comparisons, the component most affected by the laser should be the Nickel with effects onto the Iron and the Chromium and Nickel Oxide respectively. The metallic portions show a much higher thermal conductivity than the Oxide; the laser treatment could affect the oxidation of the samples when the laser is irradiating the material, which might then drastically affect the thermal diffusion when the element is used as a heater.

2.2 The Heat Production through Joule Heating of Plane Conductors

The film is designed as a heating element. The projects goal is to increase the uniformity of the heat output of the films when they are used as heating elements. The primary method of heat production of the elements in joule heating in the conductor by a electrical power input. This section considers the theory of how this heating originates and then generates a theoretical model of how with a targeted laser treatment the films heat output uniformity can be increased.

The conduction in solids of electrons in an electric field is given by equation 2.1 where the current density \mathbf{J} is determined by the conductivity δ and the applied electric field \mathbf{E} . The current density \mathbf{J} is defined as the electric current per unit area of the cross section of the current path.

$$\mathbf{J} = \sigma \mathbf{E} \quad (2.1)$$

Where:

$$\sigma = \frac{1}{\rho} \quad (2.2)$$

The production of heat by a homogenous conductor originates from voltage difference between two ends of a conductor, this creates an electric field accelerating charge carriers. Their kinetic energy causes the charged particles to collide with ionic lattices and ions in the conductor, the particles become scattered as a result and the ionic lattice vibrates thus constituting thermal motion [17]. If this energy is converted into thermal energy the heat produced is proportional to the product of the current density and the applied electric field, this is combined with the definition of current density which yields 2.3.

Table 2.2: Electrical Material Parameters of the Components of the Flame Sprayed Element

Quantity	Nickel	Iron	Chromium	Nickel Oxide
Resistivity nΩm	69.3	96.1	125	548

$$\frac{dP}{dV} = J^2 \rho \quad (2.3)$$

This shows that the amount of heat production at a point is proportional to the current density squared times the resistivity. The two primary components of the material under investigation are the metals (Ni,Fe,Cr) and oxides (NiO, Iron Oxide, Chromium oxide).

These follow the conduction law above but will contribute different factors to the conductivity. Table 2.2 shows the resistivity of the various components in the film. The Nickel has the lowest resistivity out of all the components and the Nickel Oxide has a resistivity much larger than the other components.

The lowest resistance is found in the Nickel components. Therefore the nickel component will have the largest current flowing through it from equation 2.1. The resistance of the Iron and Chromium is much lower than the resistance of the oxides thus they will have some current flowing through but on a lower relative magnitude than the Nickel component. This means the metallic regions will contribute the greatest amount to the heat production of the element.

Thus through this model it can be determined that the metallic regions are the primary current carriers and the reduction in the metallicity of the film and the increase in oxidation leads to a increase in resistance. This is confirmed through the studies of the resistance of the film and the comparisons of NiO in increasing oxidation [18].

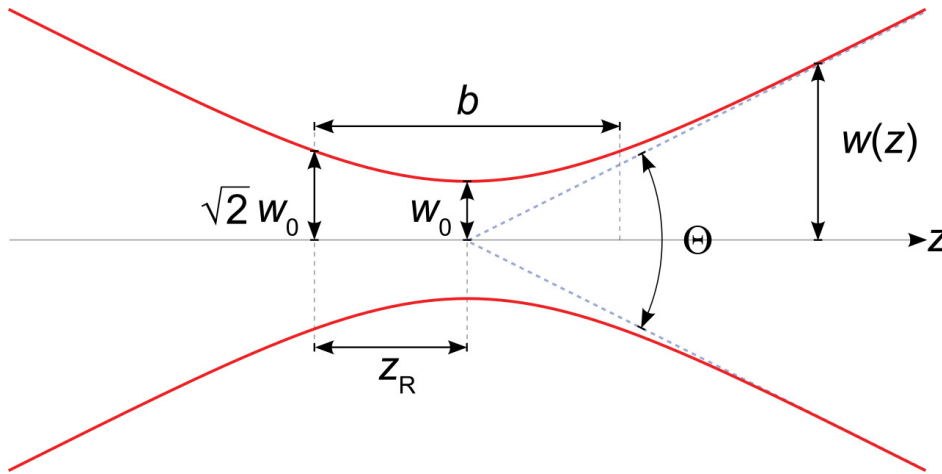


Figure 2.3: A model of a Gaussian beam width ($w(z)$) as a function of distance (z) along the beam with beam waist w_0 , the depth of focus b , Rayleigh range z_R and total angular spread θ [20].

2.3 Light Amplification Through Stimulated Emission of Radiation

The central component of the lasing process is the laser resonator, also known as the laser tube. This houses the gasses and mirrors used for the lasing process, within a CO₂ laser, the main focus of this research, these are CO₂ N₂ and He gasses. The CO₂ laser was the laser chosen to be incorporated within this project, this is justified as the carbon dioxide laser is one of the most economical lasers on the market currently offering the highest lasing power at low monetary costs [19].

The main component in the tube is the gas chosen for lasing, this is known as the gain medium, for a CO₂ laser this is an isotope of CO₂, this affects the lasing efficiency and the laser wavelength [21].

The initial change in the state of the laser is induced through stimulation by an electric potential between the cathode and anode on the ends of the laser tube. This excites the molecules in the pumping medium (for CO₂ lasers: N₂), subsequent collisions between the ions and electrons in the discharge current excite further atoms onto various energy levels. The ratio between the Nitrogen to Carbon Dioxide is around 4:1 [22].

Lasing gasses are chosen so that there is a collection of energy levels within the gasses in the laser tube suitable for lasing in the correct proportions to maximise the efficiency of lasing. The basic criteria for this are the following; the need for a higher energy level with a short lifetime, a medium energy level with a long lifetime and a lower energy level with a short lifetime. This makes the inversion of the population of the energy levels by electrons possible, which describes the state when there are more electrons in the medium energy level than the lowest and highest energy level due to the difference in their decay rates.

As the photons are emitted from the medium and are reflected along the silvered mirrors at the edge of the laser tube, the population of the medium energy level is the most populated energy level. These electrons then either fall to the lower energy level or to the ground state emitting photons. This produces monotonic light in parallel rays of high intensity.

The side of the laser tube from which the light radiates has a half silvered mirror, this allows for the lasing process to continue and for the laser light to escape the tube and be directed to the work-piece. This process continues until the electric discharge at the start of the process ceases [23].

2.4 Laser Beam Optics

The laser beam has various optical properties that are important to be considered for the laser system so that it is designed to deliver optimal performance for the laser vaporisation of the element. Throughout this research, the beam is modelled around a Gaussian beam.

A Gaussian beam has the properties of being well approximated by Gaussian functions and the amplitude profile width is determined by the waist w_0 of the beam [23]. There are various modes of the laser profile which are variations in the shape of the intensity profile of the laser, the only mode that is Gaussian is the TEM₀₀ mode, which is the mode explored in this theoretical investigation and was used within the project [23].

$$I(R, Z) = \frac{2P}{\pi w(z)^2} \exp(-2 \frac{r^2}{w(z)^2}) \quad (2.4)$$

The equation describing a Gaussian beam is shown in equation 2.4 [19]. The intensity $I(R,Z)$ at depth Z and radius R is proportional to the product of the ratio of the power (P) to area of beam (πw^2) which decays exponentially by the ratio of the beam width ($w(z)$) and the squared radial distance from the centre axis of the beam (r).

The propagation of a Gaussian beam described by equation 2.4 is visualised in figure 2.3 and an image of the energy density of a Gaussian beam in cross section at the interaction with an interface is shown in figure 2.4 [24].

The image in figure 2.3 shows a Gaussian beam width ($w(z)$) as a function of distance (z) along the beam. The beam waist w_0 is defined by the distance from centre of the beam to the point where peak intensity has decreased to $1/e^2$. The depth of focus b , Rayleigh range z_R and total angular spread of beam θ are also indicated in the figure.

$$w(z) = w_0 \sqrt{1 + (z\lambda/\pi w_0^2)^2} \quad (2.5)$$

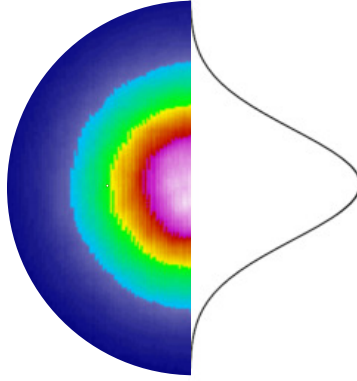


Figure 2.4: A Gaussian beam profile, indicating a higher energy density from blue (lowest) to red (highest).

When focusing the laser through a focusing optical aperture like a lens, the beam profile can change. The minimum width of the beam focused through a lens defined as $2w_0$ is given by equation 2.6, where F is the focal length of the lens, λ is the wavelength of light and D is the diameter of the beam incident on the lens [19]. When this equation is applied to the 50.8 mm focal length Plano-convex lens, used within this project with a $10.6 \mu\text{m}$ beam, the minimum spot size is 0.08 mm.

$$2w_0 = \frac{4\lambda}{\pi} \left(\frac{F}{D} \right) \quad (2.6)$$

The depth of focus of the lens b is found from equation 2.7. Using equation 2.7 to find the depth of focus for a 50.8 mm focal length Plano convex lens to $10.6 \mu\text{m}$ wavelength of light, gives a range of 2.54 mm with a focused spot size of 0.08 mm. Thus the variance in the work-piece height at the focal point of the lens must vary within this range so that the energy density applied to the surface is constant.

$$b = \frac{2\pi w_0}{\lambda} \quad (2.7)$$

2.4.1 Definitions of the Energy, Power and Fluence of Pulsed and Continuous Lasers

Many laser system properties are tuned to their application, a specific quantity of the laser system that is often controlled is the time period of the laser pulse. These can range from femtoseconds (10^{-13} s to nano and micro seconds in the applications in laser ablation treatments [25].

These are generally classed as ultra short for time periods below nanoseconds and short pulses for nanosecond and microsecond pulses. This research will concentrate on short pulsed lasers in the micro second range and continuous laser ablation. Whilst ultra-short lasers are regarded as better suited for laser ablation applications with the ability to interact with areas with a minimised heat affected zone they are also expensive and thus outside the budget of this project.

The energy per pulse of a pulsed beam can be related to the power of the laser P_{Av} using the repetition rate of the laser R_{Av} through equation 2.8 [19].

$$E = \frac{P_{av}}{R_{Rate}} \quad (2.8)$$

To compare the energy output within different laser treatments the use of an energy fluence (ϕ) is usually measured in J/cm^2 . This is described in equation 2.9 where E is the energy of the laser pulse and A is the cross sectional area of the laser beam defined by the Gaussian beam width [19]. This is usually a circular area and as a result the equation for the area of a circle is used ($A = \pi w_0^2$).

$$\phi = \frac{E}{A} \quad (2.9)$$

Continuous lasers create a continuous beam of energy until the voltage driving the ionisation of the laser tube is stopped. Common applications are the engraving or cutting of metal and surfaces. Instead of considering the pulse time of the laser the time under illumination at each spot the laser irradiates needs to be considered to find how much energy is delivered by the laser in this time frame. This is usually a function of the speed of the laser head raster and the size of the spot of the laser.

For continuous lasers, the energy delivered by the beam to the material is dependent on the dwell time of the laser over that spot. This depends upon the speed of the laser head and the size of the beam. This is described in equation 2.10.

E is the energy delivered in each spot of the laser track with exception to the first half diameter and last half diameter of the laser, some laser systems incorporate a 'punchout' at the start to account for this. The average power is P_{av} and the dwell time is t which is found from the speed-distance equation substituted into equation 2.10 where v is the speed of the laser head relative to the work-piece and d is the diameter of the laser beam.

$$E = P_{av} t = P_{av} \frac{d}{v} \quad (2.10)$$

Finding the energy applied to the work piece with the continuous laser means the fluence delivered to each spot can be found and compared to the pulsed system. Through using 2.9 the fluence can be derived using the circular symmetry of the beam. This leads to equation 2.11 for the fluence delivered to an area of the material with the beam radius w_0 [26]. This provides the ability to compare the energy applied to pulsed and continuous beam ablation.

$$\phi = \frac{2P_{av}}{\pi w_0 v} \quad (2.11)$$

2.5 Laser Ablation of Solids

Electromagnetic radiation initially interacts with the electrons inside the metal or alloy since the electric and magnetic fields of the photon only interact with charged matter and the atomic protons are neglected due to their binding in the nucleus [21]. The electrons in the material are excited by the electric field, through collisions with the other constituents of the metal energy is transferred to the lattice.

The lattice will heat up and as the temperature rises, the amount of absorbed light may change depending on the composition, this is due to the change in collision frequency of the electrons. After absorption of the laser energy, the material gains thermal energy and if enough energy is provided the material melts and then vaporises. If further energy is provided, the vapour can be ionised to form a plasma, the whole process with the formation of plasma visualised in figure 2.5.

The figure shows a heat affected zone which is the area where the temperature of material rises and subsequently the material's properties are affected. The melt depth, which is defined as the depth of material that is melted and reformed after cooling, can be seen closer to the beam and at a higher temperature than the heat affected zone when under illumination. Finally dependant on the energy of the beam a portion of the melted area is vaporised which is referred to as the ablated depth or ablation trench.

2.5.1 Absorption of Laser Radiation

At the first point of contact between the material and the laser, the incident radiation will be either reflected, absorbed, or transmitted through the material. The proportion of absorption (A) of the material is defined as $A = 1 - R$, with R being the reflection coefficient.

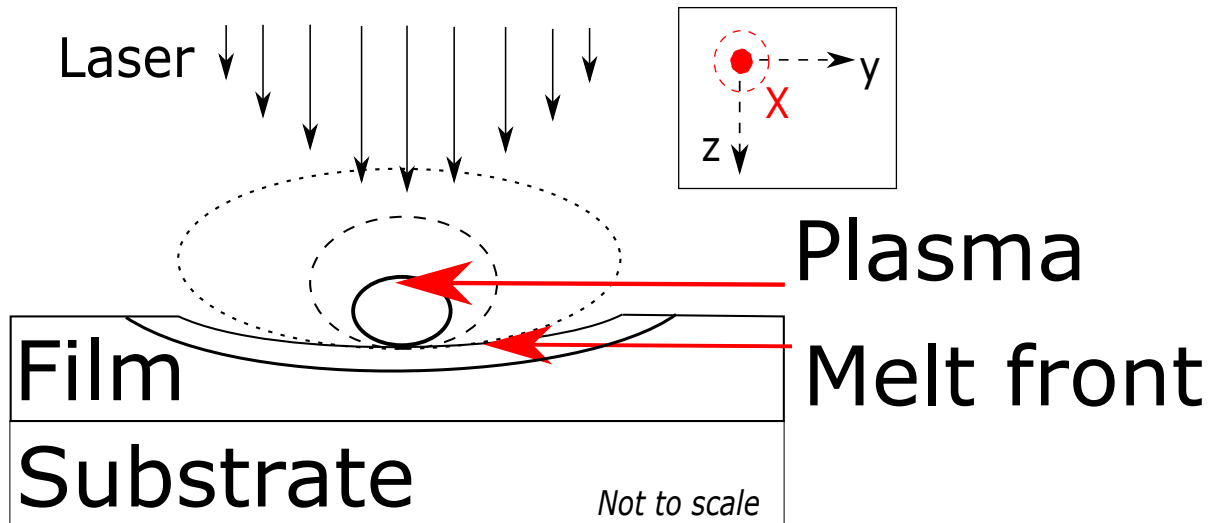


Figure 2.5: Diagram modelling the laser vaporisation process with plasma formation occurring at high laser intensities.

When radiation is not absorbed or reflected in the surface atoms it is transmitted through the material, this leads to heating in the deeper layers of the surface of the material as more of the material absorbs the laser's energy. The Beer-Lambert absorption model for laser beams interacting with media states that the intensity of a laser beam decays exponentially with depth z ([21],[23]).

The Beer-Lambert law is described in equation 2.12. The optical penetration depth is defined as the inverse of the absorption coefficient α , which is a function of radiation wavelength and material properties. This is defined from equation 2.12, where the definition is that when $z = l_\alpha$ the intensity I_z has been reduced to $1/e$ of the initial intensity I_0 .

$$I(z) = I_0 e^{-\alpha z} \quad (2.12)$$

The absorption of infrared radiation by metals largely depends on conductive absorption by free electrons [27]. Therefore the absorptivity can be calculated from data of the electrical resistivity of the film constituents. It has been demonstrated that the absorptivity of various polished metallic surfaces is a linear function of the square root of the electrical resistivity of the respective metals [27].

The proof of this and estimates for the absorptivity and reflectivity can be determined using the Drude model[27]. This is determined using the extinction coefficient, (κ) and refractive index (n) of the material through the equation 2.13.

$$\alpha = \frac{4\pi\kappa}{\lambda} R = \frac{(n-1)^2 + \kappa}{(n+1)^2 + \kappa^2} \quad (2.13)$$

The electrons in the material undergo rapid oscillations as the laser impacts the surface, these are known as plasma oscillations[28]. The relation of the plasma frequency, w_p is related to the product of the conductivity ρ and the mean time between electronic collisions τ_D and dielectric constant ϵ_o which is described in equation 2.14 [29].

$$\sigma = w_p^2 \tau_D \epsilon_o \quad (2.14)$$

The plasma frequency equals the angular frequency of light incident upon incidence, the range of electromagnetic waves considered has a angular frequency (ω) much greater than the scattering time thus the expressions in equations 2.13 and 2.14 can be approximated to the equation 2.15.

$$\alpha = \sqrt{\frac{2\omega\sigma}{c^2\epsilon_o}} \quad (2.15)$$

From the equation 2.14, the absorptivity is related to the laser wavelength and resistivity of the material. This is useful as if the film resistivity is well defined the absorption of the laser can be approximated. The total absorptivity is generally proportional to more factors than this such as the laser beam incidence angle, surface roughness and material temperature but this provides a rough enough measure for a qualitative description.

The absorption of photons by a material generally rises as its temperature rises to its melting point, thus the absorption at room temperature is the minimum absorption of radiation of the material. Once the melting point of the system is exceeded the reflectance of the system falls towards zero, with the depth of transmittance decreasing [30].

As the laser provides heating to the area, the heat dissipates outwards due to thermal diffusion through the material. The length of thermal penetration through laser energy is characterised as the thermal penetration l_{th} .

The thermal diffusion length characterises the distance over which temperature changes propagate in the time of laser irradiation. The thermal diffusion length is considered as a measure of how far the energy spreads from the region of the laser irradiation within the time of laser irradiation. This is defined in equation 2.16.

$$l_{th} = \sqrt{D\tau_{th}} : D = \kappa / \rho c_p \quad (2.16)$$

Where τ_{th} is the time for the pulse or time that the continuous beam illuminates a spot width length. The effective penetration of the beam can be characterised by equation 2.17.

$$l_{eff} = l_{th} + l_\alpha \quad (2.17)$$

The total radial sphere topped cylinder, centred at the centre of the beam with radius l_{eff} , is the area affected by the laser at the immediate illumination of the laser. When the laser stops illuminating a sample, the heat diffuses from that area. This region of thermal diffusion affected by the laser heating is defined as the heat affected zone (HAZ).

As a result of the rise in temperature in the affected area, the material exhibits a number of significant differences relative to the original material. The estimation of the size, temperature gradient and effects of the HAZ require formalisation of the differential heat equation and study of how the material will change when undergoing heat treatment [21]. This would require the numerical computation of this system to find quantitative results, which is made more difficult by the in-homogeneous surface structures and composition of the film.

The choice of laser wavelength illuminating a sample has a large impact on the optical and thermal penetration depth of the laser by a given material. The parameters of different lasers that alter the penetration depth are their wavelength, beam profile and interaction time.

In addition, the type of material the laser is incident upon greatly affects the optical and thermal penetration depth. For example, metals generally reflect the infrared irradiation of the CO₂ laser [24] whereas acrylic (PMMA) strongly absorbs light in the 10.6 μm region[31].

2.6 Laser Ablation of Films

There are a variety of ablation regimes mainly characterised by the interaction time, fluence, and angle of incidence of the beam considered [32]. Different regimes dominate depending on the combination of process factors contributed by the laser system and the material. As has been previously discussed within the material section the focus of the research is on the laser ablation of the film which has a in-homogeneous composition of Nickel, Iron, Chromium and Nickel Oxide.

Athermal ablation is the induction of bond dissociation provided through photon energy absorption [33]. The bond strengths in Nickel Oxide have been investigated through the photo-luminescence of NiO nanoparticles [34]. It was found in this literature the emission is detectable in UV region from light of 3.72 eV to 3.47 eV indicating the breakdown of Ni-O bonds.

Thus a UV laser emitting energy in this region would at least be required to undergo these changes. Metals have a high binding energy because of their metallic bonding. The greatest photon energy provided by a UV laser is 6.4 eV ($\lambda = 193$ nm) [19] which is smaller than the binding energy of the metallic bonds making the athermal ablation of the film unachievable. The wavelength of light of CO₂ lasers is of an energy 5x smaller than this, thus the photon energy of CO₂ lasers is too low to induce the athermal ablation regime.

Thermal ablation takes place when an area gains energy greater than the combined sum of energy to heat the volume to its melting temperature, the change of state to melt the area and the energy required to vaporise the volume. This balance of energy is displayed by equation 2.18 [25]. Where the energy required to ablate a region is E_v , m is the ablated mass, N the number of laser pulses, E_{pulse} the pulse energy, ΔH_m melting enthalpy, ΔH_v evaporation enthalpy, c_p the heat capacity, T_V evaporation temperature and T_0 ambient temperature.

$$E_v = m(c_p(T_V - T_0) + \Delta H_m + \Delta H_v) \quad (2.18)$$

This provides a value of the minimum amount of energy required to ablate a volume of material, in practice due to the reflection of the beam due to the surface and the diffusion of heat through the material the energy used can be much higher than this value.

2.6.1 Material Change After Laser Irradiation

Once the material has absorbed the energy from the laser, there are a variety of other effects that can take place within the material. The material has been shown to have a inhomogeneous composition of metals and metal oxides, this means there is a concentration gradients of oxidation within the material. As reviewed in the material properties section, the diffusion of ions in the material is limited by the fast quench rate in the flame spray process. The heating of the film means that the ion diffusion is no longer limited. The diffusion flux (J) is proportional to the diffusion coefficient (D) times the concentration ϕ gradient. this is described in equation 2.19 [35].

$$J = -D \frac{d\phi}{dx} \quad (2.19)$$

The diffusion of metal atoms is a thermally activated process [9] thus the diffusivity can be written in the form of equation 2.20 [35]:

$$D = D_0 e^{-E_d/k_b T} \quad (2.20)$$

where D_0 is the diffusion coefficient. E_d is the potential energy barrier height for the ion motion inside the material, k_b is the Boltzmann constant, and T is the temperature of the ion. Thus it follows from equation 2.19 and 2.20 that the greater the temperature of the material the greater the diffusion of ions within the material. A hypothesis to draw is the metal- metal oxide regions seen in the material section after laser treatment will become lower and more homogeneously oxidised as the oxidised material is the vast proportion of material. In addition the ability for Nickel Oxide to absorb Iron and Chromium ions into interstitial sites means the Iron and Chromium portions will also become associated with the Nickel Oxide matrix.

2.6.2 Surface Factors Affecting Laser Treatments

The main variables in laser surface modification is the power of the laser, beam spot size, beam quality, speed of laser scan, film condition (roughness, temperature and absorptivity), composition, and thermodynamic properties [23]. The understanding and control of these laser processing parameters for the flame sprayed material is important to achieve repeat-ability and an optimum micro-structural change of the film.

Roughness on a sample increases the absorption of the incident light due to the light reflecting from the surface and the reflected light being more likely to strike another part of the film's surface where it then gets absorbed. This increases the proportion of light absorbed by the material [36].

Additionally this means that there is an change to the energy distribution of absorbed light. Focusing effects can also take place on the material. When light is incident on a rough surface, the lights momentum must be conserved so the light is likely to be focused onto the bottom of the surface, due to impinging a small angle of incidence with the rough surface, increasing the energy density in that region.

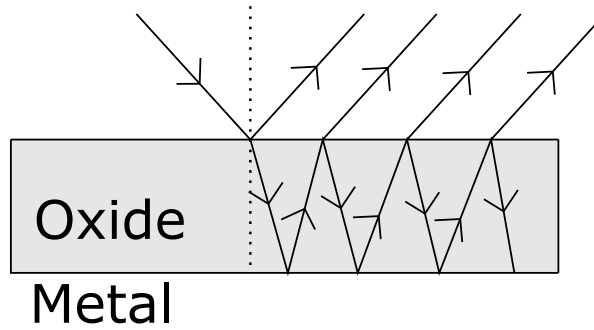


Figure 2.6: A diagram showing the internal reflection of light at interfaces of varying refractive indices

Dependant on the roughness of the sample it is possible that where the average depth of ablation is greater than the thickness of the film the film s ablated completely in this area. As a result the film can be damaged and in an electrical system lead to short circuits, this is why careful control of the laser parameters for the film roughness is determined.

The absorption of light in materials with differing refractive indices and absorption also leads to some changes to the dynamics of transmitted light within materials. The film has been shown through the optical, X-ray microscopy techniques by Duffield (2017), to have an in-homogeneous structure arranged in layers of materials differing in composition and crystal structure. Due to the in-homogeneous structure, discontinuities between the layers of the element can arise.

At these discontinuities, when light is incident on the material, a proportion of the light will be transmitted. The light transmitted through the material when encountering a discontinuity have a chance to reflect, this leads to the reduction of the absorption length of the light and thus a greater density of energy absorbed onto that area[37].

Within this work, the angle of irradiation is constant throughout the process at 90° and polarisation of the beam is left unpolarised / untested because of experimental limitations. The literature states that lasers impinging on a material at an angle greater or less than 90° have a lower absorbance than impinging perpendicular to the surface [19]. In addition since the beam interacts with the work-piece at an angle the cross section of interaction is changed making the assumption of circular symmetry of the beam and workpiece to be invalid.

The dependence of ablation rates and fluence required for ablation on the number of laser pulses is called incubation [38], this is the process where by the ablation of one area results in the reduction of the threshold fluency of the next pulse.

The origin of incubation is usually attributed to the generation of high-density defects in the material. The subsurface regions affected by void/crack formation are expected to exhibit significantly lower heat diffusion lengths, l_{th} , than the homogeneous bulk material due to strongly reduced heat diffusivity [38]. Thus, the heat dissipation is reduced and the ablation threshold decreases. It follows that due to the effect of the flame spraying technology that the material will already have voids, cracks, and discontinuity that will lead to a lower ablation threshold than that already calculated.

2.6.3 Laser Ablation of the Heating Element Film

So far the laser ablation of samples has been very generalised, with only specifics added to the sections for the material under observation. This section compares the use of infrared lasers (CO₂) in a pulsed regime for the use of laser ablation of the film.

To review, the film is made from a variety of components with Nickel, Chromium, Iron and Nickel Oxide, the main constituents as verified by the previous work into material science [2]. The primary phase is Nickel Oxide followed by the metallic Nickel, then in small quantities the Iron and Chromium. The metallic sections are held either in small bubbles of metallicity or are arranged in a milky pattern through the oxide matrix. There is the presence of voids within the material as well as a surface roughness of the order of a 10 μm variation in the height of features.

The percentage absorption of infrared lasers on Nickel Oxide samples between wavelengths of 1 and 10 μm was found to be as high as 80% indicating a high absorption of infrared light at the NiO interface can be absorbed[39].

Generally metals have a much higher reflection coefficient than oxides to infrared wavelengths of light [23]. Within the review of the film material properties it was found that, due to the high temperature of deposition in the flame spray process, the film has a layer of oxidation on its surface. This means this reflection coefficient value of 80% to infrared light is likely accurate for the whole film for the initial ablation of the film.

The absorption spectrum of NiO, Ni, Fe and Cr make the largest contribution to the absorption length in the material as these are the main constituents of the film. NiO films have been observed to have a continuous background absorption occur in the range from 0.1 to 3.5 eV of the order of $\alpha = 10^5 \text{ cm}^{-1}$ which increases with impurity concentration ([40]).

It was also found that the absorption coefficient rises steeply above 3.5 eV to be plateauing at a value of 10^6 cm^{-1} at 4 eV [40]. The NiO within the material has been found to have a high presence of impurities [2], thus the value of the absorption coefficient could be larger than 10^5 cm^{-1} to CO₂ radiation.

Other work done has found the absorption spectrum for NiO at a range of laser wavelengths, this is shown in appendix item A1. At 1.5 eV the absorption coefficient is 54000 cm^{-1} thus the effective penetration depth, the depth at which the beam power is reduced to $\frac{1}{e}$, is 0.185 micrometers. This agrees with the value obtained through other literature, so seems a reasonable value for this parameter.

The thermal penetration depth varies with the pulse or interaction time. Within the range of laser pulse or interaction time available, the interaction must be 0.01 μsec or longer to have a thermal interaction size greater than the optical penetration depth, at this point half of the beam's energy will be dissipated outside of the optical penetration depth.

Other material properties that are important for the heating of matter are its thermal diffusion and heat capacity. The heat capacity of NiO and semiconductors increases as they are heated due to the increase in conduction electrons. When metals melt their heat capacity increases but the difference between their melting point and vaporisation temperature is small [29].

The Thermal conductivity of NiO is around 30 W/m K but for thin films (around 200 micrometers) can be half as much. Additionally at interfaces between different materials and grains there is a lower thermal diffusion [41], this means that since the material is so inhomogeneous the HAZ will be less than that predicted in clean samples.

2.6.4 Experimental Literature on the Material After Heat Treatments

To gain data for how the material could change after laser ablation a comparison can be made to Duffield's work on the heat treatment of Nickel Oxide flame sprayed films. Duffield (2017) heated the film at 800°C for 66 hours. He found that XRD showed the spinel 311 peak relative to the NiO 111 and 200 peaks increased notably during the process.

He found that the decomposition of the doped NiO was initiated at 600°C. He hypothesised that the spinel structure growth is due to the Cr and Fe metallic integration into the spinel structure while the Ni remains mainly in the oxide matrix. This provides some indication of the effect that a thermal laser treatment will have on the element surface and can be tested through other XRD and EDS experiments.

This indicates that in the heat affected zone of the laser interaction with the material it is possible for changes to the oxidation and crystalline structure to take place. Since the heating time is much smaller and the quench rate higher in laser treatments this should not effect a large proportion of the film but would be localised to the immediate areas of laser irradiation.

2.6.5 Justification of the Choice of Laser for Further Experimentation

This project, as most projects are, had a limitation on the amount that could be spent upon all the components in the project. Through comparing the cost of lasers per amount of output optical power the CO₂ laser showed the greatest amount of optical power per expenditure [19]. This allowed for the purchase of high amounts of optical power with comparable to other wavelengths of laser a low expenditure.

CO₂ lasers are currently available for purchase with combined gentry, control software and safety features pre-installed. This has the added benefit of improving the reliability of the laser system as its design was already validated and tested prior to the inclusion in the project.

In addition, the relevant mirrors and lenses for the CO₂ laser are available at a cost point within the budget of this project. The operation of a carbon dioxide laser is arguably the safest high energy laser due to the low laser frequency and respective low photon energy and the accessible range of absorbing materials for the construction of safety enclosures.

Through the flame spray deposition there exists a high surface roughness, oxidation, variance in constituents and general inhomogeneity. This means that the detailed and specific micro machining of these structures is not possible and the use of a laser as specific and powerful a UV laser would not offer the advantages it has over a CO₂ system because the film is too inhomogenous.

The CO₂ laser wavelnngth has been shown in the literature to be absorbed by the majority of the constituent parts of the film and has been shown to offer significant value for money. The combination of these factors and advantages at the cost of the higher absorption and focus ability of lower wavelengths meant that the carbon dioxide laser was the chosen as the most appropriate laser to be used to develop the system.

2.7 Model of Targeted Conduction Pathway Reduction of Conductors for Uniform Surface Joule Heating of Conductors

Since the material is made from multiple components there is a difference in the current density within the components. It is hypothesised that the metallic regions contribute the primary conduction medium. Thus the lines of conduction spread through the material like tree roots in the ground. If the volume of these current paths are reduced the cross section of the current flow will decrease and the current density will increase if the current flowing stays the same. If there is a larger current density the heat production will increase per voltage applied as shown through equation 2.3.

Since the voltage is applied across the whole element and the electrical resistance has increased within that area the heat production within that area will increase and the heat production within other areas will decrease as the proportionally higher resistance area gains a larger proportion of the energy.

2.7.1 Laser Ablation for the Increase in Uniformity of Heat Output of the Element.

There are three key effects to take into account, the increase of the localised resistance due to the thickness reduction, the increase in temperature due to the lower of volume of matter heated in the localised area, and the increase in resistance from the oxidation or melting of the film. The resistance change due to the thickness reduction of localised areas is taken into account in the above analysis but the resistance change due to the change in oxidation is not taken into account.

The oxidised nickel has a resistivity 10 times that of metallic nickel. This means for every area that is ablated the same area that is oxidised contributes 10x as much to the resistivity change. For this reason the analysis and observation of the device oxidation change is undertaken to understand these changes.

In addition the change in thickness of the conductor means there is less material for the element to heat and thus reaches a higher temperature this is given from the heat equation given in 2.21. This states that the amount of heat a mass of material m takes to heat a difference in temperature ΔT is proportional to the product of the mass, temperature change and specific heat capacity (c_p).

$$Q = mc_p\Delta T \quad (2.21)$$

The greater the amount of mass that is required to be heated the more energy is needed, thus if the ablation process is removing material the amount of energy required to heat the ablated region to the same temperature is decreased leading to a higher temperature.

Since there is also oxidation of the material from the laser process the specific heat capacity of the material changes, the specific heat capacity of the oxidised Nickel is double the metallic specific heat capacity thus it takes double the amount of energy to heat the surface to the same temperature if the whole surface becomes oxidised.

Chapter 3

Methods

3.1 Optical Microscopy

An optical microscope is used to investigate the film at magnifications up to 1000x, the microscopic system used is a Leica DM2700 M operated under bright-field illumination. The optical system contains polarising filters to reduce the reflections of the coating and obtain clear images, which is a reflected light microscope.

It illuminates the specimen from the same side as the objective lens since the film is opaque the light reflects from the surface of the film. The light is focused by the objective lens, after illuminating the sample the reflected light re-enters the objective lens creating an inverted, real image of the sample within the microscope. This image is then magnified by the eyepiece producing an enlarged, virtual image for the camera to record.

Samples are mounted within Bakelite through a pressurised mounting procedure, and were then prepared by grinding the samples as in standard metallographic procedure. Silicon carbide grinding papers are used up to a 2500P grade where the sample is polished with 5 μm and 1 μm diamond paste, this achieves a 1 μm finish.

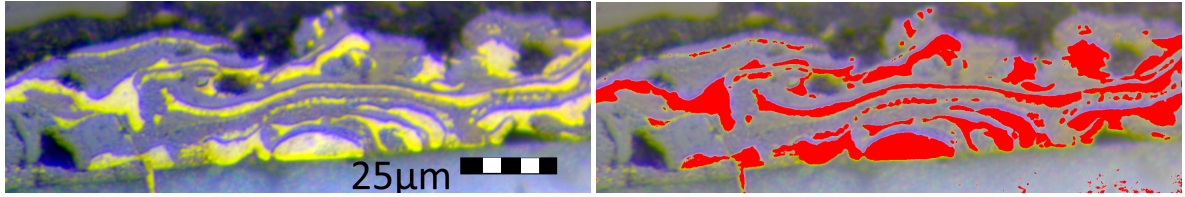


Figure 3.1: Example of the optical micrograph of a section of film with the metallic regions highlighted. Film thickness of $39\ \mu\text{m}$ for the image scale.

Measurements of the percentage of metallic, oxides, and voids within the thick film were captured by the camera within the microscope that is coaxial with the optical system. Using the image processing software ImageJ, the percentage of the various regions of the film were found by segmentation of the image dependent on their intensity. There was high contrast between the three different components, this enabled the regions to be easily separated within their optical micrograph, with good accuracy. This process is shown in figure (3.1)

3.2 X-ray Techniques

The use of X-ray diffraction (XRD) and X-ray Photo-electron Spectroscopy allowed the research to look at the changes in structures and weight percentage in the powder after flame spray and the changes in the element after ablation. This was important as it allows for the more detailed comparisons of the processes taking place within the laser ablation methodology.

3.2.1 X-ray Diffraction

The XRD used in this work was a Rigaku SmartLab Powder XRD. This is a 9 kW Cu-source generator and equipped with a high-resolution Vertical θ/θ 4-Circle Goniometer and D/tex-ULTRA 250 High-Speed Position Sensitive Detector System operated in reflection mode.

XRD relies upon Bragg diffraction of X-Rays by crystal lattices. In Bragg diffraction, the path difference between X-rays scattered by different atomic planes must be an integer number (n) of wavelengths (λ) for coherent diffraction, as shown in figure 3.3. This can be written in terms of inter-planar spacing (d) and angle (θ) for the condition of constructive interference [42]:

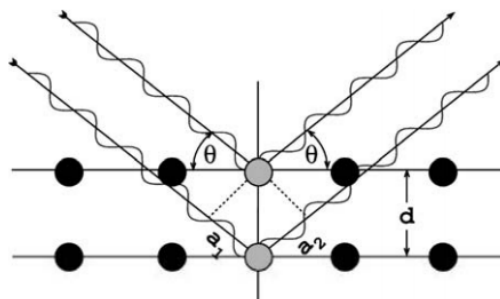


Figure 3.2: Visualisation of the constructive interference of X-rays by an atomic lattice [42].

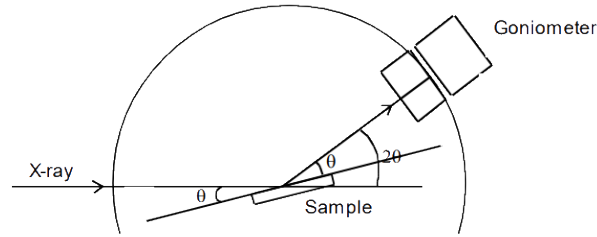


Figure 3.3: Diagram of a XRD diffraction experiment.

$$2d \sin \theta = n\lambda \quad (3.1)$$

The X-ray source is fixed during the measurement and the scanning pattern is implemented by rotating the detector over a selected range of angle 2θ (relative to the source) whilst simultaneously rotating the sample by angle θ to maintain the symmetric geometry (shown in the figure 3.2). At certain angles, constructive interference occurs when the Bragg condition is satisfied and a high X-ray intensity is detected. Each peak in intensity is related to a particular inter-planar spacing for a set of hkl planes which shows the crystal structure of the sample.

During experimentation the goniometer rotates, varying the interaction angle between specimen and X-ray beam to obtain a range of angles and therefore data. This is recorded by the CCD detector in the instrumentation after various filters and optical enhancement of the signal has taken place.

Data was collected over a 2θ range of 30-50°, with a step size of 0.01° and dwell time of 5 seconds . These settings were selected so a reasonable signal to noise ratio was obtained.

Upon completion of the scans, peak search software was used to remove background noise and the Cu K α peak. Phase identification was then conducted by comparing results with standard XRD data obtained from the inorganic crystal structure database (ICSD). Finally, this data was analysed with graphing software and peaks matched, this is displayed within the results section under the XRD heading.

The peak positions were used to find the lattice parameters and crystal structure in the sample, and peak intensity data was used to give indication of the phase fractions and the corresponding change in the phase fractions after ablation. [42]

3.2.2 Energy Dispersive X-Ray Fluorescence

The model used for Energy Dispersive X-Ray Fluorescence (EDXRF) was a Shimadzu EDX 8000. In EDXRF spectrometers, all the elements in the sample are excited by a direct excitation. In this process, the atoms in a specimen are excited by primary photons from external sources, such as an X-ray tube. A detector with a multi-channel analyser is used to collect the fluorescence radiation emitted from the sample and separate the different energies of characteristic radiation from the different sample elements. [43].

The expression between the count rate of the characteristic X-ray and the content of an element of the tested sample is shown by equation 3.2:

$$I_K = \frac{K1}{\mu_0 + \mu_k} \times W_k \quad (3.2)$$

Where I_k and I_0 are the K^{th} characteristic of the X-ray of measured element and count rate of incident X-rays. Moreover, μ_0 and μ_k are absorption coefficient of the tested substance to the incident X-ray and the emission of K^{th} characteristic X-rays. The magnitude of K is a constant for the calibration of measurement device. W_K is the measure of the content element. Through the manipulation of the weighting of these factors and by using primary filters to test for elements from individual samples, the device can distinguish across a range of light (C) to heavy (U) elements.

3.3 Scanning Electron Microscopy

The scanning electron microscope (SEM) used in this work was a JEOL JSM-7800F, which uses a focused, high energy electron beam to examine the surface of the specimen. When incident electrons interact with the sample surface they generate secondary and back-scattered electrons in the material, which is shown in figure 3.4.

This data is recorded by a detector and as the beam moves across the surface raster, an image of the material's topography was generated. Additionally, this data can be used to give an indication of chemical composition and crystal structures as the electron interaction with the material depends upon its density and composition ([44]).

An image of a SEM is shown in Figure 3.5. Typically a SEM is composed of an electron gun encased in an electron column and a working chamber containing the optics to focus the electron beam, held under a vacuum to avoid the electrons becoming scattered by particles before interacting with the sample. After emission from the electron gun, the electrons are accelerated down the electron column by an applied potential difference.

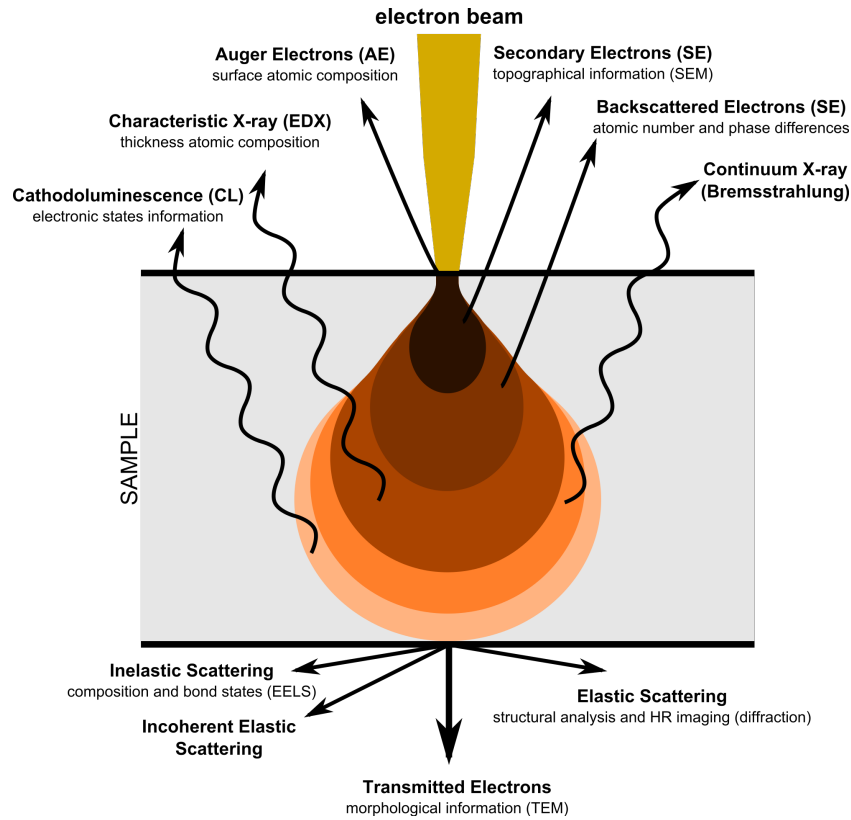


Figure 3.4: A diagram of an electron beam interacting with a material and a visualisation of the resulting effects. Adapted from [45].

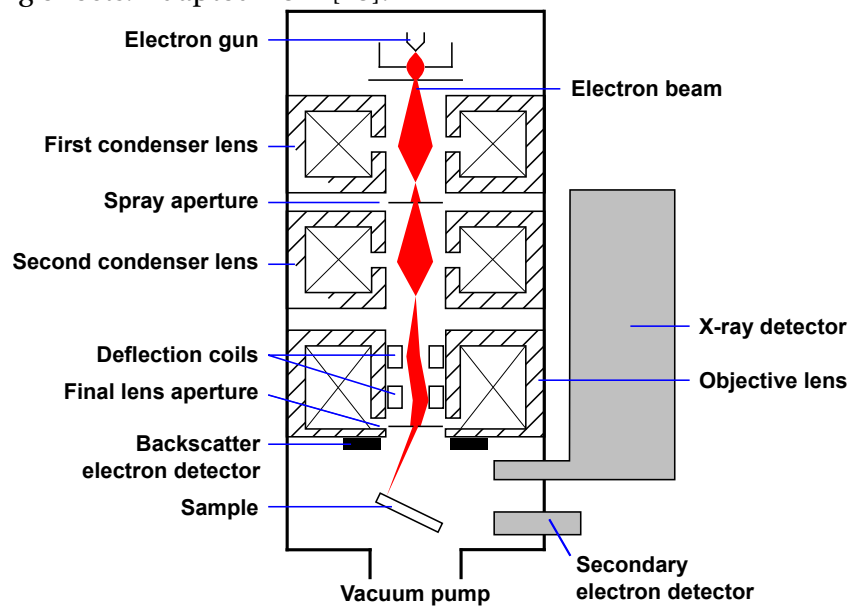


Figure 3.5: A diagram of a Scanning Electron Microscope in operation to image a sample [46].

The electrons accelerate within the potential difference due to their charge, the potential difference polarity is pulsed sinusously so that the electrons travel in a straight line down the column. Within the column, electromagnetic lenses focus the beam in a similar way, apertures in the beam line control beam current and diameter whilst stigmators produce a circular beam profile. To map an area, deflector plates are used to raster the beam. Detectors inside the chamber then measure the intensity of secondary and back-scattered electrons emitted after the electron collided with the sample surface [44].

The main advantage of a SEM over optical methods is the use of radiation with a smaller wavelength than visible light. As a result a SEM can resolve finer details than traditional light microscopes. SEMs can resolve features of less than a nanometer, this resolution is far larger than the required resolution to distinguish features on the micrometer scale required in the applications within this thesis.

In contrast to optical microscopy the SEM has a greater depth of field, this is due to the smaller convergence angle of the electron beam. This is advantageous within this application as there is a high degree of surface roughness in the primary material which increases after laser irradiation.

3.4 Scanning Electron Microscopy with Energy Dispersive Spectroscopy

The interactions between the electrons in an SEM and matter generates radiation, these emitted X-Rays can be used in the characterisation of materials due to the unique atomic structures within the material emitting x-rays of a characteristic wavelength. The characteristic X-rays emitted are specific to an element's atomic structure thus allowing elements to be identified uniquely from each other.

This is due to the principle that after stimulation by radiation an atoms electrons rise from their ground state to higher energy levels in discrete energy levels. In addition, electron holes can be generated by the ionisation of an atom via the ejection of electrons from energy levels.

Subsequently, the electrons from outer, high-energy levels are more likely to move to lower energy levels to fill the hole, resulting in the difference of energy between the energy levels of the de-excited electron being emitted as a X-ray. The energy and amount of X-rays emitted are then measured by a detector, usually silicon-drift detectors. The energy of each X-ray is characteristic of the element it is emitted from. The difference in energy of the energy levels the electron was de-excited from can then be used to identify the element from which it was emitted.

Incident X-rays impact the detector, they create electron-hole pairs, as a voltage is applied across the detector semiconductor, a current proportional to the energy of the X-ray is produced. By measuring the size of the current relative to the probe current, the energy of the incident X ray can be determined and thus the element it was produced from can be identified. Within this experiment a probe current of 10 mA is used to take these measurements to maximise the amount of counts detected.

Within the experiment 20kV of electron energy was used, this is higher than the critical ionisation energy of Nickel, thus ensuring that the Nickel will be found within the spectra. The dead time was approximately 30-40% and live times of 60s or greater were used to generate a high quality elemental image and spectra.

Experimental errors and problems can be introduced when trying to gain the spectra of low atomic number elements this is due to the windows used to shield detectors from contamination absorbing a significant amount of the low energy X-rays emitted by low mass elements making them difficult to detect. Due to the ultra-thin windows used in the SEM-EDS used in this research, the analytic range can be extended to make measurements of elements as light as Boron.

3.5 Optical Scanning Profilometry

To gain accurate measurements of the depth of ablation and the surface roughness of the element samples, a scanning profilometer was used. The brand of equipment used was a MarSurf CP/ CL select nano focus uScan system, the specifications of this system are a maximum measurement field of 16x15cm, and vertical resolution limit 1 μm .

The advantage of an optical system over a physical probe is a higher rate of scanning and a wider depth of field and range which means that an in-homogeneous and rough sample like the element can be scanned quickly and accurately.

An optical profilometer works by moving along a raster over the worktop, with a laser taking height data of the distance from worktop to laser head. As the laser scans the beam oscillates backwards and forwards so that the laser scans in the x direction and y direction as the head is moving. The oscillation is built into the analysis software so that the values in the x direction are recorded. The laser head is able to determine the height of the surface through interferometry of the laser beam.

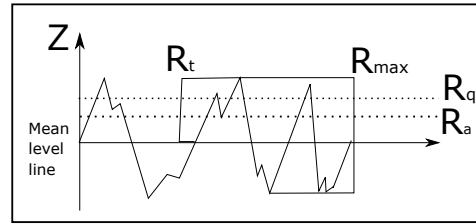


Figure 3.6: Surface roughness parameters indicated on a profile plot of an arbitrary rough sample.

Within the laser head and the laser detector is a interferometer. This is used to gain accurate data on the height measured by the laser at each point. This is done through measuring the time it takes for the laser to reflect from the surface of the work piece and become detected. since the speed of the laser is finite (the speed of light), the distance the laser travels can be calculated. The recorded data is then transmitted into a file for the height data for each measured point.

The required resolution must be stipulated by the user prior to the device working, the smaller the resolution in the x and y direction the longer the task will take to complete. The results are analysed by a metrology software which is used to visualise and analyse the profilometric images data. In addition, the surface roughness can be calculated from the software. Surface roughness is defined in multiple ways to measure the various qualities of the roughness. A diagram showing the surface roughness measurements is given in figure 3.6.

Ra is the arithmetic average of the absolute values of the profile heights. Rt is the vertical distance between the highest and lowest points of the profile. Rq is the root mean square average of the profile heights, and Rmax is the greatest difference between the peak and depth of ablation. These values can be used to describe the surface roughness of the sample.

3.6 Microscopy Sample Preparation

To prepare the samples for the microscopy techniques used, a variety of processes was needed so that the microscopy techniques used were applicable. Initially samples had to be cut to the correct size to width within the SEM and XRD, this was achieved with a diamond saw. For samples imaged under optical microscopy, some were able to be imaged without sample preparation. The cross section optical images were produced by cutting the sample to a thin strip, which was then hot mounted on its side with a bakelight mounting solution within a hot mounting machine where the sample was heated with the bakelight solution to 120°C and a constant pressure was applied to set the sample.

The sample was then ground and polished with an automated grinding machine. This was done through the use of silicon carbide abrasive papers, starting from a p600 decreasing down to P2400. In between switching of the grinding papers the samples are washed to remove particulates from their surface so that in subsequent grinding the particulates from the previous grinding do not rub against the sample.

After grinding the sample is polished with 3 µm and 1 µm diamond paste respectively. The aim was to achieve as good a finish as possible as the focal depth of the optical microscope was low and better results are achieved with a flat surface for EDX. This process was also undertaken for the samples that are mounted face on with their face ground.

The ground samples were produced because for accurate EDX measurements a flat surface produced more accurate results, this is crucial as the samples have an inherent variation in the elemental composition. Therefore, no elements can be discarded from the elemental analysis as there would be no evidence from the known elemental analysis to suggest a systematic error due to the surface roughness.

3.7 Resistance Measurement through the Four-Probe Method

The measurement of the resistance and sheet resistance of the film was done through a four-probe line resistance method. This method was chosen because it reduces the effect of contact resistance on the measurement of the resistance, allows for the graphing of the resistance across the elements after they have been ablated and the resistance can be measured more precisely than with more traditional two-probe resistance measurement techniques.

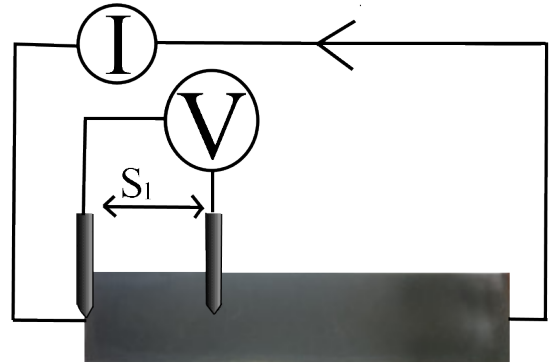


Figure 3.7: Diagram of the methodology of the resistance measurements of the element.

$$R = \frac{V}{I} \quad (3.3)$$

This method is shown within the diagram in figure (3.7). It displays how the voltage and the voltage sensing electrical lines are kept separate except in the place of connection with the film. The voltage probe is scanned at 1 cm intervals across the length of the element making connection with the film and recording the voltage between the present position on the film and the fixed contact at the start of the sampling area. Keeping one probe in a fixed position reduces the uncertainty in the lateral position and means the contact resistance of the element is constant across all tests as the fixed probe has the same contact across the film.

When the data is analysed the voltage between the n th section is calculated by finding the difference between the voltage across the n th and the value at n th-1 measurement. This is then used with Ohms law from equation 3.3 and the current recorded by an ammeter in series with the power source. The estimation of errors in the resistance measurement is characterised by adding the errors in quadrature for the error in the voltage measured from position to position and the errors in the current measurement from the ammeter.

3.8 Statistical Techniques

A variety of statistical techniques are used within the project so that the effects of the laser processing can be analysed. The surface temperature profile data can be described by statistical techniques, the two main techniques are the standard deviation of the temperatures on the element and the kurtosis of the element surface profile. The statistical processing was done with a MATLAB ® code written with the default MATLAB ® functions with some alterations so that the all the data was analysed.

The standard deviation of the thermal image data gives an indication of how much the spread of data is converging at each processing cycle, the standard deviation of a 2D space is given by equation (3.4) ([47]). The mean (\bar{X}) is defined so that the standard deviation ($\hat{\sigma}$) can be calculated. N_i measurements of the temperature profile are taken across the element to compute the standard deviation. The use of the standard deviation in the research is to quantify the spread of the data around the mean. This can be used to compare the spread of temperature output by the elements after ablation. Therefore this is a measure of the average uniformity of the surface temperature.

$$\bar{X} = \frac{1}{N_1} \sum_{i=1}^N X_i \quad \text{and} \quad \hat{\sigma}^2 = \frac{1}{N-1} \sum_{i=1}^{N_1} (X_i - \bar{X})^2 \quad (3.4)$$

The standard deviation determines the average deviation of the data from the mean but does not describe how it is distributed. kurtosis is the measure used within this research as a way to quantify the distribution of the data. The definition of kurtosis is the ratio of the fourth moment (m_{4th}^4) and the variance squared [48]. This gives the following equation (3.5).

$$K = \frac{m_{4th}^4}{(\sigma^4)} \quad (3.5)$$

This can be generalised in equation 3.6:

$$K = E\left(\frac{X - \mu}{\sigma}\right)^4 \quad (3.6)$$

K is the kurtosis value, E describes the expectation operator, X the variable, μ the mean, and σ the standard deviation. This shows that the values within $\mu \pm \sigma$ will not contribute much to the kurtosis, but values far from the mean, usually described as outliers, have a large effect on the kurtosis, hence it is a good measure for the shape of the data. The kurtosis is used to measure the temperature profile shape profile. An example of different distributions and their kurtosis is shown in Figure 3.8.

The kurtosis of the normal distribution is 3, distributions that are more outlier-prone, i.e. have more data that deviates from the mean and variance on the outskirts of the data than the normal distribution have a kurtosis greater than 3; distributions that are less outlier-prone have a kurtosis less than 3. Since these values are scaled to the standard deviation and mean of the data the comparisons of the kurtosis of elements with different means and standard deviations can take place. This leads to some counter intuitive results.

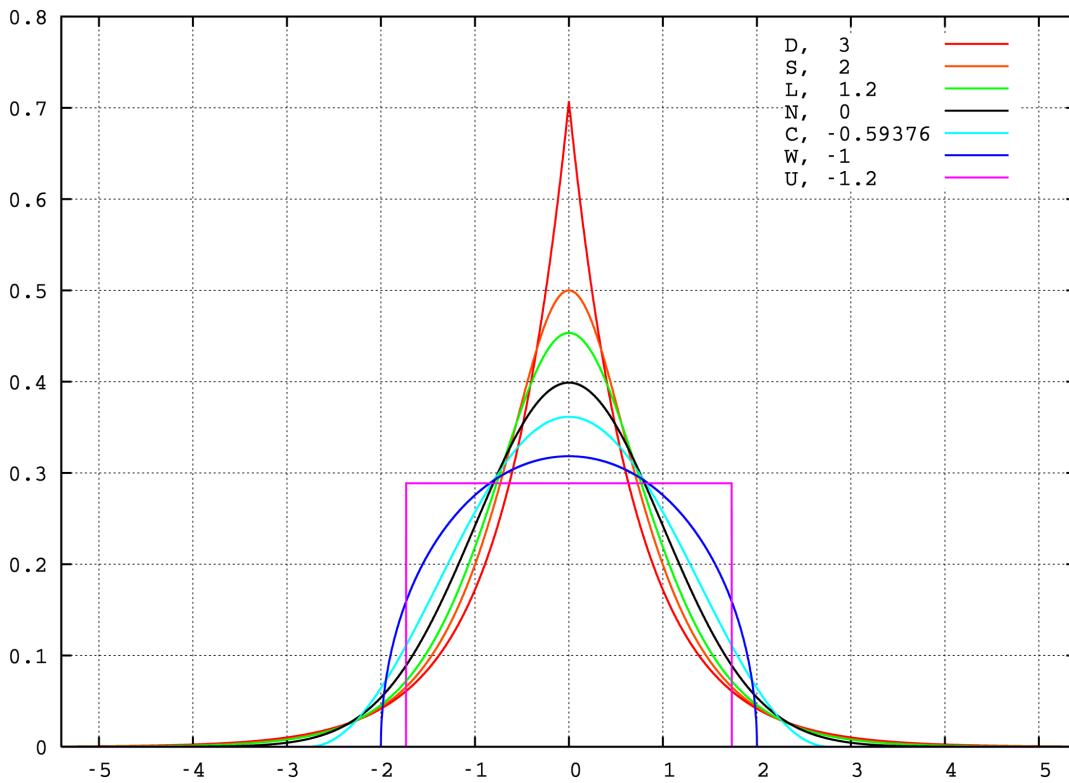


Figure 3.8: The plots of various distributions with mean 0, variance 1, and against the excess kurtosis where 0 excess kurtosis indicates absolute an kurtosis of 3). The normal distribution is labelled with an excess kurtosis of 0 and an absolute kurtosis of 3 as is the definition of the kurtosis [49].

Since the kurtosis indicates the shape of the temperature profile of the data. When the kurtosis of the temperature profile is less than 3, the profile is determined to have a hot spot located in the centre of the element. This seems counter-intuitive as a higher kurtosis value indicates a more peaked distribution. Understanding can be gained if the element temperature profile is considered as a temperature distribution, when there is a hot spot the outliers of the temperature distribution are, on average, closer to the mean temperature and lower in temperature thus resulting in a lower kurtosis as the kurtosis scales by the size of the outlier too. In addition this can be experimentally verified as the distributions with a greater surface temperature uniformity as judged by eye have a kurtosis value closer to 3.

With a kurtosis >3 , the element has a greater amount of the hot spot spread across the element. The closer the kurtosis is to the value of 3, the more uniform the temperature distribution. A value of kurtosis of 3 indicates the distribution matches the normal distribution.

This indicates that the spread of the data with a value of kurtosis of 3 has a lower amount of underlying structure causing that distribution and is closer to a random distribution [48]. This matches the theory of thermal diffusion which indicates that the distribution of temperatures will follow a normal distribution as well.

Chapter 4

Experimental System Design Experiments

To design the system, a range of parameters and experiments were required to examine the material response to laser ablation and to provide data so that an informed choice of system could be made. Tests of the material response to CO₂ laser ablation were carried out on a 80W laser system summarised as the PIRANHA system. The laser is a carbon dioxide laser with a 10.6 μm wavelength, power range of 0-80W and speed 0-600mm/s. The system has access to both continuous and pulsed regimes.

In addition the microscopic morphology changes from the laser ablation were investigated along with the phase changes as the laser ablation takes place. The laser radius at the focal point of this laser was measured through optical microscopy to be 0.2mm with an error of ± 0.05 mm from the uncertainty in the focus height of the laser, which is important to take into consideration.

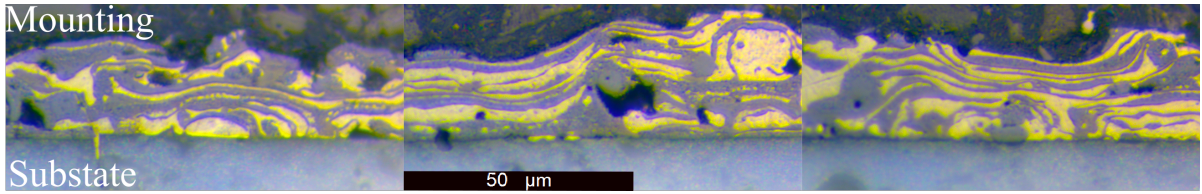


Figure 4.1: An optical image of the cross section of the film after mounting and polishing. The film thickness was found to be $39 \pm 8 \mu\text{m}$.

4.1 Properties of the intrinsic film

There are a variety of properties of the intrinsic film that were investigated, this section summarises the relevant results from those investigations. A polished cross section of the film is displayed in figure 4.1. The results of the image analysis of the film cross sections suggested the film was 17% alloyed metal, 62% oxide, and 21% porous with a film.

However, the porosity value is likely to be inflated due to difficulties distinguishing pores from voids created during sample preparation. Evidence of voids being added through the sample preparation are found by comparing cross sectional images in figure 4.1. Here voids are shown in the film and in the substrate that the film is mounted on both before and after ablation showing that some of the voids could be due to the sample preparation.

Figures could be further skewed if these voids form through the preferential displacement of either the metallic or oxidised material. The film thickness was found to be $39 \pm 8 \mu\text{m}$, this was found from recording the width of the film across the substrate at 0.1 mm intervals across the cross sections of a set of elements.

Table 4.1: Scanning probe measurements of the average surface roughness of the unablated element.

Quantity	Arithmetic Average Ra	Min-Max Range Rt	Root Mean ² Rq	Maximum Height Rmax
Value (μm)	2.7	23.1	3.4	15.5

4.2 Surface Roughness of the Element

To investigate the variation of surface roughness of the elements, the surface height variation of 10 elements has been recorded with a scanning profilometer. The profilometer scans across the surface and records the difference in height of the features on the element to itself. The process is explained in the methods section as is the calculation of the surface roughness. The surface roughness measurements are recorded in table 4.1.

The measurements indicate that there is a significant variation of the element's profile height. The average arithmetic variation is Ra, this shows that most of the average height change of the surface is within 2.7 (μm). Rt is the vertical distance between the highest and lowest points of the profile. It shows that there is a variation of film height of 23.1 (μm), which means that the focus depth of the laser needs to be at least larger than this value.

Rq is the root mean square average of the profile heights, showing that the majority of the differences between the height of the film is within 3.4 (μm). This value is generally high, but if within the focus depth of the laser the treatment delivered from the laser should affect all regions equally. Rmax is the greatest difference between the peak and depth of ablation. In addition to the Rt value this indicates that there can be a wide variation of surface height.

More importantly, the volume of material and the depth of the film varies in a inhomogeneous way which means that there will be a variation in the ablation delivered to the film if the laser focus depth is too small because the thickness of the film has a large effect on the efficiency of the laser ablation process.

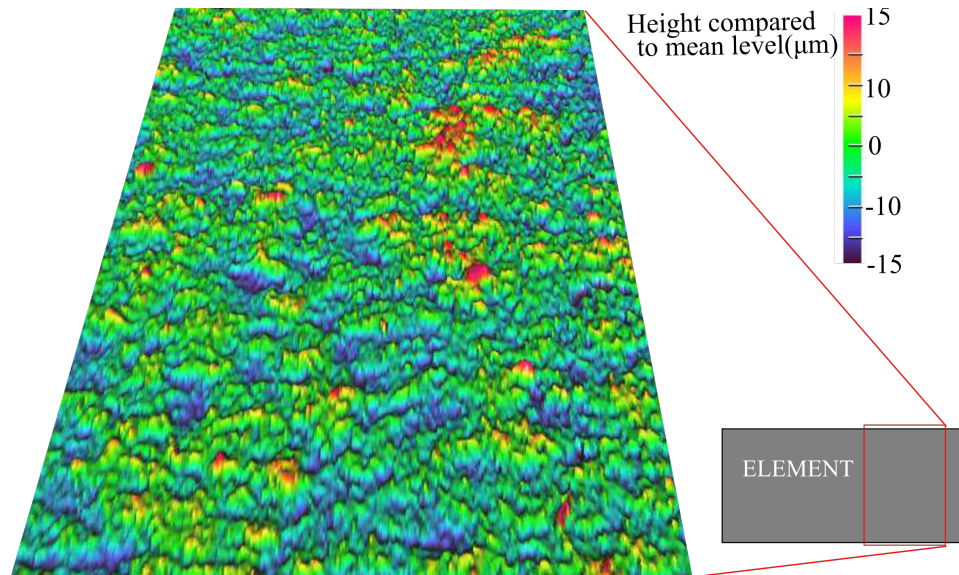


Figure 4.2: A 3D re-projection of the profilometer data of the surface heights across an 10x20mm section of the element compared against a mean level, heights not to scale with the width and length of the element.

When reviewing this experiment, it was observed that there is a wide range of heights of the film thickness and surface heights. Therefore, if a laser with a focus depth less than the feature height interacts with the area, there will be a difference in the treatment delivered. Therefore, the system must focus the laser to a point that has a depth of field larger than this feature size. In addition, due to the roughness of the surface, there can be lensing effects and reflection of light on the film thickness.

This can lead to an in-homogeneous heating of the surface from the laser. For this reason, a small spot larger than these features must be used whilst also balancing the need for a small spot size to enable melt depth and lower powers of the laser. A spot size between 0.1-0.2mm has been specified for the laser to meet these requirements. The depth of focus of the laser must also take the range in surface height into account also so the minimum focus depth is ± 0.5 mm.

To visualise the surface roughness a 3D re-projection of the surface is shown in figure 4.2. This shows how the distribution of the surface roughness changes and that the surface roughness is in-homogeneous. This means that there can be slight variation in the surface height in different regions. This is also mirrored in the profilometer statistics where the maximum ranges of the surface roughness is very high compared to the film thickness but the mean roughness is fairly low.

4.3 Preliminary Ablation Tests

To investigate the effect of continuous wave carbon dioxide lasers on the target material with the range of powers (10-80W) and speeds (5-600mm/s) at a wavelength of 10.6 μ m an industrial laser cutting machine which matches these parameters was used, as referred to by the PIRANHA system. The specified range of power and speed was required to establish a power-speed-matrix of the laser effect on the material under these conditions.

Squares, i.e. groups of lasered lines with a set distance between the lines, were lasered within a matrix onto the element surface at various powers and speeds. These were analysed with an optical microscope to observe laser effects on the material structure. A matrix of various laser powers and speeds is shown in figure (4.3).

The matrix illustrates that under laser ablation within the range of power and speeds selected, there is a range of different morphology created by the laser on the film surface. The complete power-speed matrix is given in figure 4.4. The groups of categories is given in figure 4.2 this classifies the damage done to the surface from a 1 to 5 point scale.

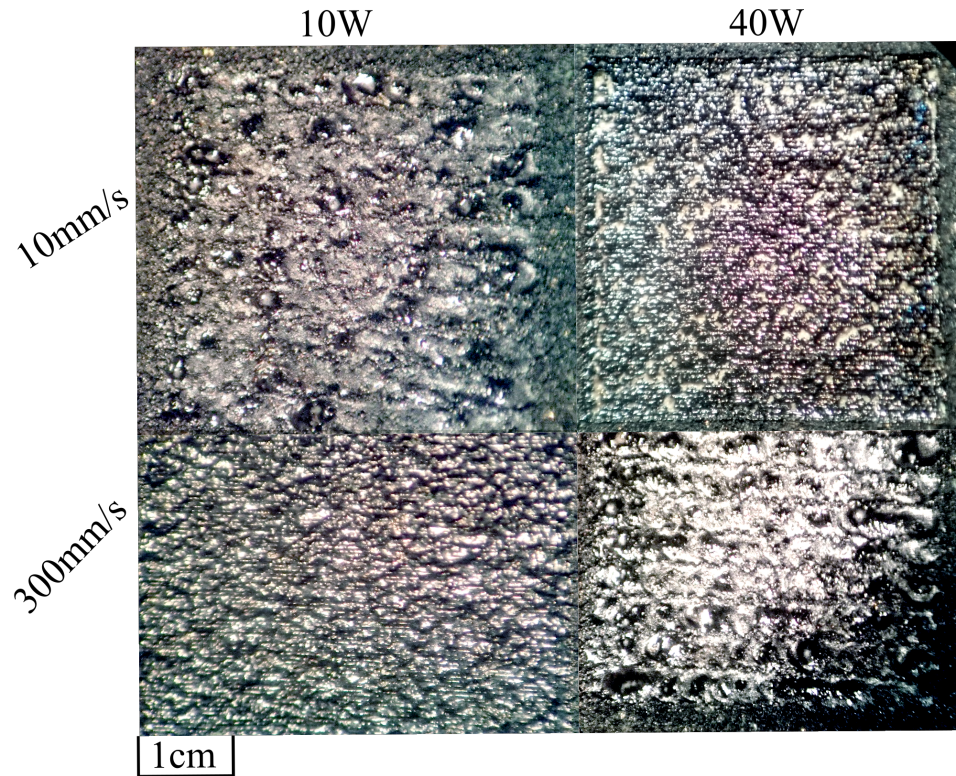


Figure 4.3: A matrix of continuous wave carbon dioxide laser irradiation of the flame sprayed element at various speeds and powers of laser using the PIRANHA system.

Table 4.2: Characterisation of damage to the film surface from the continuous wave laser ablation matrix

Damage category	Description	Effects observed
1	No visible change to the ablated area or light colourisation changes	Oxidation
2	Colour changes to the surface with visible surface depressions	Oxidation, melting and some ablation
3	Darkening of area with visible kerfs along the line of ablation with surface depressions	Oxidation, melting and ablation
4	Visible ablation depth with darkened melt depth	Oxidation, melting and ablation
5	Whole film is ablated to the substrate layer with large cut kerfs	Oxidation, melting and ablation

At a low power and high speed the fluence of the laser is low as the laser is applied to each position for a small amount of time. This results in the surface being mainly melted as shown in figure (4.3). There is some evidence of ablation when looking at the dross formation along the edges of the laser tracks.

Additionally, due to the high speed the heat affected zone is smaller than at lower speeds as the laser irradiates the area over a shorter time frame. When the power increases and the speed was kept high more extreme morphology was observed, larger melt depths and a greater amount of dross was seen, indicating more ablation than at a lower power and a greater effect on the film.

At low speeds and low powers there is a clear melt depth seen across the film with some undulation of the film surface indicating a high in-homogeneity of underlying structure. Where the power is increased and the speed is kept low the highest fluence is incident on the film surface. This leads to the greatest amount of visible ablation from the film where even the substrate under the film becomes visible. The area has been melted through with a high amount of contrast between the surface and the ablated region.

Data of the whole laser effect matrix has been collated into figure 4.4. This shows the variation of effect on the surface of the element at the various powers as is summarised above. Since the fluence applied to each spot size differs depending on the speed and power of the laser the fluence of each laser track is tabulated in figure 4.5. The transitions between damages categories has been indicated on the table.

Speed of laser (mm/s)	Power of Laser (W)														
	10	15	20	25	30	35	40	45	50	55	60	65	70	75	80
300	1	1	1	1	1	1	1	1	1	2	2	2	3	3	3
250	1	1	1	1	1	1	1	1	2	2	2	2	3	3	3
200	1	1	1	1	1	1	1	2	2	2	2	2	3	3	3
190	1	1	1	1	1	1	2	2	2	2	2	2	3	3	3
180	1	1	1	1	1	1	2	2	2	2	2	2	3	3	3
170	1	1	1	1	1	1	2	2	2	2	2	2	3	3	3
160	1	1	1	1	1	1	2	2	2	2	2	2	3	3	3
150	1	1	1	1	1	1	2	2	2	2	3	3	3	3	3
140	1	1	1	1	1	1	2	2	2	2	3	3	3	3	3
130	1	1	1	1	1	1	2	2	2	2	3	3	3	3	3
120	1	1	1	1	1	1	2	2	2	3	3	3	4	4	4
110	1	1	1	1	1	1	2	2	2	3	3	3	4	4	4
105	1	1	1	1	1	2	2	2	3	3	3	4	4	4	4
100	1	1	1	1	1	2	2	2	3	3	3	4	4	4	4
95	1	1	1	1	1	2	3	3	3	3	4	4	4	4	4
90	1	1	1	1	1	2	3	3	3	3	4	4	4	4	4
85	1	1	1	1	1	2	3	3	3	3	4	4	4	4	4
80	1	1	1	1	1	2	3	3	3	3	4	4	4	4	4
75	1	1	1	1	1	2	3	3	3	3	4	4	4	4	4
70	1	1	1	1	1	2	3	3	3	3	4	4	4	4	4
65	1	1	1	1	1	2	3	3	3	3	4	4	4	4	4
60	1	1	1	1	1	2	3	3	3	3	4	4	4	4	5
55	1	1	1	1	1	2	3	3	3	3	4	4	4	4	5
50	1	1	1	1	1	2	3	3	3	3	4	4	5	5	5
45	1	1	1	1	1	2	3	3	3	3	4	4	5	5	5
40	1	1	1	1	1	2	3	3	3	3	4	4	5	5	5
35	1	1	1	1	1	2	3	3	3	3	4	4	5	5	5
30	1	1	1	1	2	2	3	3	3	3	4	4	5	5	5
25	1	1	1	1	2	3	3	3	3	3	4	4	5	5	5
20	1	1	1	1	2	3	3	3	3	3	4	4	5	5	5
15	1	1	1	2	2	3	3	3	4	4	4	4	5	5	5
10	1	1	1	2	2	3	3	3	4	4	4	4	5	5	5
5	1	1	2	3	3	3	4	4	4	4	4	4	5	5	5
1	1	2	2	3	3	4	4	4	4	4	4	4	5	5	5

Figure 4.4: Tabulation of the effect of the continuous wave laser on the material at various powers and speeds.

Speed of laser (mm/s)	Power of Laser (W)														
	10	15	20	25	30	35	40	45	50	55	60	65	70	75	80
300	0.17	0.25	0.33	0.42	0.50	0.58	0.67	0.75	0.83	0.92	1.00	1.08	1.17	1.25	1.33
250	0.20	0.30	0.40	0.50	0.60	0.70	0.80	0.90	1.00	1.10	1.20	1.30	1.40	1.50	1.60
200	0.25	0.38	0.50	0.63	0.75	0.88	1.00	1.13	1.25	1.38	1.50	1.63	1.75	1.88	2.00
190	0.26	0.39	0.53	0.66	0.79	0.92	1.05	1.18	1.32	1.45	1.58	1.71	1.84	1.97	2.11
180	0.28	0.42	0.56	0.69	0.83	0.97	1.11	1.25	1.39	1.53	1.67	1.81	1.94	2.08	2.22
170	0.29	0.44	0.59	0.74	0.88	1.03	1.18	1.32	1.47	1.62	1.76	1.91	2.06	2.21	2.35
160	0.31	0.47	0.63	0.78	0.94	1.09	1.25	1.41	1.56	1.72	1.88	2.03	2.19	2.34	2.50
150	0.33	0.50	0.67	0.83	1.00	1.17	1.33	1.50	1.67	1.83	2.00	2.17	2.33	2.50	2.67
140	0.36	0.54	0.71	0.89	1.07	1.25	1.43	1.61	1.79	1.96	2.14	2.32	2.50	2.68	2.86
130	0.38	0.58	0.77	0.96	1.15	1.35	1.54	1.73	1.92	2.12	2.31	2.50	2.69	2.88	3.08
120	0.42	0.63	0.83	1.04	1.25	1.46	1.67	1.88	2.08	2.29	2.50	2.71	2.92	3.13	3.33
110	0.45	0.68	0.91	1.14	1.36	1.59	1.82	2.05	2.27	2.50	2.73	2.95	3.18	3.41	3.64
105	0.48	0.71	0.95	1.19	1.43	1.67	1.90	2.14	2.38	2.62	2.86	3.10	3.33	3.57	3.81
100	0.50	0.75	1.00	1.25	1.50	1.75	2.00	2.25	2.50	2.75	3.00	3.25	3.50	3.75	4.00
95	0.53	0.79	1.05	1.32	1.58	1.84	2.11	2.37	2.63	2.89	3.16	3.42	3.68	3.95	4.21
90	0.56	0.83	1.11	1.39	1.67	1.94	2.22	2.50	2.78	3.06	3.33	3.61	3.89	4.17	4.44
85	0.59	0.88	1.18	1.47	1.76	2.06	2.35	2.65	2.94	3.24	3.53	3.82	4.12	4.41	4.71
80	0.63	0.94	1.25	1.56	1.88	2.19	2.50	2.81	3.13	3.44	3.75	4.06	4.38	4.69	5.00
75	0.67	1.00	1.33	1.67	2.00	2.33	2.67	3.00	3.33	3.67	4.00	4.33	4.67	5.00	5.33
70	0.71	1.07	1.43	1.79	2.14	2.50	2.86	3.21	3.57	3.93	4.29	4.64	5.00	5.36	5.71
65	0.77	1.15	1.54	1.92	2.31	2.69	3.08	3.46	3.85	4.23	4.62	5.00	5.38	5.77	6.15
60	0.83	1.25	1.67	2.08	2.50	2.92	3.33	3.75	4.17	4.58	5.00	5.42	5.83	6.25	6.67
55	0.91	1.36	1.82	2.27	2.73	3.18	3.64	4.09	4.55	5.00	5.45	5.91	6.36	6.82	7.27
50	1.00	1.50	2.00	2.50	3.00	3.50	4.00	4.50	5.00	5.50	6.00	6.50	7.00	7.50	8.00
45	1.1	1.7	2.2	2.8	3.3	3.9	4.4	5.0	5.6	6.1	6.7	7.2	7.8	8.3	8.9
40	1.3	1.9	2.5	3.1	3.8	4.4	5.0	5.6	6.3	6.9	7.5	8.1	8.8	9.4	10.0
35	1.4	2.1	2.9	3.6	4.3	5.0	5.7	6.4	7.1	7.9	8.6	9.3	10.0	10.7	11.4
30	1.7	2.5	3.3	4.2	5.0	5.8	6.7	7.5	8.3	9.2	10.0	10.8	11.7	12.5	13.3
25	2.0	3.0	4.0	5.0	6.0	7.0	8.0	9.0	10.0	11.0	12.0	13.0	14.0	15.0	16.0
20	2.5	3.8	5.0	6.3	7.5	8.8	10.0	11.3	12.5	13.8	15.0	16.3	17.5	18.8	20.0
15	3.3	5.0	6.7	8.3	10.0	11.7	13.3	15.0	16.7	18.3	20.0	21.7	23.3	25.0	26.7
10	5.0	7.5	10.0	12.5	15.0	17.5	20.0	22.5	25.0	27.5	30.0	32.5	35.0	37.5	40.0
5	10.0	15.0	20.0	25.0	30.0	35.0	40.0	45.0	50.0	55.0	60.0	65.0	70.0	75.0	80.0
1	50	75	100	125	150	175	200	225	250	275	300	325	350	375	400

Figure 4.5: Tabulation of the calculation of the fluence (J/mm^2) applied to each spot size (0.2mm) within each experiment. The green coloured cells indicate the transition between damage cases from the colouration of the surface to light ablation of the surface, the yellow cells indicate the transition between light ablation and heavy ablation and the orange cells indicate the transition between heavy ablation and ablation all the way to the substrate.

Analysing the matrix of speeds and powers and comparing it to the theory of laser ablation in the literature review section indicates that the greater the speed of the laser the lower the heat affected zone and higher lasing efficiency. As a result, the melt depth induced by the laser appears to be reduced at higher speeds. For this reason the highest speeds for the laser ablation of the films are specified, giving a minimum specification for the speed of the laser head relative to the work-piece of 100mm/s.

The range of fluence where the laser effect is desirable is between 0.75-1.17 J/mm². This means the laser system will have to be able to provide laser powers within this range. Through analysing the laser market in relation to the project budget it was decided that the highest power of carbon dioxide laser that could be afforded was a 40W laser.

As discussed in the literature review of laser technology, carbon dioxide lasers should not be ran at 100% of their maximal output as this leads to disassociation of the lasing gasses, thus the maximal output of the laser tube within the experimental system would need to be 2-3 times larger than the maximum output used in the tests. This means that the maximum output of optical energy that would be accessible with a 40W laser tube would be between 10-20W. Within these tests the power of the laser required is 40-70W to deliver the required fluence with a 0.2 mm spot size and 100-300 mm/s speed.

Since it has been shown that as high a speed as possible leads to the best film condition and the speed cannot be lowered to increase the fluence, as a result the spot size of the laser must be reduced for a 40W system. The fluence of the laser is proportional to the inverse square of the radius to increase the fluence of the laser by four times (from 0.17-0.25 to 0.75- 1.17 J/mm²) the radius of the laser must be halved. This would lead to a beam radius of 0.1mm.

4.4 Morphology Changes from the Interaction of the Laser and Film

The images of the element ablated after being polished compared to the film cross-section is shown in figure 4.8. This shows how the metallicity of the film has been reduced after the laser ablation. In addition the films structure is altered, the presence of voids is much lower in the ablated sample indicating the melting of the film as the ablation takes place. This laser ablation was done at a high power and low speed as defined in the figures and corresponds to the four squares in figure 4.3. A matrix of the power and speeds of laser is shown in figure 4.6. This shows four different combinations of power and speed applied to the element with the top of the element ground and polished.

Within the laser tracks with a greater amount of ablation (higher power and lower speed) the more the milky areas turn into dark oxidised areas with the metallic globules. This is seen also in the EDX measurements of the film. This indicates that the ablation has a large effect on the oxidation and composition of the melted regions with a large heat affected area. This means that the processing method chosen for the ablation treatment needs to effect the film as little as possible.

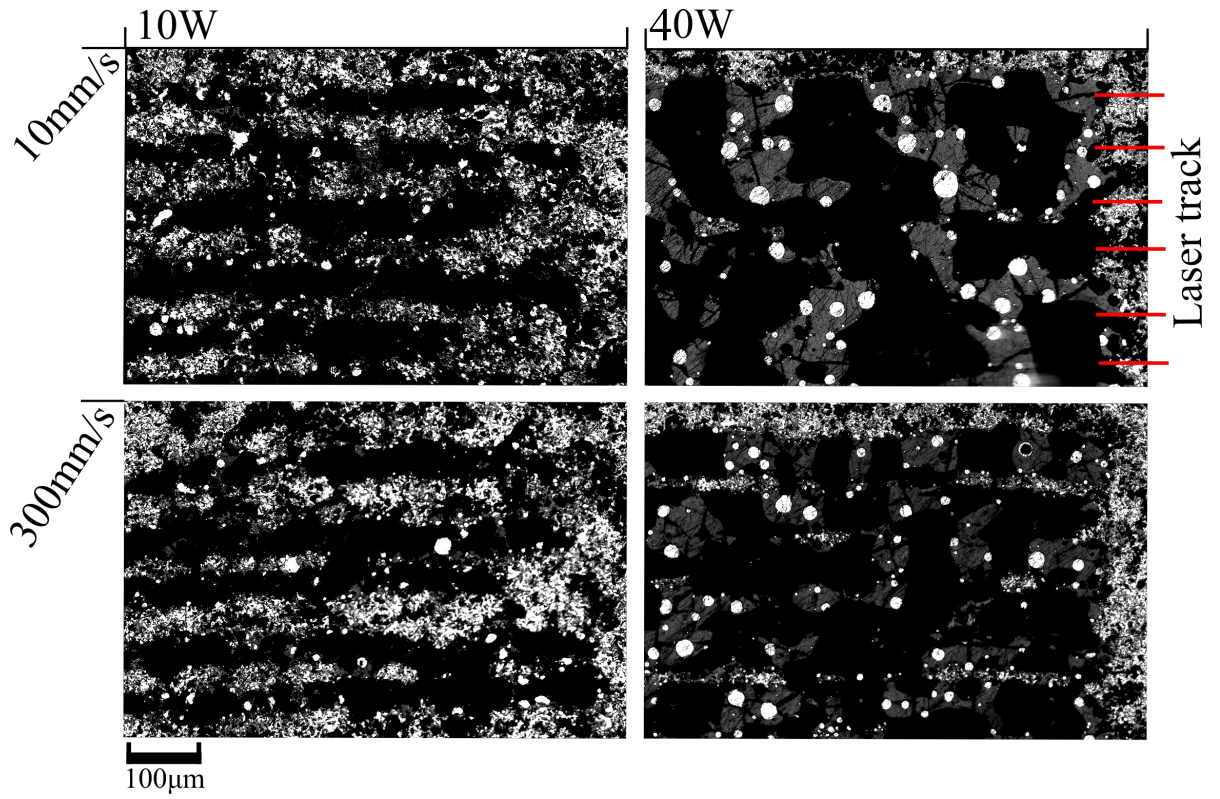


Figure 4.6: An optical image of squares of ablation after mounting and polishing the upper surface. The fluence of each is shown in figure 4.5.

Before

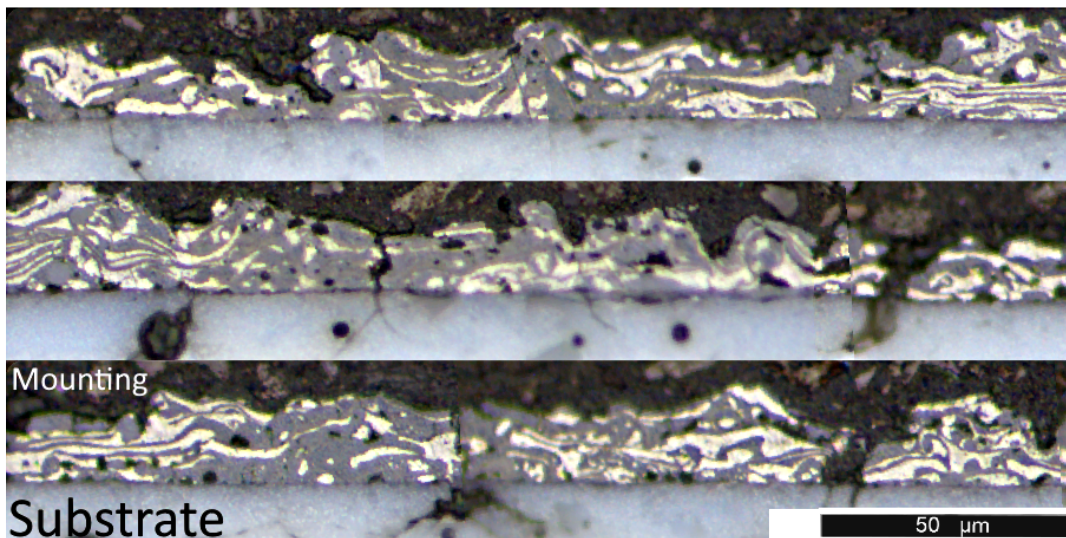


Figure 4.7: Optical images of the cross section of the film before ablation at the same magnification as 4.8.

After

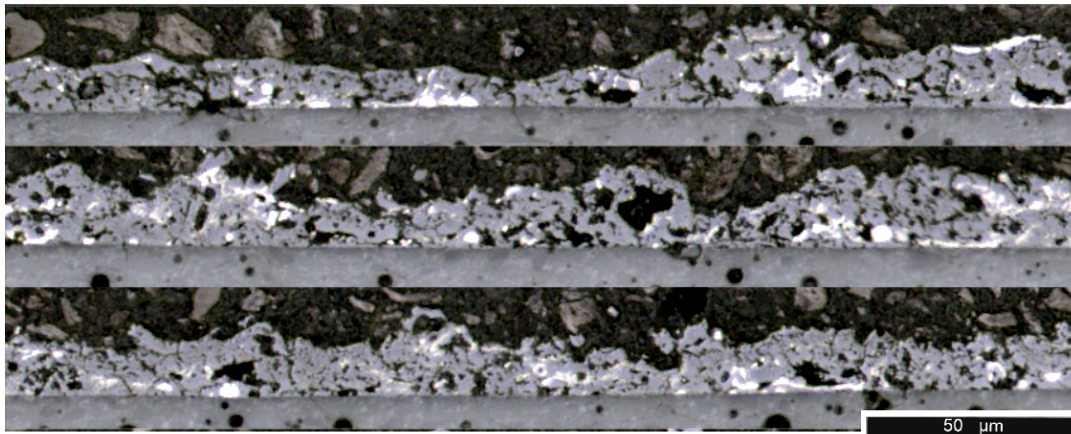


Figure 4.8: Optical images of the cross section of the film after ablation. The ablated sections cut across the lines of ablation with the beam having a slight overlap in each line of ablation.

4.5 X-ray Diffraction of Samples

To investigate the phases present within the flame sprayed element in the prepared powder, before ablation and after ablation x-ray techniques have been employed as discussed within the methods section.

Table 4.3 shows the proportion of peaks matched and thus the relative quantity of various phases throughout the samples. There are four samples examined, the prepared powder used in the flame spray process, the flame sprayed element, the Laser ablated film, and a heavily laser ablated flake that has been melted with the laser and ablated then removed from the substrate to investigate the wider effect of the laser treatment.

Table 4.3: XRD results summary of the proportion of various compounds on various materials investigated.

Compound	Prepared powder Percentage of Phase	Flame sprayed element	Laser ablated film	Laser ablated flake
Metallic Ni	60	54.3	35	5.7
Alloy (Fe-Cr)	12	9.1	12	8
Oxides	3.2	19.0	24.7	68.5
Other traces	bal	bal	bal	bal

Within the initial prepared powder is a high proportion of metallic nickel and alloy, there is still some oxide present which is produced in the oxidation step to prepare the powder. These values match with the proportions of phases seen with Duffield's work [2]. The element produced by the flame spray has a lower proportion of metallic nickel and alloy but a larger amount of oxides, this is to be expected from the flame spray process and again matches Duffield's work who recorded an oxide proportion of $\approx 20\%$.

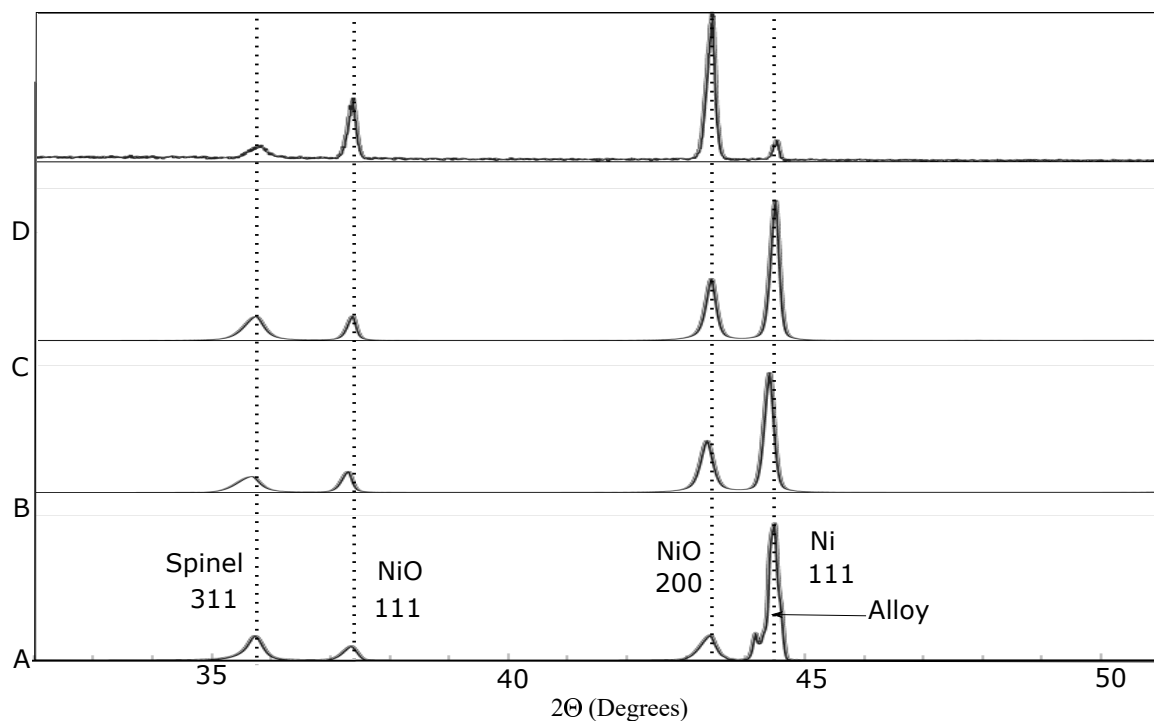


Figure 4.9: XRD results shown with the miller indices indicated for various shown species. A: Prepared Pre-flame sprayed powder, B: Flame sprayed element, C: Laser ablated element, D: Heavily laser ablated flake.

The laser ablated element oxidation increases again but less than the amount gained through the flame spray oxidation process. As a proportion, the amount of alloy increases and the proportion of Nickel decreases. The hypothesis drawn from this observation is that less alloy will be ablated in comparison to the nickel areas due to the lower melting point of Nickel. This follows for the oxide which also has a higher melting point than the nickel. In addition, the proportion of Nickel is expected to decrease if the proportion of oxide increases as the Nickel is oxidised.

The matched peaks of the XRD can be seen in figure 4.9. This shows the four main components, the oxide with Miller indices [200] and [111], metallic and alloy peaks with a Miller indices of [111] and the spinel peak with [311]. These results match the results seen in Duffields thesis and match the positions of the peaks found by Duffield.

Notable changes depicted in the plot are the decrease in metallic peak and the increase of the oxide peak within the ablated and heavily ablated proportions. This gives evidence that the laser ablation treatment also increases oxidation of the film. This has consequences for the research as the electrical conductivity of the oxide regions is lower than the conductivity of the metallic regions. As a result the calibration and selection of the parameters for ablation have to take into account the reduction in thickness of the conductor and the change in conductivity of material due to laser ablation.

4.6 SEM & EDX Microscopy

To further investigate the change in the film from laser ablation the film has been examined with a SEM with EDS mapping. The objective is to view the laser tracks at high resolution and gain EDS mapping of the laser tracks and surfaces to compare the effects of the laser interaction.

Figure 4.10 shows the unablated element with four different elemental maps from the EDX mapping applied to the SEM image. This suggest that there is an even distribution of the elements throughout the sample, some black spots appear on the surface where no EDX measurements were taken. These are created from the surface roughness obscuring the electron beam.

The composition of these is assumed to be similar to the other areas since the other areas show an even balance of elements with some grouping of elements in certain regions. This provides a good baseline to compare to ablated tracks on the element.

To further analyse the distribution of elements in the raw element, a film sample has been polished to remove the upper oxidised layer and reduce the surface roughness. Figure 4.11 illustrates this sample, it shows two regions, a dark region and a lighter region.

Due to the electron interaction with the material the darker region is a denser region and the lighter region is a less dense region. When compared to the EDX images the lighter regions coincide with the metallic elements (Ni, Fe, Cr). The dark regions have a higher amount of oxygen recorded, this shows that these regions are likely oxide regions. In addition, it is worthwhile to note that the pattern of the elemental distribution forms a milky pattern where the metallic portions are well mixed throughout the sample. There are some regions that form clumps of metallic regions.

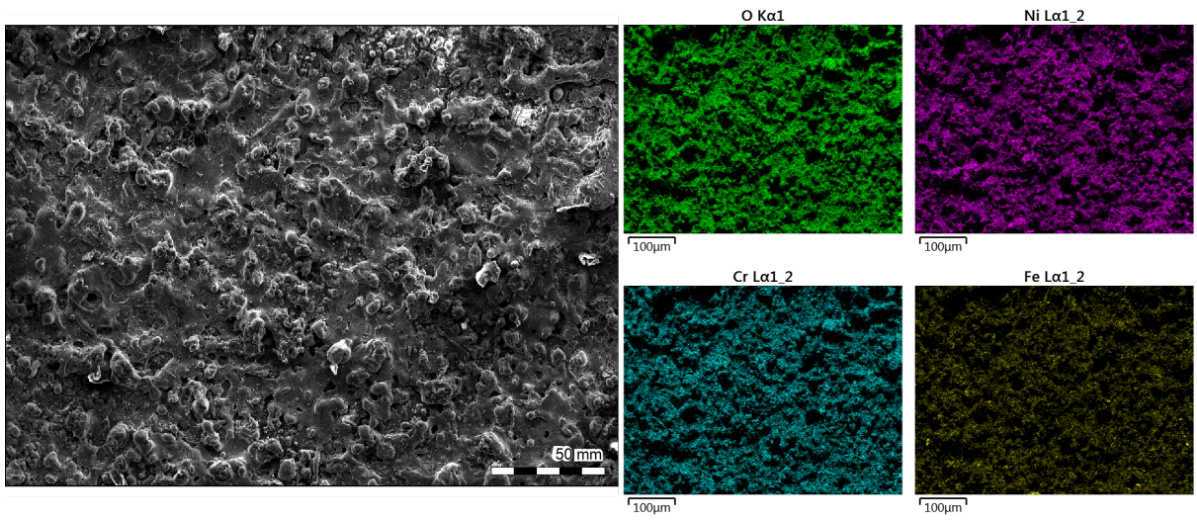


Figure 4.10: A SEM image of the raw surface roughness and four EDX elemental maps of the distribution of Ni O Cr and Fe on the rough sample.

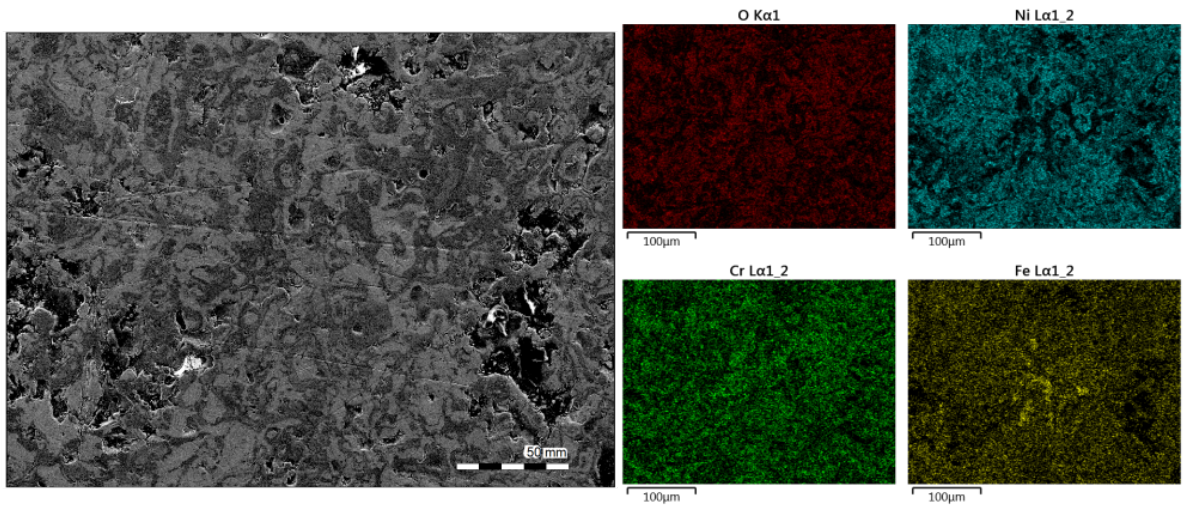


Figure 4.11: A SEM image and four EDX elemental maps of the distribution of Ni,O,Cr and Fe of a polished sample of a raw element.

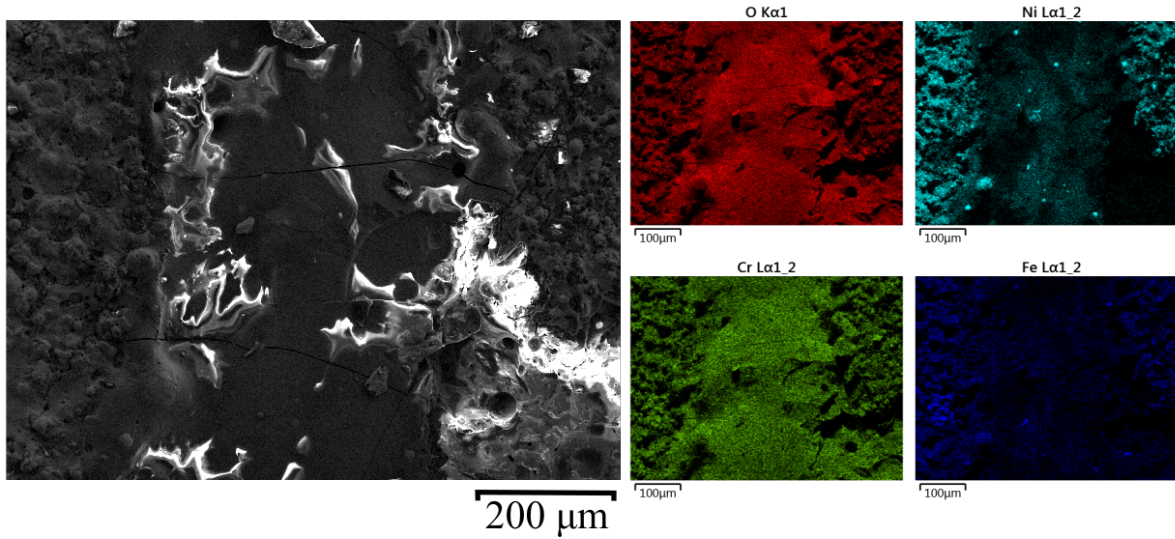


Figure 4.12: A SEM image and four EDX elemental maps of the distribution of Ni,O,Cr and Fe of a continuous laser ablated line at 25W at 300mm/s with a 0.2 mm spot size.

An SEM image of a laser line on this raw element is shown in figure 4.12. This shows a laser track with the rough surface of the element either side. At the edge of the laser track there is dross formation from the accumulation of material either side of the laser line.

What is also clear is there is a smoother surface compared to the rough surface of the element within the laser track, this is evidence of melting of the material where the laser has interacted with the area. The EDX maps show that the amount of Nickel in the laser line has reduced and the amount of oxide in the line has increased. The chromium seems to not be effected as much and the iron seems to be ablated in a higher proportion than Cr and less than Ni.

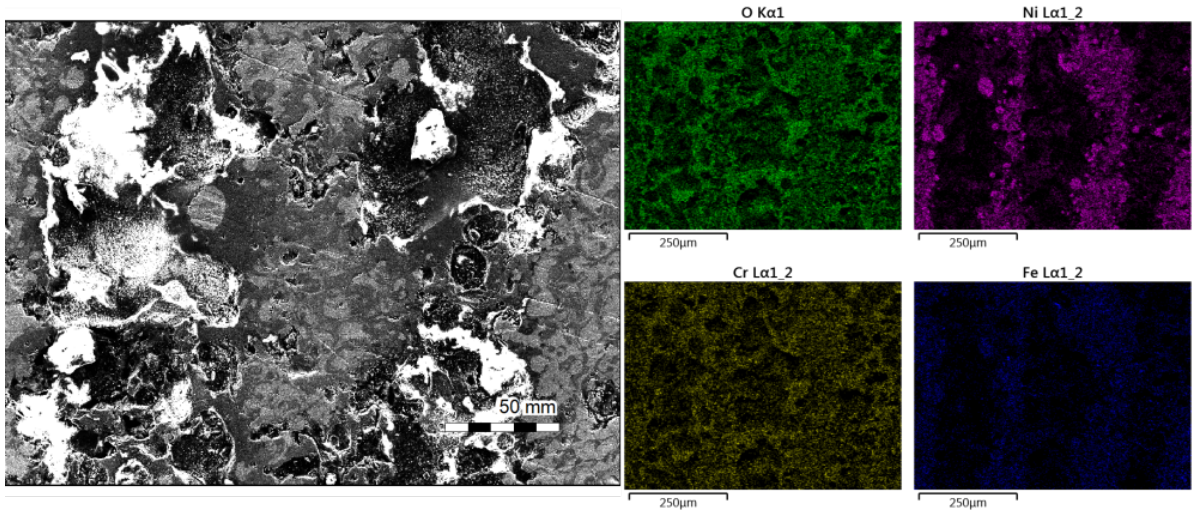


Figure 4.13: A SEM image and four EDX elemental maps of the distribution of Ni, O, Cr and Fe of two laser ablated rastered lines each at 25W and 300mm/s with a 0.2 mm spot size.

For further examination, this the sample has been ground to remove the upper layer of the sample. This allows for more detailed information of the variation of elements to be taken. As expected there is the milky region around the polished raw sample between the laser lines. Within the laser lines there was a high amount of charging of the surface so the electron image is not perfectly clear. It is observed that there is a definite melting taking place in the laser lines and a clear heat affected zone.

Within the heat affected zone there is a dark pattern with a round light circle, this is likely a metallic globule. The rough laser line sample shows less Nickel and Iron in the laser ablated sections and there is an increase in the oxygen indicating an increase in the oxidation in the area.

Within the Nickel elemental image, more of the metallic globules can be seen. These regions coincide with the iron elemental image too thus these regions are likely to be Iron and Nickel alloys. The Cr elemental image indicates some ablation of the Cr with the Cr being well dispersed throughout the sample and not present in the metallic globules.

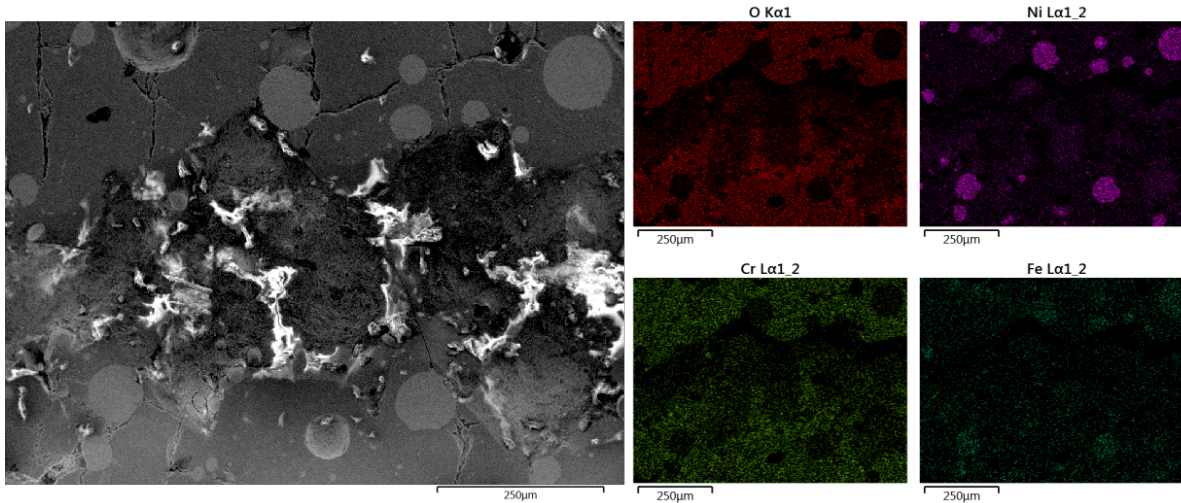


Figure 4.14: A SEM image and four EDX elemental maps of the distribution of Ni,O,Cr and Fe of a polished laser track ablated with a continuous laser at 25W and 300mm/s with a 0.2 mm spot size.

To inspect the heat affected zone of the laser further, a higher resolution EDX image of a laser track has been produced, which is seen in figure 4.14. This shows more of the metallic globules in the heat affected zone and a greater contrast between the laser line and the heat affected zone.

The major difference between the unablated element and the laser treated element seen through the SEM images is the change from the milky pattern to the dark oxidised regions with metallic globules pattern. The hypothesis is that as the laser interacts with the area and as the temperature rises the metallic regions (mainly Ni and Fe) are ablated preferentially.

Due to the thermal spray there are some regions of pure metallic particles within the film. These are ablated and oxidised at the same rate as the other regions, however, since they have such a high metallicity the proportional decrease in metallicity is undetectable. This leads to a darker oxidised region and the lighter metallic globules. From observations when comparing the heat effect of the laser line to the unaffected element sample, there is a clear gradient going from dark to lighter milky pattern. This shows the stages in the formation of the darker spotted pattern from the milky pattern. The nickel regions become smaller and more round and the oxidised area becomes darker.

4.6.1 Summary of the Experimental System Design Experiments

There are a variety of effects of the laser on the material. The material was shown to have a high surface roughness with a large degree of inhomogeneity. This puts a limit on the ability to predict the depth and mass of ablation. As a result the depth of focus of the laser had to be larger than the surface roughness in order to ensure the fluence applied to each part of the material is predictable and constant. The material appears to strongly absorb the laser radiation shown by the melting and vaporisation of the film with a variety of fluences of laser power.

It was found that the Nickel and alloys in the film when heated are oxidised and preferentially ablated in comparison to the oxide regions. This was found through comparing the elemental density maps of the material in regions that have been ablated and that have not. This in addition to the XRD data gives good indication of this hypothesis.

In addition a range of laser fluence that the laser produced suitable effects on the material were produced of between 0.75-1.17 J/mm². It was found that the higher the laser speed the lower the heat affected zone. As a result it was prescribed that the lowest stable interaction time between the laser and the material be specified. This provides a baseline for designing a system that can match these specifications and sourcing and manufacturing the components to build it.

4.7 Processing Method Design Model

Through analysing the literature and these experiments a model was produced for how the laser ablation of the film can be used to improve the uniformity and distribution of heat output of the elements. The various variables available to change in the laser ablation process are the speed or time that the laser interacts with the surface, the amount of energy delivered to the work-piece, and the locations that the laser interacts with. It follows that areas with more interactions over a longer time with greater amount of energy receive the most energy applied and thus treatment amount.

It was drawn from the data that the processing method used must not significantly cut off the current paths through the element. This is because the cutting off of the current flow can lead to in-homogeneous temperature profiles from the current avoiding areas of higher resistance. Finally, the laser processing needs to be selected so that the laser damage and oxidation is reduced to avoid the increase of total element resistance.

The method developed to account for this was to use the laser to deliver pulsed treatment onto the element with the density of pulses higher in areas with a lower temperature compared to the rest of the element. The condition is that the laser pulses must not penetrate the whole film, this is so an electrical connection over that space is maintained.

This model means that the current density in the areas that were at a lower temperature is higher and through the equation 3.3 the power output of those regions increases. This has the additional benefit of reducing the power output of the hotter regions compared to this area thus increasing the uniformity of the temperature profile on the element. This is further explained and implemented in greyscale pulsed output implementation subsection.

Chapter 5

Implementation of System Design

The initial tests were done on a research CO₂ laser, this section details how the design specified by the tests on the research equipment were implemented. When implementing the design, it was important to incorporate the theoretical and the experimental data so that the optimal system could be designed and manufactured. This chapter details how these two considerations came together so that the system could be implemented. The chapter concentrates on the two major components in the system the infrared camera and the laser tube and how through the software implementation these two systems work together.

5.1 System overview

The preceding sections provide the justifications and outline the process of developing the system and analysing its effectiveness. First the connections between the components are mapped out, this is shown in figure (5.1). This can be used in conjunction with the flow chart of the treatment process in figure (5.2) to understand how the system operates.

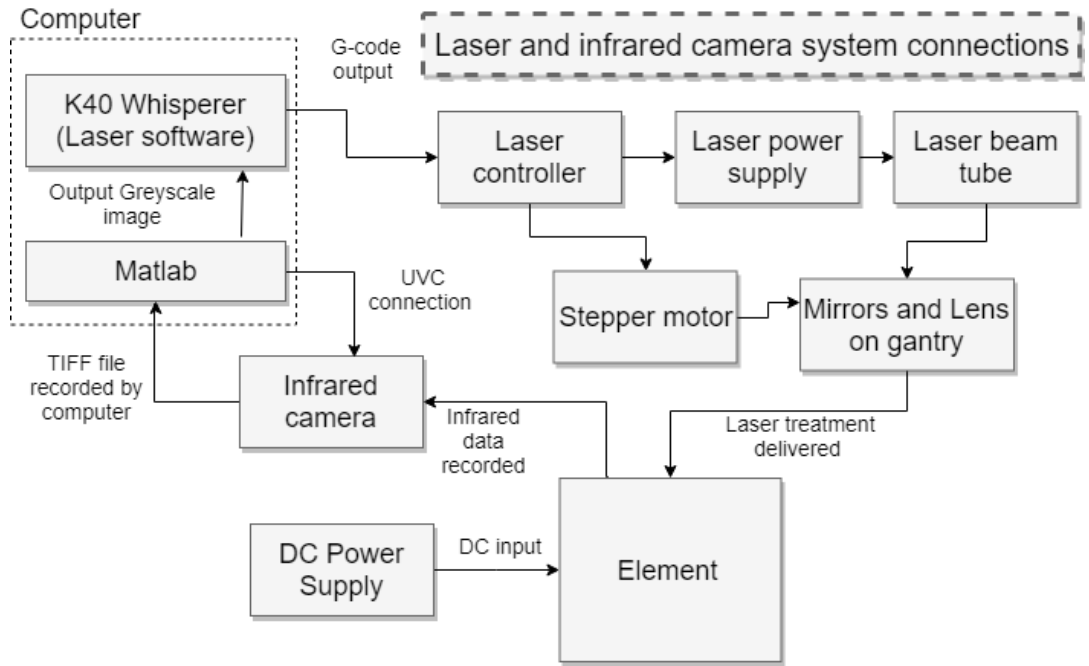


Figure 5.1: This diagram shows how each component communicates with each other to achieve the laser treatment of the element.

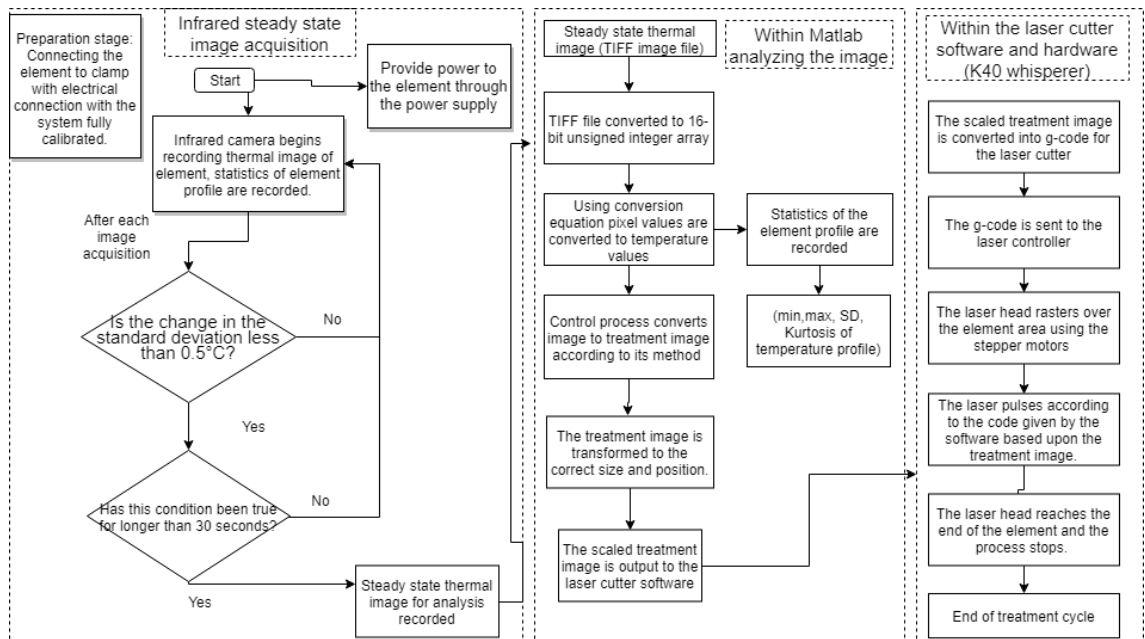


Figure 5.2: Flow chart showing how each process in one treatment cycle operates procedurally.

5.2 Infrared Thermography

Thermography is the photography of thermal images using the distribution of infrared light emitted from objects as a result of their temperature. Using these images the average temperature of each region designated by a pixel can be found. Within this project the thermal camera was pivotal in the sensing of the surface temperature profiles of the element. This was required for the characterisation of the element thermal non-uniformity, the implementation of the laser processing methods to alter the elements as well as the characterisation of the statistical change to the element surface temperature distribution.

Black-body radiation is the characteristic radiation from an object due to the thermal vibrations of its electrons, it is emitted with a characteristic, continuous frequency spectrum that depends only on the body's temperature. The peak of this distribution is generalised by Wien's law which is given in Eq. 5.1 [50].

$$\lambda = \frac{b}{T} : b \approx 2900 \mu\text{K} \quad (5.1)$$

The intensity of infrared radiation emitted in a region depends on the temperature as well as on the features of the surface material, a factor is introduced into the equations for black body radiation to account for the material surface. This ranges from 0 to 1 where 1 is defined as a perfect black body which emits and absorbs radiation.

The definition of emissivity is shown in equation 5.2 , this states that light incident on a object is either absorbed, transmitted or reflected from the object, the proportion of light that is absorbed is the emissivity factor [50].

$$\epsilon + \rho + T = 1 \quad (5.2)$$

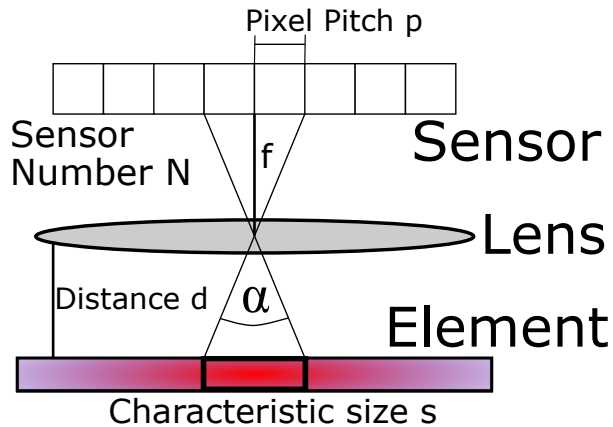


Figure 5.3: The apparatus of the thermal camera visualising the heating element, with the key variables in the spot size effect displayed.

Careful choice of emissivity of material is important as if chosen too high, the infrared data may display a temperature value of the heater lower than the real temperature. In addition reflective surfaces carry the risk of inaccurate measuring results by interfering infrared radiation emitted by background objects.

The factors effecting emissivity are the temperature of object, measuring angle of camera, geometry and surface roughness of the surface, thickness of the material, oxidation of surface, range of the measurement, and transmissivity of infrared by the film ([50],[51]).

The film examined has a highly rough surface, this is shown within the optical microscope cross sectional images in figure 3.1. A rough surface has a greater interface contact area, which results in less reflection, greater transmission and greater absorption of light. Therefore, emissivity increases according to equation. 5.2.

For this reason the expectation is that the surface has a high emissivity to infrared radiation. Using data for rough thin samples of oxidised Nickel the value of emissivity is 0.9 ± 0.2 ([50], [51]).

The spot size effect in infrared optics is where a minimum pixel density is required within a sensor to be able to distinguish the temperature difference within a region on an object a set distance away. The spot size is how much area each pixel covers on the target an diagram of this is visualised in figure 5.3.

Generally it is considered that five pixels within a region allow the region to be resolved. Using equation 5.3 and the camera specifications the maximum distance from the element that the infrared camera can go before this effect limits observation can be calculated, this is found to be 700mm.

Using this equation the amount of pixels upon each mm of the element is approximately 0.68 with slightly less pixels on the extremity of the element due to the lens distortion. This is accounted for within the removal of the lens distortion step.

The thermal camera puts some limitations on the resolution of the laser output, for this reason the laser device can only make general changes on the order of this scale. The interpolations steps add a blending of the layers so that the laser output is a continuous scale with steps every 0.1mm which is the maximum resolution of the laser beam instead of the approximate 1mm scale given by the raw output of the thermal camera.

$$N = \frac{df}{sp} \quad (5.3)$$

The error in all of the temperature measurements is given by adding all of the errors within each factor together in quadrature, the factors added together are the error from emissivity differences, ambient temperature, transmittance, Camera response, calibrator (blackbody) temperature accuracy. The result of this is an error of 0.5°C.

5.3 Infrared Camera Integration

A FLIR Lepton 3 sensor was used to record thermal data. The sensor is controlled by a control circuit manufactured by GroupGets. An image of the sensor coupled to the control circuit is shown in figure 5.4) this is comprised of a VOx (vanadium oxide) microbolometer which is sensitive to long wave infrared (8-15 μ m) radiation, a thermal image processor and a USB communication interface.

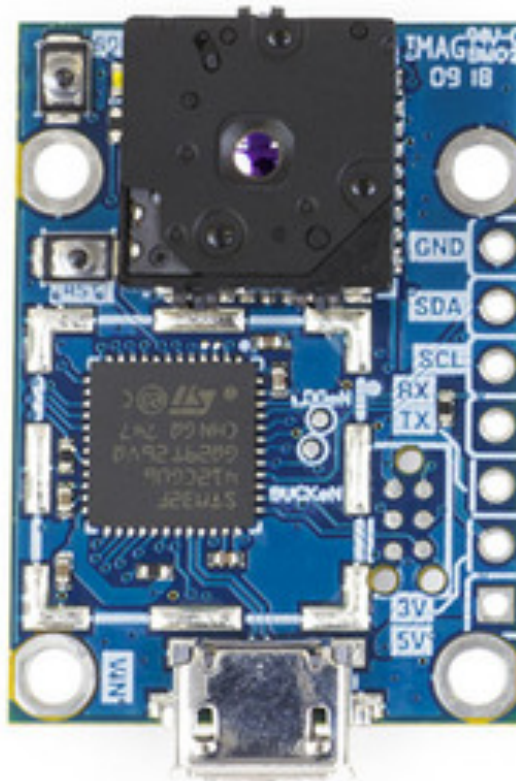


Figure 5.4: Image of the infrared sensor and control circuit which is 2.2x3cm in size.

The thermal data goes through the Thermal image processing before it is transferred via USB video device class (UVC). The CCI (command and control interface) is a control interface used to carry out functions with the Lepton and the VoSPI (Video over SPI) is transferring an image data to the platform.

The resolution of the sensor is 160 x 120 pixels with a pixel size of 12 μm . Pixel size is the size of one side of the square shaped sensor that measures the pixel value. The thermal precision is 0.5°C, data is scanned progressively before processing and being send to the computer via communication protocols.

The sensor has a black body shutter attached which communicates with the control board to adjust the camera. There is an internal thermocouple which is used to find the temperature of the camera and the scene, as the temperature recorded from the scene depends on the temperature of the camera.

The processing of the raw sensor data was done through the STM32F412 ARM micro-processor within the circuit board. The data from the sensor is processed within the circuit board, as various transformations need to be applied to the data to output raw image data with the pixel values linearly proportional to the scene temperature.

After processing the sensor data, a variety of data types that can be produced with the thermal camera; raw 14 bit data, scaled 8 bit data and scaled 24 bit colour data. For the purpose of this project the raw 14 bit data is taken and send to the computer so that further analysis can be done on the faster processor within the computer. Subsequently, this raw data needs to be calibrated to the correct temperature.

The VoSPI protocol is used to transfer image data, this has a maximum of 8.8 frames per second. One frame is 60 packets, 4 segments with a size of 38.4 kB. Each packet is indicated by a packet number and the 20th packet number contains a segment number as its header. The image data is sent in chunks of packets so that three chunks are needed for each image to be produced.

US export regulations for thermal cameras stipulate that any thermal camera exported from the United States of America for non-military use to countries that are signatories of the Wassenaar Agreement are locked at less than 9 frames per second. In order to be compliant with this regulation, the frame rate is lowered by sending the same frame three times [41].

This can cause problems with the acquisition of data when images are queried at a frame rate faster than 9 fps. To manage this, a limit of a minimum time interval of 0.5 seconds is used to avoid data loss and experimental errors from device malfunction.

5.4 Infrared Camera Calibration

5.4.1 Flat Field Correction to the Thermal Camera

Bolometer thermal sensors experience drift over time which leads to systematic errors as the temperature measured by the sensor will either be lower or higher than usual. As a result, the sensor requires re-calibration or refurbishment. A technique to remove this process is a blackbody correction [52].

This process is where the camera images a perfect black body material at a known temperature upon which the camera can then adjust its output. This process is integrated within the thermal camera through a shutter on the front of the lens. This process is carried out for all the pixels in the sensor as the drift in the sensor can be nonlinear. This process is repeated before every cycle as the image data is processed. Since the time for this process to take place is less than the time for the image data to be processed, there is no increase in the processing time of each cycle.

5.4.2 Temperature and Emissivity Calibration

In order to correlate the temperature displayed in each pixel by the thermal camera and the temperature of the element in that pixel a calibration process was required. The calibration process used other thermometry devices to correlate the temperature seen by the thermal camera to itself, these devices were a spot infrared thermometer and thermocouple thermometer. These thermometers record the temperature of an element emitting heat in a steady state before the thermal camera records an image of the element and the temperature of the region measured by the other thermometers.

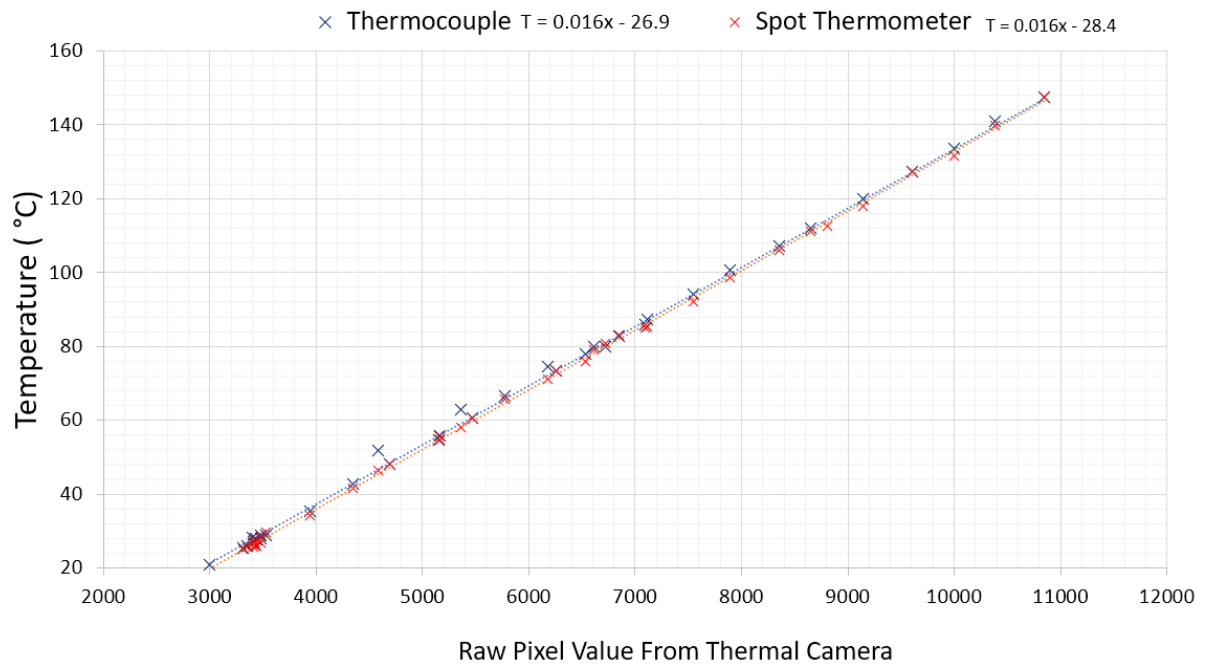


Figure 5.5: Graph of the pixel value of the sensor against the values measured by the spot thermometer and the Thermocouple with linear fits added.

The raw value from the sensor is recorded to generate the temperature calibration graph. This calibration is shown in figure 5.5. The data shows good agreement between the linear fits and the experimental data. An average fit was taken from these plots with the equation of $T = 0.016P - 27.5$, the error in the temperature is $\pm 0.5^{\circ}\text{C}$ from the average residuals of this fit to the experimental data. This equation is used in the imaging processing to convert between the pixel values determined by the thermal camera to a temperature value.

The emissivity of the element is set to a standard blackbody of value 1 throughout the experiment to assure that throughout the course of the experiments the temperature data is always recorded with the same bias applied. Since all the temperature measurements are recorded for the same material (the element). It is also assumed that the laser processing does not alter the emissivity of the surface. This is justified in the optical experiments looking at the surface changes of the element from the laser ablation.

5.5 Software Implementation

5.5.1 Image Acquisition

To implement the processing method the first stage is taking the image, this is done through the use of MATLAB® Support Package for USB Webcams, this allows MATLAB® to bring live images from any USB Video Class (UVC) webcam into MATLAB®. The output from this is a 16-bit unsigned integer class file, this contains temperature data for every pixel recorded by the camera, this can then be analysed and transformed with the tools within MATLAB®.

5.5.2 Image Processing

The image used for ablation was captured after the temperature profile of the element was determined to be at a plateau. A plateau is reached when the average standard deviation, max, median, and mean temperatures fluctuate about their mean value with a fluctuation of less than 0.5°C. This was determined by finding the change in standard deviation of the element as the element is heated.

This image is then interpolated using a Bi-cubic algorithm. This was chosen as the interpolation surfaces in bi-cubic interpolation are smoother and have fewer interpolation artefacts compared against nearest-neighbour or bi-linear interpolation [53]. A negative aspect of using bi-cubic interpolation is the higher computational power required compared to similar interpolants [54]. However, it is on the order of a tenth of a second for an image of 160 x 240 pixels to be processed, therefore it is considered to be a small but non-trivial addition to the processing cycle.

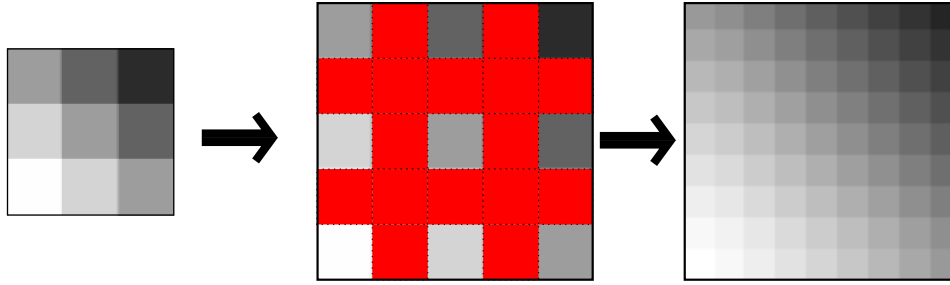


Figure 5.6: Diagram showing the result and the area of influence of bicubic interpolation on a sample greyscale image.

Bi-cubic interpolation considers 16 pixels (4x4) and uses the weighted average of the four translated pixel values for each output pixel value. The bi-cubic interpolation method fits a surface between four corner points using a third order polynomial function, this guarantees the continuity of the first derivatives, as well as the continuity of a cross-derivative.

This was important as interpolation is used to approximate the heat diffusion in solids between the pixel values. The first derivative of the heat equation is continuous thus the interpolate must have a continuous value between between interpolated regions. The interpolated surface, $f_i(x, y)$ [53] is defined by :

$$f_i(x, y) = \sum_{i=0}^3 \sum_{j=0}^3 a_{ij} x^i y^j \quad (5.4)$$

The 16 coefficients of a_{ij} are determined in order to compute $f_i(x, y)$. Four are determined from the intensity values in the four corners; eight are determined from the spatial derivative in the horizontal and vertical directions and four of the coefficients are determined from diagonal derivatives. An example of the bicubic interpolation of a greyscale is shown in figure 5.6. This shows how the red sections are filled by the addition of new data.

The bi-cubic interpolation was used to minimise pixelation of the thermal image when the element area is cropped. Pixelation reduction is crucial to match the laser scaling when the image is increased in scale. If the raw pixel images are used then hard borders are added to the output because the pixel size is larger than the laser resolution. Reduction of artefacts and roughness is important to prevent the laser power from rapid fluctuation, so that the effect on the surface is smoother. This reduces the chance of burnout as there are less regions with a disproportionate amount of ablation.

5.5.3 Selection of the Region of Interest

In the next step, the element was cropped around its edges using a polygon where the edges and corners of the element were selected. Automation in this process is possible as the algorithm can recognise the elements in the image either through machine vision or by the intensity threshold. However, due to the low contrast between edges in the thermal images, a lack of time to train a neural network, and since the elements do not move from test to test manual selection was preferred.

The image of the element was then placed within the correct position and a scaling applied to ensure that the image is the same size as the output scaling of the laser cutter. After the scaling was correctly set, the relevant specific processing method algorithm was applied to select regions and treatment depth within the image. Subsequently, the image was saved and output to a Portable Network Graphics file which is then converted into a Scalable Vector Graphics file so that the units of the image are set (mm). This then leads to the final step in this process, the laser path being sent to the laser machine controller.

5.5.4 Image Distortion Calibration

Due to the lens on the infrared camera, there is some distortion to the size of objects in the image particularly at the edges of the image. This problem compounded itself, as the element needs to take up the maximum amount of the image to receive the maximum resolution of the element so the element takes up most of the size of the thermal image. This means where the distortion is the greatest at the edges of the lens thermal data is being taken.

To remove the distortion in the camera, a calibration procedure was implemented. The calibration of a camera takes place by measuring images of a chequerboard with known and regular distances between the chequers. The MATLAB® Computer Vision System Toolbox was implemented to identify the location of the vertexes of the chequers, from which it finds the distances between the projected chequers and the imaged chequers length at various positions in the image. By comparing the distance between the corners of the chequers within the image and the projected corners the distortion of the image across the whole angle of the lens is found.

To adapt this process to an infrared camera, an acrylic chequer board has been produced with a laser cutting machine where the white squares of the chequerboard are being cut out. Contrast between the white and black sections on the acrylic chequerboard are produced by placing the chequerboard on a powered heating element. Since the cut out sections of the chequerboard are hotter than the acrylic surface, they appeared brighter in the thermal image. This leads to a contrast between the acrylic squares (black squares) and the cut out sections(white squares). Figure 5.7 shows an image of a chequerboard illuminated by infrared radiation and imaged by the thermal camera.

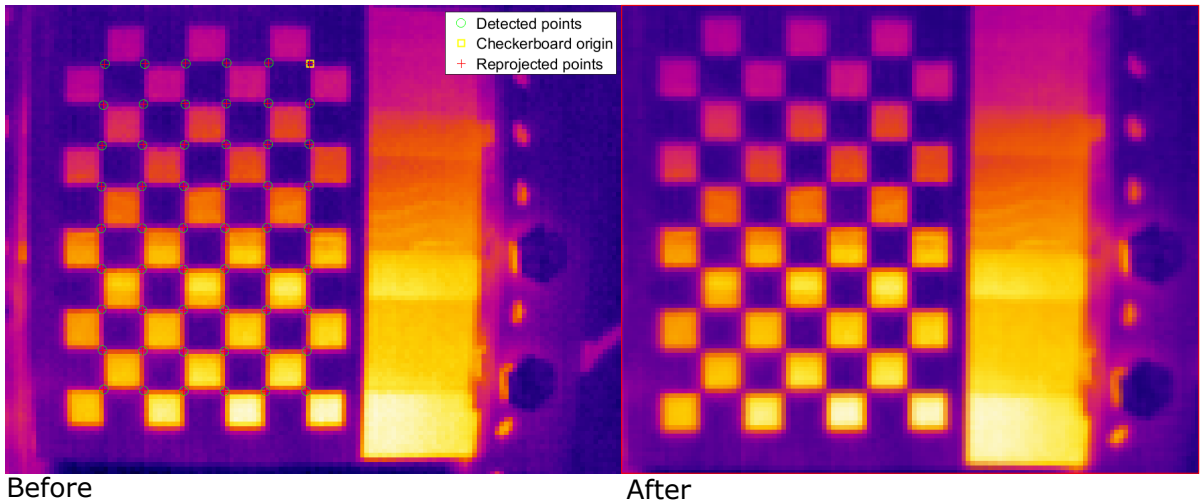


Figure 5.7: Comparison of the images before and after lens calibration with the corners of the checkerboard indicated by the calibration algorithm.

The acrylic has a thickness of 5mm and strongly absorbs infrared radiation, this was tested by placing acrylic in front of the camera and infrared radiation cannot be detected behind the acrylic sheet. These findings are in agreement with the literature showing PMMA to have strong absorption across the infrared spectrum [31].

Due to the acrylic absorbing the infrared light, the cut-out spaces in the checkerboard appear bright in the image and the acrylic squares dark, this allows for the recognition of the corners of the chequers and thus the calibration of the thermal image to account for lens distortion. The measured distortion parameters have an error of 0.08 pixels (0.07mm), which means there is a direct translation between the position of pixels in the image and their actual position within this error. Figure 5.7 compares the distortion in the thermal image before and after the calibration has taken place showing how the distortion of the image is removed.

5.5.5 Image Scaling

The image taken by the camera is at a pixel scale which requires the dimensions of the objects in the images to be defined. As a result, the image needs to be scaled so that the output image is equivalent to the scale of the laser. Therefore, a translation of the image within the image area is necessary so that the laser interacts with the correct position on the work-piece. An expansion transformation was applied so the unit pixel length equals the unit length that is output by the laser. The size calibration was

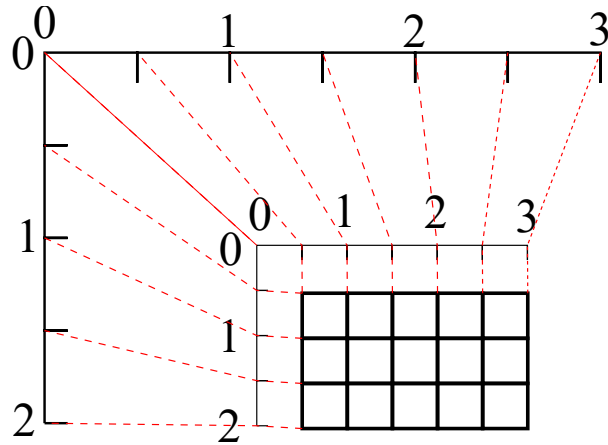


Figure 5.8: Image showing the transformation of the thermal camera pixel coordinates to the laser coordinates.

done by comparing the positions of the chequerboard to the grid of the laser axis. An image of this process is displayed within figure (5.8)

Each corner of the chequerboard is compared against the position in the thermal image and the laser axis. Figure (5.9) shows a graph comparing the y and x axis of the corners of the thermal image and the laser axis. From this comparison, an equation can be generated for the transformation of the x and y axis between the thermal image and the laser axis. This is $0.75 \times$ the thermal image pixel coordinate ($+13.6(x)$ and $+21.3(y)$). This equation was used to adjust the position and size of the cropped image from the analysis of the thermal imagery to their position within the laser machine axis. When the transformation of the image took place, the Bi-cubic interpolation was used. It was considered valid to use this transformation as the linear fit between the pixel value measured and the value of the laser coordinate show good agreement.

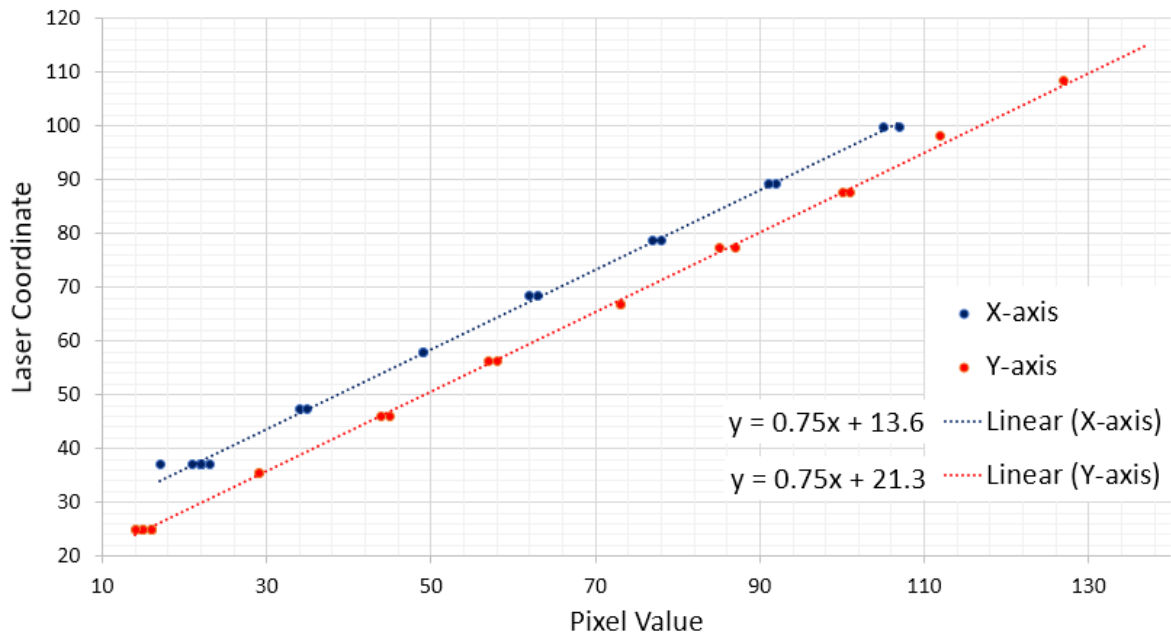


Figure 5.9: A graph comparing the positions measured in the laser grid and the positions measured in the thermal image.

Every time the thermal camera position is moved this transformation must be altered as the height is changed the gradient of this graph will change. Subsequently, as the position in the x and y axis of the camera changes the intercept value will change. The intercept value also measures the position of the origin of the thermal image in the coordinates of the laser so for this calibration the origin of the thermal image is at the (21.3,13.6)mm position. The fact that there is a linear relation between the pixel and the laser cutter coordinate shows that the distortion calibration is successful in removing the distortion of the lens from the images.

5.6 Laser Control Engineering

5.6.1 Laser Gantry Control

The gantry is controlled by two stepper motors on each axis. The steppers are rated for 4.7 V at 1.0A, with phase resistance 20 Ohms. The step Angle is 1.8° which equates to 200 steps in a rotation with a precision of $\pm 5\%$. Using these values the precision of the x and y axis driven by the stepped motor is found to be $0.01\text{mm} \pm 5\%$. An image of the gantry with the mirrors attached is shown in figure 5.10.

The lens and third mirror is attached to what is called the laser head, the place where the beam is reflected downwards to the work piece and then focused by the lens. This is held para-axially to the mirror on the end of the y axis arm, which is the second mirror. The second mirror is held at 45 degrees to the y axis arm and the first mirror, this is so the beam reflects on the second mirror after hitting the first mirror and hits the third mirror in the laser head. After the laser beam leaves the laser tube it hits the first mirror, this is held at 45 degrees to the laser tube so that the beam reflects from this mirror and hits the second mirror which undergoes the process outlined above. This is all controlled and operated within the software of the laser system.

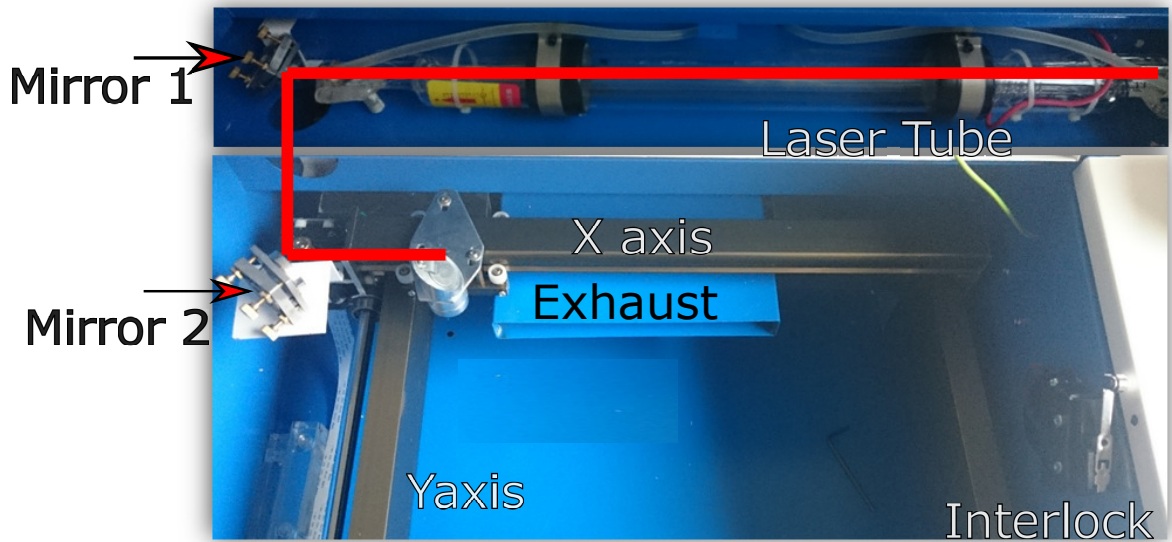


Figure 5.10: Laser path and gantry design without worktop placed within, the laser tube is roughly 1m in length with the gantry area encompassing 200x300mm.

5.6.2 Software Path Control

The program K40 Whisperer is an open-source software which interfaces to the controller in the laser machine [55]. A laser path image is coded into g-code for the laser cutter to execute through the K40 Whisperer software. There are a variety of modes available, cut, etch, and dither. For the majority of the research the dither mode is used, as it breaks the laser path area into scan lines and then, according to the colour of the image on a greyscale, alters the duty cycle of the laser. The duty cycle is defined in equation (5.5) [56]. The time for the pulse is signified by t_p , the time between the next pulse is given by T . This serves as a measure of the ration of the time the laser is on.

$$Dutycycle = \frac{t_p}{T} \quad (5.5)$$

What is important for the application of this research, since the pulse length is fixed, is the position of the pulse of the laser not necessarily the time between them, since the laser head moves at a consistent speed of 300mm/s this can be related. This is what the software within the laser system does the positions specified by the images given by the matlab code is decoded into g code so that the pulses are sent at the correct time so that the pulses are in the correct location. This is done by the laser software altering the duty cycle as it needs. This means that the correct amount of pulses per length of each pixel is output onto the workpiece. This is found from the value of the greyscale value in the picture given to the laser system software.

The laser pulse length for the pulsed regime is set by altering the greyscale value in each pixel where the laser follows the raster over an area which in the image is given to the laser to ablate. Since the time that the laser pulses over is proportional to the distance covered by the laser, the speed of the laser must be specified to specify the pulse time to find the duty cycle. The speed of the laser is chosen to be 300mm/s, the highest speed achievable by the system in use. This allows for the duty cycle to be calculated for the desired overlap of laser pulse.

5.7 Laser Processing

5.7.1 Laser profile

To measure the laser profile, the visualisation of the laser effect on acrylic was undertaken. This was achieved by pulsing the Laser on the acrylic multiple times at various powers in a line on the acrylic and looking at the resultant pattern. An image of these laser pulses is given in figure 5.11. This data was used to find the average laser width as 0.13 ± 0.01 mm.



Figure 5.11: Laser pulses onto acrylic media in a line set to only just overlap. Each pulse has a width of $0.13\text{mm} \pm 0.01\text{ mm}$ which corresponds to the beam width.

It is assumed in the laser section that the laser has a Gaussian like shape. This experiment finds evidence that indicates that the beam indeed follows a Gaussian like shape as the laser marks show a spherical interaction with a higher power density in the centre. This shows that the energy density of the laser is largest within the central region which is the Gaussian approximation.

5.7.2 Laser Power Output and Delivery to Worktop

The power output of a laser, if not properly calibrated, can be non-linear. The test described in this chapter has been undertaken so that the power of the laser beam can be stated in terms of Watts and not a percentage of the maximum value. This enabled the analysis of the threshold fluence of the laser and gave a more representative value of the power output. Figure 5.10 shows the gantry layout of the laser. To carry out these tests a CO_2 power meter was placed between the laser tube and mirror 1.

Each test of the power was repeated three times. This particular power meter takes a data reading over 60 seconds per trial, the reading for the power meter is taken by comparing the temperature of a sensor encased within itself before and after the trial. The temperature rise of this sensor is then correlated to the power of laser by a scaling equation, this is calibrated from the manufacturer and they assert that the power measurement is accurate to $\pm 1\%$.

The data for this test is shown in 5.7.2. Two fits are made to the data, in the range 20-40% a linear is used with the equation 5.6, within the range 40-70% a log fit is used, the equation for this is described by equation 5.7. Both lines overlap with the error bars and follow the range of data within the respective ranges, thus the data shows that these fits are appropriate.

If the linear fit is extrapolated towards the x axis the value of the threshold power percentage is $5.6\% \pm 2\%$, the minimum power that the laser can pulse at is 15%, this means that the range of power available for experimentation are 12-28W of average power output. This is the raw output of the laser tube, due to losses in the mirrors there is a lower output of power being delivered to the worktop.

$$y = 0.8x - 4.5 : 15 < x < 40 \quad (5.6)$$

$$y = 17.2 \ln(0.133x) : 40 < x < 70 \quad (5.7)$$

This data was repeated at the end of the project and data was found that indicated that the laser tube had not lost power over time, this shows that the water cooling system is efficient in its role of protecting the laser tube from damage.

Power of the laser at various percentages selected on the potentiometer.

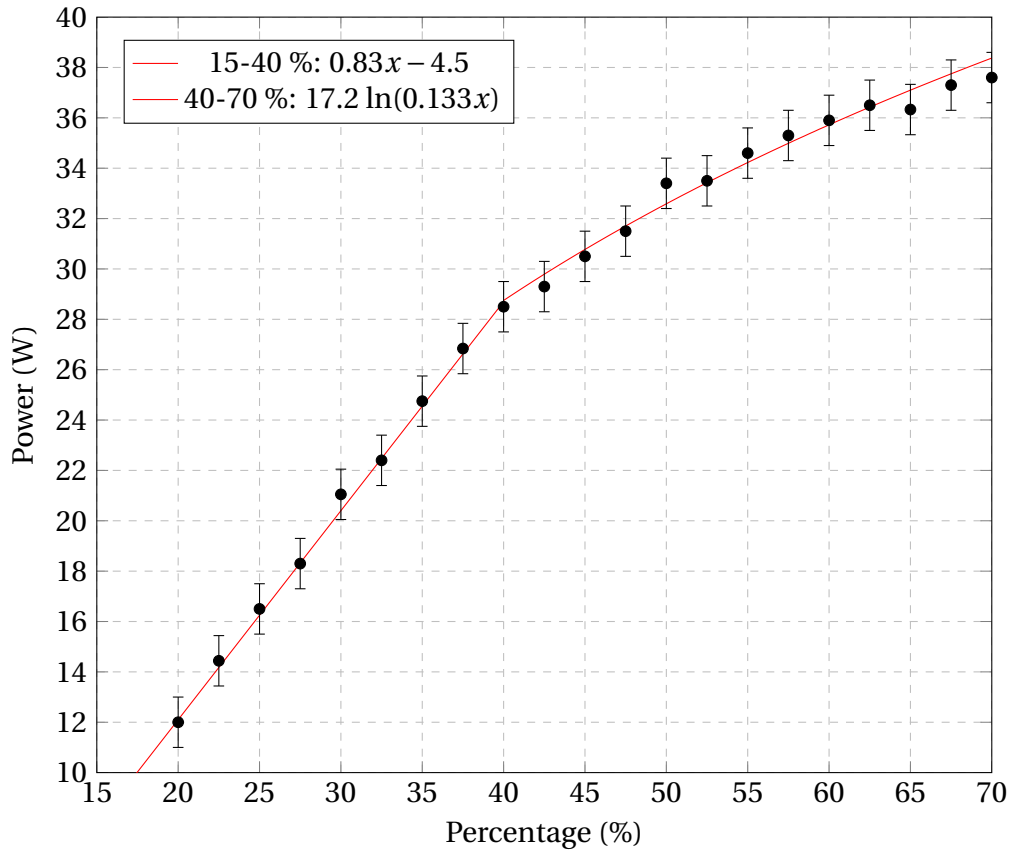


Figure 5.12: Graph displaying the power of the laser at various percentages of power selected on the manual power selection knob. Y-axis error bars due to the uncertainty from the power meter recording.

5.7.3 Mirror and Lens System

Molybdenum mirrors are used to reflect the beam of light, these have a maximum reflectance of 98.9% to infrared radiation showing that they will reflect a high proportion of the infrared radiation, this value can be lower in practice due to defects on the mirror, the alignment of the mirror, and particles on the mirror absorbing some of the radiation [57].

It was important to keep the mirrors clean at all times, as in case the laser is incident on a unclean mirror the mirror will absorb more of the energy of the beam which would result in the mirror temperature to increase. The increase in temperature on the mirror can cause damage and warping of the mirror, worsening its performance in the future.

In addition, Molybdenum mirrors are tougher, having high melting points (in the eventuality some dust does get on their surface), and thus require cleaning less often compared to silicon and copper mirrors. This means cleaning can take place before every day of laser tests rather than after each individual laser test.

A Zinc Selenide (ZnSe) Plano-Convex lens is used with a 50.8 mm focal length. The transmission of ZnSe to infrared radiation in the 10.6 μm is 88%, this is shown in 5.13 [58]. This type of lens was chosen because ZnSe lenses have the greatest transmission of infrared per cost of the lens thus the greatest value for the project as well as being affordable to replace if damaged. In addition, since there were a wide range of laser power available to the project a lower efficiency of lens is acceptable as to gain the same output of power the input power from the laser can be increased.

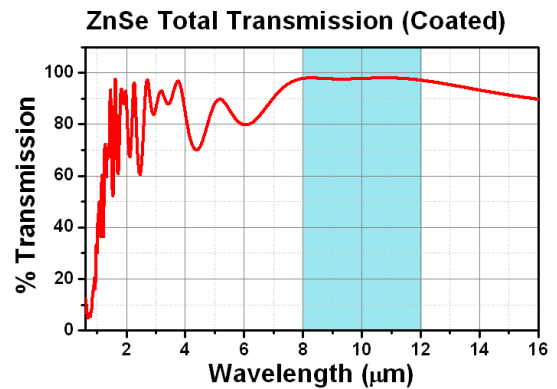


Figure 5.13: Transmission of infrared radiation through a ZnSe lens [58].

A 50.8 mm focal length of lens was chosen as a compromise between the depth of focus and the size of the spot of the laser beam; A Plano-Convex lens with a 50.8 mm focal length will have a depth of field of approximately 2.54 mm which is larger than the error in the height of the work-piece to the lens with the error in the surface roughness taken into account. A ZnSe lens is also resistant to damage from thermal variation[58], this improves the robustness of the system so that heavy lasing can take place without having to take potential damage to the lens into account.

Similar aspects to mirrors also exist for lenses with regard to cleanliness. The lens must be kept clean, thus before a days testing the lens is inspected and cleaned to remove any particulate. Within the inspections it was not found that there was a visible deposition of material on the lens, nevertheless the lens was cleaned before starting the tests.

5.7.4 Mirror and Lens Radiation Transmission Efficiency

The efficiency of laser output and mirror reflection of the laser tube was investigated with the use of the power meter. The power of the laser was examined with the power meter held perpendicular to the beam, each measurement was repeated three times. Figure 5.10 shows the gantry layout of the laser. The beam power was tested after the laser tube, after the first mirror, after the second mirror, and after the third mirror. The power meter must be held under the laser beam for 60 seconds, this measurement is accurate to $\pm 1\%$.

The data of power output recorded at the various positions along the gantry is displayed in table 5.1. The total efficiency of the laser output to worktop is calculated, this decreases as the power increases. The proximate hypothesis is that at higher powers the quality and cleanliness of the mirrors is a larger factor in the emission of radiation. This indicates an average efficiency of 91.4% for the mirrors, 86% for the lens, and an average total efficiency of $77\% \pm 3\%$ from beam to work-piece.

There is a variation in the efficiency of output for various power outputs, hence an expression is required to describe the efficiency at various powers so that in future experiments the power delivered to the work top is known to an accurate and precise value. An empirical linear equation can be established to this data, which is shown in equation 5.8 with an R^2 of 0.99. This overlaps with the errors in the values of the efficiency, follows the trend, and has a value of R^2 close to 1 giving an indication that this equation is a good fit to the data.

$$Efficiency(\%) = -0.17 * Power(W) + 83 \quad (5.8)$$

Table 5.1: Power output data of the laser tube.

Position in beam	16W (25%)	28W (40%)	34W (55%)
Mirror 1 to mirror 2	15.5	27.2	33.0
Mirror 2 to mirror 3	15.2	26.1	31.3
Mirror 4 to lens	14.8	25.3	29.9
lens to worktop	14.2	24.3	28.7
Total efficiency	91.3 %	89.4 %	87.1 %

Improvements to this data could be undertaken with a greater amount of experimental values obtained, but since the error in the power measured by the power meter is so high it would only provide a moderate improvement in the data. This equation is used in further analysis to find the power delivered from the laser to the worktop.

To find a relation between the percentage of power output selected by the laser and the optical output delivered to the work-piece equations 5.6 and 5.8 are combined by the linear equation 5.9.

$$OpticalPower(W) = 0.47(Percentagepower(\%)) + 0.76 \quad (5.9)$$

This equation is only valid within the range of percentage power from 20-40% as this is the range of validity of the linear fit used. This provides the tools to convert the percentage power used by the laser and the optical output.

5.8 Accessory System Engineering

For the safe, reliable and optimal operation of the automated ablation system a variety of accessory systems have been designed and implemented. These range from ventilation and cooling systems to alignment and safety procedures.

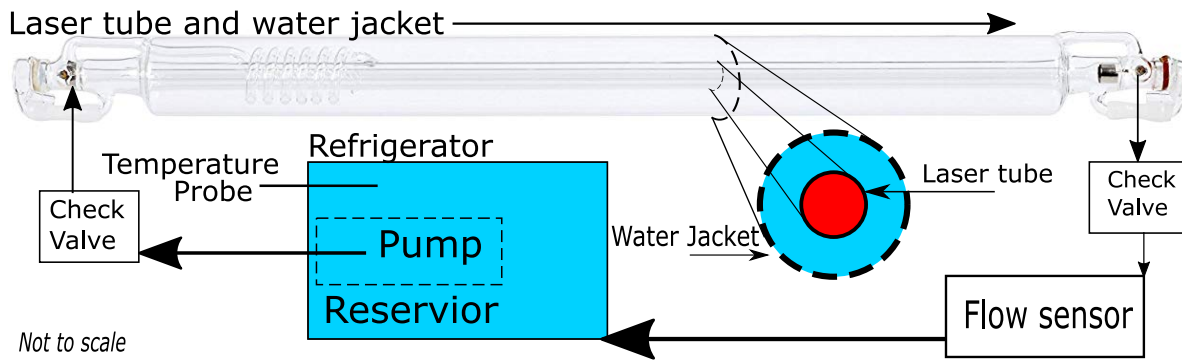


Figure 5.14: Components connected within the coolant system.

5.8.1 Laser Tube Cooling system

The cooling system of the laser tube is shown in Figure 5.14. A cooling system was vital for the laser tube, as when the laser operates the gas within the laser tube heats up, causing the CO₂ gas to disassociate.

As the laser tube is cooled the gas re-associates to CO₂[59]. This means the efficiency of the lasing decreases and the power of the tube decreases. Where temperature fluctuations are very high, the glass encasing the laser tube can undergo thermal stress and deform, causing deviation and power loss of the beam or even fracturing of the glass case.

The requirements for the coolant system are that the temperature range stays within 10°C to 25°C, the water flow at a minimum of 50L/hour, and the water stays free of contaminants ranging from mineral particulates, bio films, and other small objects.

The minimum of 10 degrees is set to avoid the glass casing from freezing when below 0 degrees. Due to the laser tube being non-insulated along its breadth and, as shown from figure 5.14, the water jacket is concentrically wrapped around the laser tube. If the water jacket is much colder than the surrounding area, then condensation will build upon the water jacket, which lowers the laser tubes resistance.

As the laser tube is under 12kV in operation, there is a chance if condensation builds up and finds its way through the insulation on the laser tube cathode that the tube will produce electrostatic arcs and damage the laser system with the potential of death for operators. In addition, even if the laser does not arc the condensation can become charged from the high voltage leading to the aforementioned results.

In order to ensure that the water bath stays within the specified temperature range, a plastic reservoir was placed within an insulated refrigerator by splicing the wires and placing valves on the opening of the fridge so that the fridge and pump can be connected whilst the reservoir is internally insulated. Holes are put in the refrigerator door for valves to take the output water to the laser tube and for the return of the water back to the reservoir. These valves are then tightened and insulated with silicone sealant to minimise convection flow of air from the reservoir.

Check valves are placed either side of the connection to the laser tube so that the water flows in one direction and to minimise the build up of micro bubbles within the water jacket. A flow sensor is attached to the system, so that before tests begin there is an indication if water is flowing within the system. Additionally, the flow sensor is transparent in its upper section, since this point is higher than all points of the laser tube air bubbles are being collected here, this allows for the operator to check if the water is flowing and if there are air bubbles within the system.

Air bubbles are a problem within water coolant systems if the system is not correctly designed or purged of air pockets. To avoid air bubbles, the laser tube is kept lower than all other parts of the coolant system. Due to air being a gas and therefore being less dense than water, it will raise to the highest part of the system, which is the reservoir.

When under correct operation, the laser tube does not contain any air bubbles and provided the system is left undisturbed none are introduced. This is validated from looking at the check valves and flow meter which serve as local maxima along the water path which reduce the build up of bubbles in the tube, collect micro-bubbles and when the bubbles in these sections become too large, they are being flushed through the system due to the surface tension and water pressure.

Distilled water is used within the water coolant system as it is free from bio-films and minerals. Minerals are important to remove from the water jacket as ion content in the coolant raises the conductivity of the coolant. If the conductivity of the water increases then static charges can build up, these create hot spots in the tube which can then decrease the integrity of the tube over time. The static charge can also interfere with the beam, making it deviate from its path, expand the beam size and due to less energy transferred to the lasing mechanism lower power output from laser in a non linear fashion.

At a 40W output the laser tube draws over 800W of power, thus when the tube operates at this level a minimum of 760W of power must be removed from the laser tube so that the laser tube temperature stays constant. Depending on the laser treatment the laser, when operated continuously, will have a load of several seconds of power drawn whereas in pulsed regimes the laser draws less power as the laser is off for half of its lasing time.

During preliminary tests, the temperature of the laser tube raises by 0.1°C per minute at a 40W output, to reduce the temperature of the reservoir to its original state it takes 5 minutes to cool the reservoir by 0.5°C, as a result it is concluded that the coolant system requirements are fulfilled by this design as the coolant system can keep the laser under the safe temperature conditions for multiple cycles.



Figure 5.15: Components connected within the ventilation system.

5.8.2 Ventilation System

During the process of laser ablation small particles enter the air from the laser vaporisation at the surface of the material, the components used to achieve this are shown in figure 5.15. The quantity, size, and toxicity of the particulates vary by the material cut, power used, and quality of surface. To connect the ventilation system to the laser system, a square to 4 inch dust extractor was attached to the back of the laser system as shown on the left of figure 5.15. Between the laser cutter and the dust extractor, a bespoke shim was manufactured to maintain an airtight seal, the duct is held in place with two rivets on the back the laser cutter, the seals of the ventilation system are then sealed additionally with a silicone sealant. The duct is then connected to the ventilation fan using duct tubing.

To ensure any operator is safe from any emissions, a constant airflow is required whilst the device is under operation. The safety criteria set from the safety department of Lancaster University determined that within one second all the air within the laser system area must be vented to the ventilation system.

The area of the laser system work space is $0.03m^3$, this would require a minimum speed of $108 m^3/hr$. To accomplish this a $200 m^3/hr$ fan was acquired and ensures the laser cutter is under negative pressure. The system vents into an activated charcoal filter wrapped within a HEPA filter, this conforms to HEPA standard of filtration to the U11 standard according to ISO14644-1 which dictates filtering out particulates $< 1 \mu m$.

Since there is some chance not all of the particulate is filtered, the filter vents on the outside of the experimental space filter the air to the environment. The estimated peak rate of particulate ablation when ablation is taking place is $0.01g/minute$, each cycle of the automated process took under 2 minutes to complete, a high portion of this was expected to be filtered thus the impact to the environment from this processing is negligible when compared to other processes such as the emission of car exhausts and industrial processes [60].

5.8.3 Interlock Safety System

An interlock safety system was important to implement within the laser machine as lasers are very high powered and produce focused energies; The eye is particularly sensitive to light radiation due to the lenses and exposed structures as well as the body being sensitive to burns from radiation. Additionally, due to the reflection of radiation, light damage can be caused in unexpected ways from stray reflection if the laser is operated with the lid open.

The interlock design works from a hard stop basis, which is implemented by a contactor relay wired to the switch so that when the switch is deactivated (lid opened) the relay is tripped and the contactor goes from an open state to a close state. This stops all the flow of electricity to the laser machine and can only be restored if the lid is closed and the power is manually reset with a button wired to the contactor.

5.8.4 Element Electrical Connection and Clamping System.

To maintain the electrical connection throughout the tests, the element sheet needs to be at the focus of the laser and the heater needs to be insulated so that it has a uniform thermodynamic load. This was achieved by designing a clamp system on its edges, figure (5.16) shows an image of the clamp design.

The choice of material for the clamp is acrylic (Poly(methyl methacrylate)), this was chosen as it insulates the element, electrically insulates the element from the case, and is resistant to the temperature changes of the element. In addition, the acrylic (PMMA) is opaque to laser wavelengths between 8-25 μm so the laser will be absorbed by the acrylic being cut by the laser and shielding components from the laser[31]. The top layer of the clamp is built from one large worktop of 6mm thick acrylic, this then holds onto the device with two clamp bridges. This is held up with pins at the focus height under the worktop. The location of the focus is just under the worktop height where the clamps hold the work piece.

The flatness of the piece of work was a key parameter to control. The clamp is able to reduce the bend in the piece of element by clamping along the edges of the element with parallel clamps, this provides tension along the element and increases the flatness. The difference in height of the edges of the element and the centre when clamped were $\pm 0.5\text{mm}$ as measured using a electronic inclinometer (measured a 0.2°) and taking length of the element into account. As the deviation is less than the waist of the focus of the beam, the clamp is adequate in restoring the flatness of the element so that the element bend does not have an effect on the laser ablation of the element.

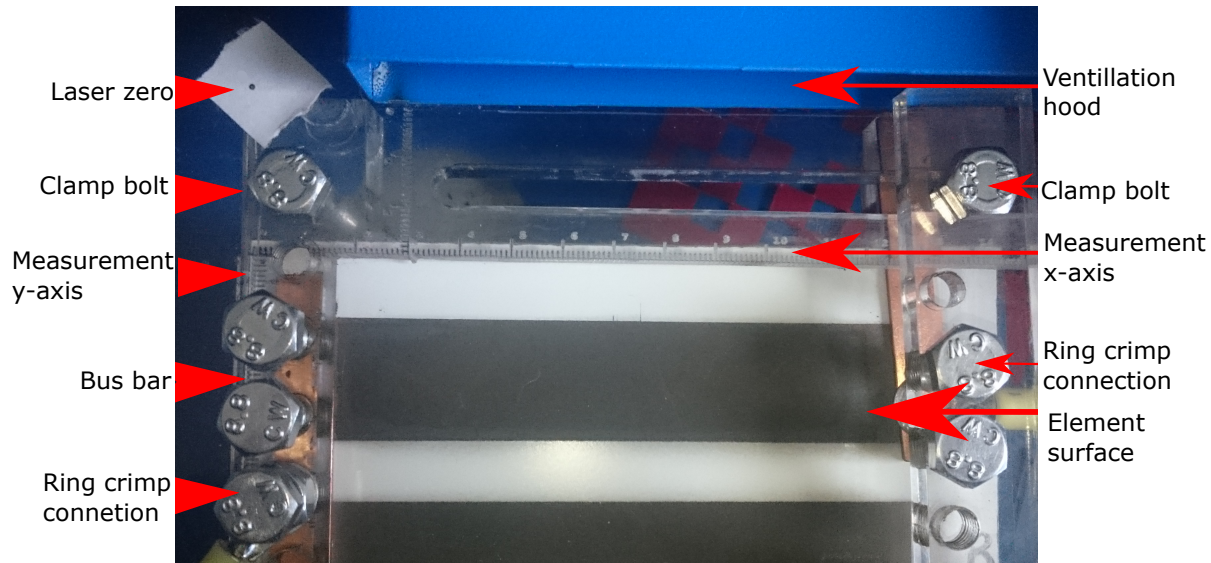


Figure 5.16: A labelled diagram of the clamp system in operation.

To manufacture the internal axis, holes and cut out sections were produced by the laser within the machine. The axis was etched onto the worktop by the laser; This axis correlates with the value of the positions of the laser within the laser software so if the laser were ordered to move to the right by 10mm and down 10mm the laser would move to this location on the worktop. This provides a way to compare locations on the worktop with locations in the software from a set zero position.

The upper clamp bridge has M8 tapped holes through them at 1cm intervals. The element is held by M8 bolts screwed into these holes which clamp the element onto two clamp bridges under the element. A M8 screw was chosen as a compromise between maximising the number of threads, depth of thread and the surface area of the bolt head. On top of the element between the bolt and the element connection is a copper bus bar which reduces the contact resistance of the element and increases the surface area of the connection between the bolt and the elements silver contact strip.

Two ring crimps of an internal diameter to fit around a M8 bolt are added to the wires from the power source and are secured with M8 nuts to the clamp to avoid removal when the device is under operation. The wires are fed under the acrylic worktop so that the laser does not fray or damage them.

5.8.5 Mirror Alignment

To create as small a spot size as possible for the laser it was vital that the laser was well aligned. In order to do so, an alignment procedure was created which is outlined further in appendix item A2. This procedure is regularly used to check the laser alignment and most crucially was used to correct for changes to the alignment after transporting the laser. This took place when the laser first arrived, a variety of improvements to the positioning had to take place such as raising the second mirror slightly so that the laser had a better alignment through the lens. After the laser was brought into alignment and not transported anymore, only minor changes need to be made to correct the alignment. These are focused on the laser head and second mirror.

5.9 System Validation and Calibration

5.9.1 Depth of Pulsed Spots on the Material

The processing strategy that was chosen is to place a series of pulsed dots onto the work piece with dots at a higher density in the coldest areas. This is to maintain the flow of current through the film whilst increasing the local resistance of the ablated areas. The lowest laser power where ablation takes place and the laser output is stable is at 20% of the maximum laser current. This equates to 10W of average optical delivered after accounting for the laser power curve, laser reflection and mirror efficiency.

The shortest stable pulse time of the laser is 30 μs , this is used because the lower the time period of laser ablation, the smaller the heat affected zone and melt depth. Using these values this equates to a pulse energy of 300 μJ and a fluence of 2.26J cm^{-2} for each pulse of the laser on the material. Some of the laser pulses overlap thus a greater fluence is applied to the area in the areas that overlap, this is proportional to the overlap of the pulses. At half overlap the radius of the circumference of each circle overlap with the centre of each circle. At a quarter overlap the radius of the circumference overlaps with half the radius of the other circle. This means that in the overlapped areas there is a higher fluence. Assuming a uniform fluence within the pulse beam these areas receive double the fluence than the other areas.

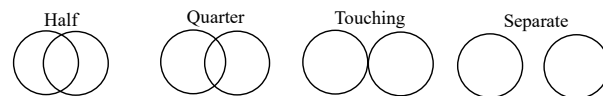


Figure 5.17: Pulse overlap definitions are shown in the figure to illustrate the difference between the various overlap definitions.

Table 5.2: Average depth of pulses ablated onto the film with various overlaps at 2.26 J cm^{-2} , $30 \mu\text{s}$ pulse, 0.13mm spot size.

Overlap	Half	Quarter	Touching	Separate
Average Depth of hole (μm)	11.6	9.3	7.1	6.7

The overlap of each pulse changes depending on the recorded temperature of each area of the element emitted by the joule heating. The highest level of overlap is at the coldest areas on the element each pulse overlaps with half of the last pulse. The amount of overlap decreases until at half the scale there is zero overlap of the pulses then the displacement between pulses increases as the temperature recorded in that region increases until a threshold temperature is reached. The depth of each spot of the laser has been found through optical profilometry when the laser pulse is overlapped and when the laser pulses are not overlapped at the settings described above.

The depth of four cases of overlap have been tabulated in table 5.2. The maximum depth of each hole is measured for each pulse including when there is an overlap of the pulses. This shows that at higher overlap between pulses the depth of the hole on average is slightly larger, the hypothesis of this is that the heat from the previous pulse is still heating the area leading to more energy available for ablation and in addition the overlap of the pulses means less material is required to ablate the same depth. As expected all the depths of holes are roughly similar in size.

This is expected since a similar energy density is applied to each pulse. The pulse sizes of no overlap and where the laser pulses are separate are close in depth and within the error of measurement. The pulse depth of all these scenarios is less than the film depth and since multiple ablation cycles take place on the element if multiple pulses are directed to the same area the laser is not likely to penetrate through to the substrate.

5.9.2 Greyscale Pulsed Output Implementation

When working with a continuous laser treatment, the whole region is set to one 'colour' which sets one percentage of power and speed of laser for the whole coloured area. The laser follows a subsequent raster pattern across the surface in layers until it has completed the operation. In this mode the laser is either on or off. The processing methods that use this mode are the 20% and 50 % threshold methods that only ablate areas lower than their respective thresholds.

For more advanced processing methods, the pulsing of the laser is undertaken by altering the duty cycle of the laser. The software is able to interpret images to be pulsed by the use of greyscale images with a dither process. A dither process is where the intensity of colour or treatment in an area is increased by increasing the duty cycle within that area.

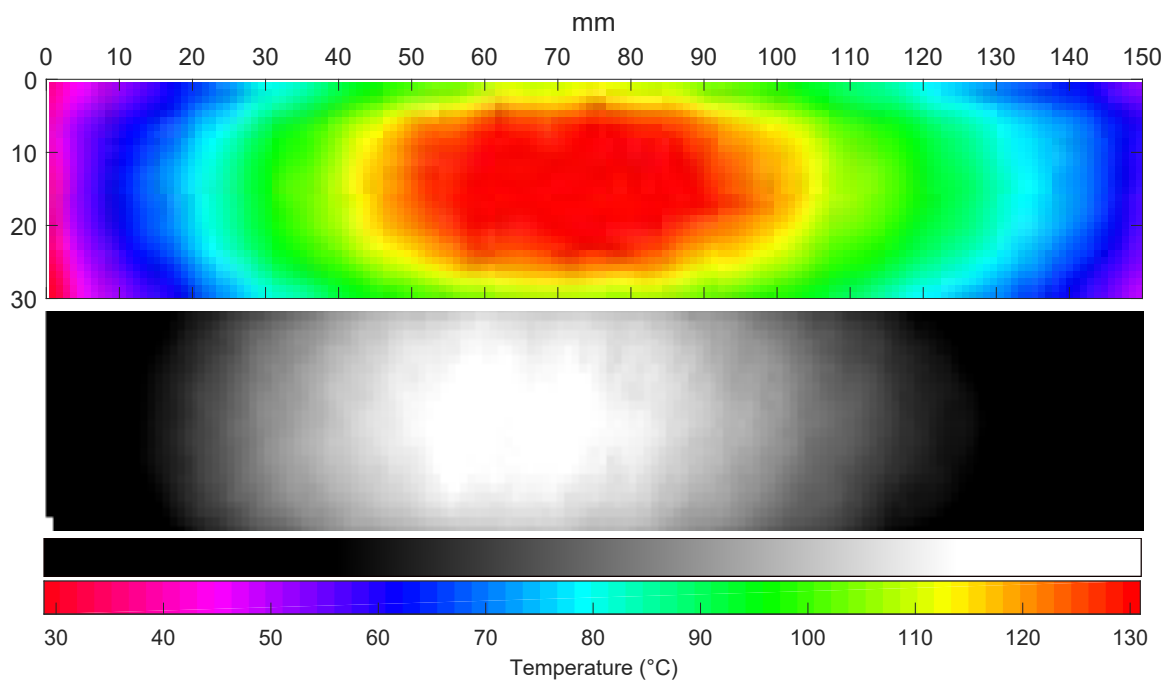


Figure 5.18: A thermal image of the element is converted to a greyscale image with the greyscale adjacent to the temperature graph.

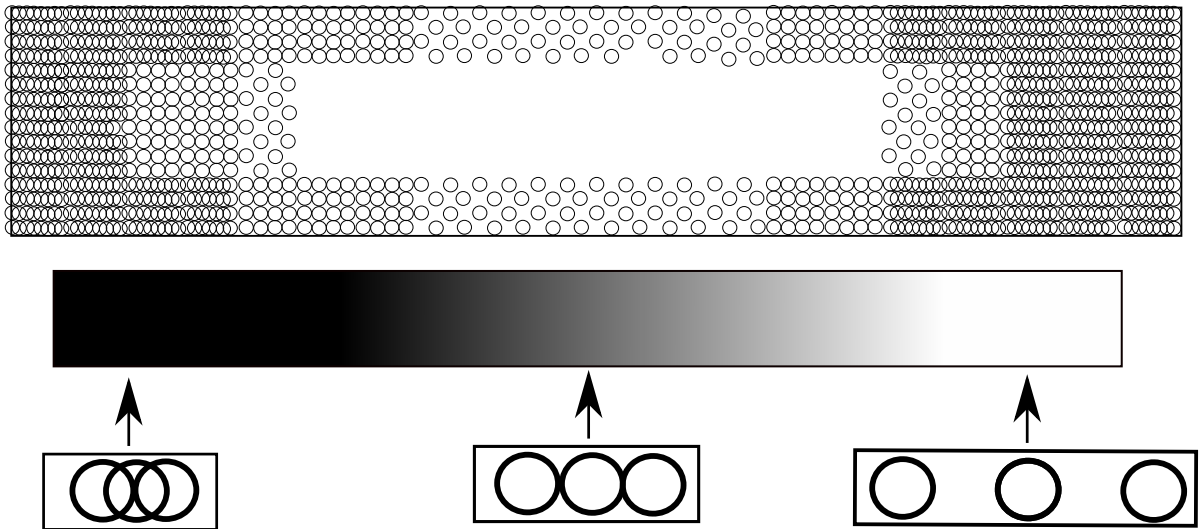


Figure 5.19: A diagram of a greyscale transferred into a pulse map with the corresponding translation between the greyscale and the gap between pulses illustrated.

An example in the printing industry is where lots of dots are used to make an area look black, a few dots are used to make an area look grey and white areas have a low concentration of dots. The same process is used to generate a greyscale image from a treatment process where each dot applied is identical.

This process is implemented in this research project by using a greyscale image having an intensity from 100% (black) to 0% (white). The laser at 100 % pulses every half of its beam radius so that pulses overlap, as a lighter shade is output the distance between pulses increases until the point the distance between pulses is larger than the spot size, which is when the laser stops pulsing.



Figure 5.20: The output of the conversion of the greyscale to a pulse map which is lasered onto an acrylic sheet.

These thresholds are set from the greater range of duty cycles where greater ablation is possible through more pulses on each area. This was decided, through the initial experimental tests, to be undesirable as the chance of burnout is higher and the effect on the device resistance is too high. Within figure 5.19 a sample image of an element is shown, below is a reference greyscale displaying the pulse/duty cycle overlap. This illustrates how the greyscale algorithm has selected regions of lower temperature to receive a greater amount of treatment and areas at a higher temperature to receive a lower amount of treatment. This allows a more relevant treatment to be delivered to the element in comparison to the continuous modes. Within the sections outlining the results and the processing methods, there is a variety of alterations made so that the amount of treatment delivered is more appropriate and specific to the elements at hand.

At the maximum amount of treatment, there is an overlap of the pulses. This means each area receives a greater fluence than each non-overlapping area. Hence, when the laser is overlapping (from 100% to 50%) the ablation rate is higher than when not overlapping.

The laser head follows a raster from one end to the other; whilst following the lines along the raster, the next line is ablated with a set overlap which is set to the laser spot diameter so that within each line of ablation the laser does not interact with the previous laser line of ablation. The reason for this setting is so the laser does not ablate areas after they have cooled down and re-solidified. If the laser was to interact with a hole, the laser beam can be reflected and focus in the hole, and therefore increase the amount of ablation there. This would worsen the size of the hole in a nonlinear fashion that is not accounted for, which can increase the chance of a burnout as the hole can now start to ablate through to the substrate.

5.9.3 Time to Reach Steady State Investigation

Reductions to the overall processing time of each treatment step was achieved through altering the power sent to the element over time. The processing time was reduced by reducing the time taken for the system to reach a steady state or equilibrium so that the thermal data can be taken for the treatment procedure to begin. To do this the element is visualised with a thermal camera, the thermal camera sends this information to the computer which analyses the data, from this data the standard deviation of the element is calculated. When the standard deviation of the element surface temperature is constant then the element has reached a steady state.

To investigate and reduce the time required to reach a steady state various heating techniques were tested then implemented. This data is shown in a graph in figure 5.21. The first trial had the element heated by a continuous power input to find the baseline time for the element to reach a steady state. In the plot the baseline time takes 300 seconds to reach a steady state. Any reduction in this will reduce the total processing of an element by a factor of the number of processing cycles.

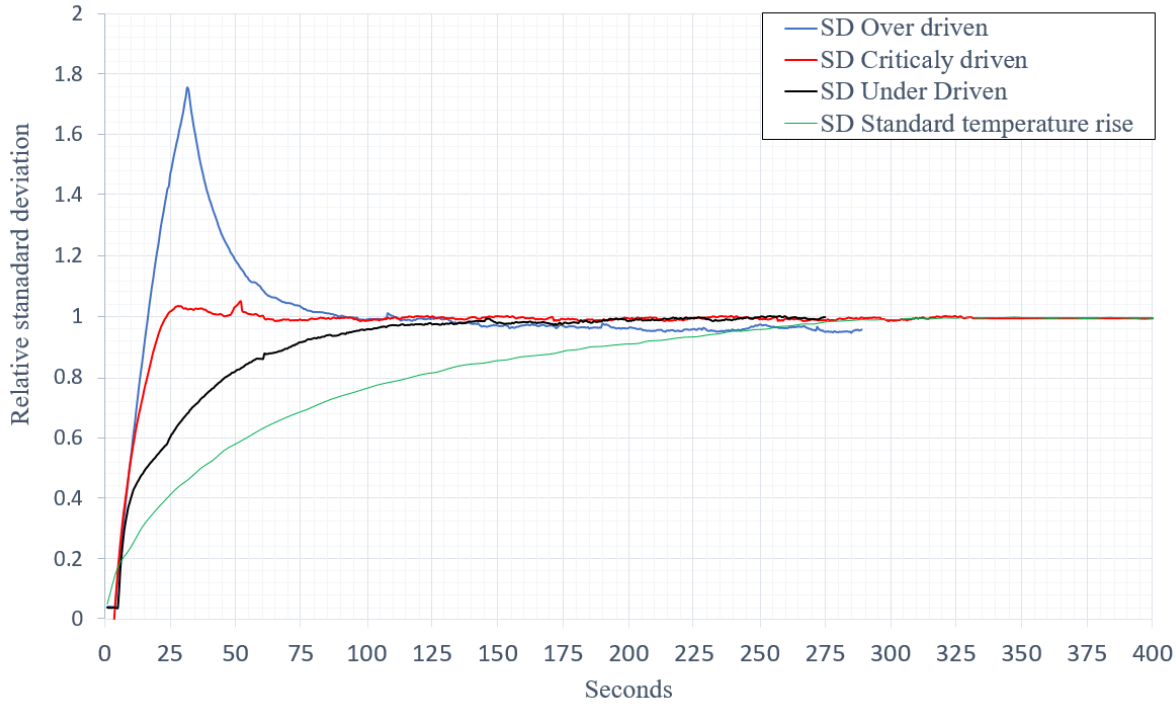


Figure 5.21: The standard deviation of the temperature profile over time for an element heated through various heating techniques.

To reduce this process a scheme of pulsing the power initially at a higher power and when the mean temperature of the element as recorded by the thermal camera reaches the desired temperature the power input is lowered to the appropriate level to maintain that temperature at a steady state, three examples of this are shown in the plot, the under driven line were the initial power input was too low to appreciably decrease the processing time.

The over driven line which has the power input to high or on for too long leading to an over driving of the system. Finally there is the critically driven element that reaches a steady state the quickest. This reduces the time to take data from 300 seconds to 50 seconds, a factor of 6 times which is saved in each processing time adding up to over 30 minutes per element saved.

5.10 Resistance Experiments

The temperature dependence of the resistance of the material is investigated. This is shown in figure (5.22). The graph of the normalised resistance of the element as the normalised temperature increases shows a linear relationship. By plotting $\frac{R}{R_0} = \alpha\left(\frac{T}{T_0}\right) + c$ as $y = mx + c$ the linear Resistor temperature dependence coefficient is found.

Through this method a value for $\alpha = 0.0057$ was determined. The value found for Nickel samples is 0.005 [11]. This provided evidence that the primary carrier of the current through the element is Nickel, this is because the resistance increase temperature coefficient for Nickel Oxide is much higher at 0.5 [39].

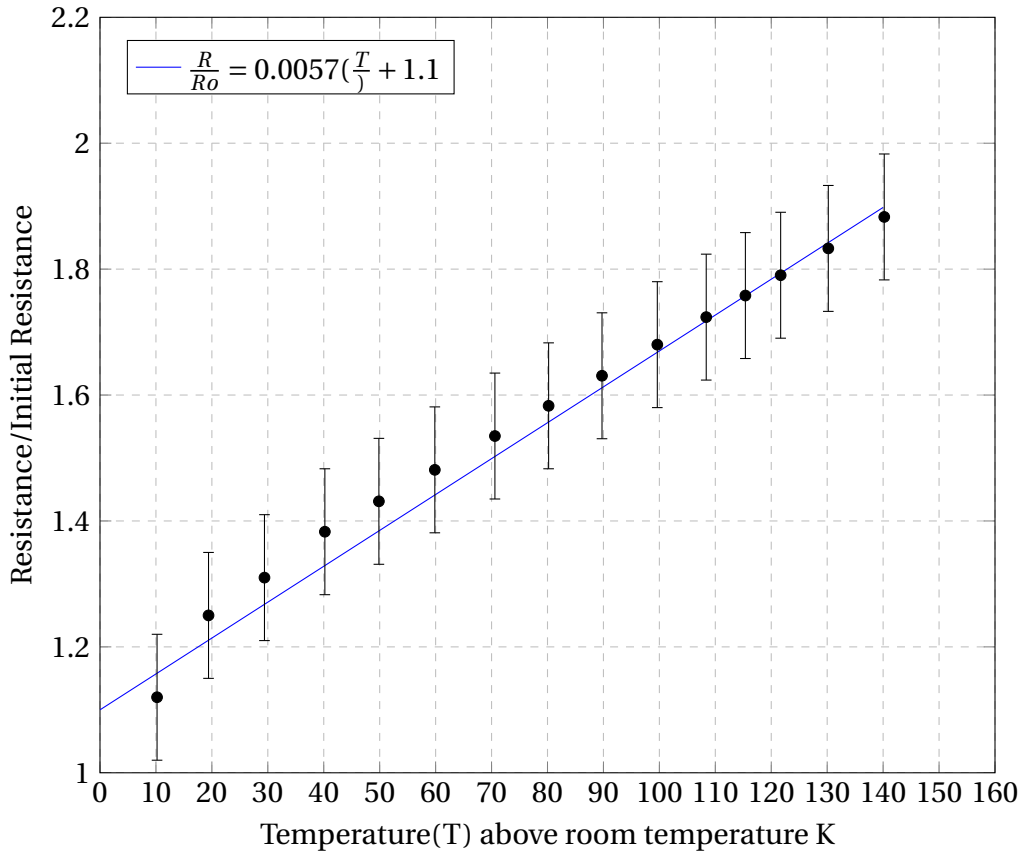


Figure 5.22: Resistance as a function of temperature normalised by the initial resistance. Error bars result from the uncertainty due to measuring high resistances leading to small voltages with the voltmeter at the range of

5.11 Maintenance of power output as element resistance changes

As the element is ablated the resistance of the element increases, this is through the pathways listed in the literature review. The power output of the element is correlated with the (R) resistance of the element and the (V) voltage applied to the element. This is described by Ohms law in equation 3.3. This means that the element reaches a different steady state temperature at different element resistances with the same voltage applied as the current through the element changes.

As the goal of the project is to change the resistance of the element with the treatment, the resistance cannot be controlled and the voltage input to the element must be varied so the elements power output is held constant throughout the tests. This is important so that the data for the various processing methods can be compared against one another as the element temperature changes as a result of the resistance change.

To achieve this, resistance tests are carried out after each trial, these are outlined in the methods section under the heading of resistance measurement. For each of the trials the resistance of the element is found, this is used with Ohm's law from equation (3.3) and the equation for electrical power in equation (2.3) to control the power output as the current is decreased so that the power output is held constant, the expression for this is shown in equation 5.10. The *i* subscript indicates the initial applied variable and the subscript *F* indicates the variable associated with the element after treatment. I_F is the current applied after the treatment process in order to account for the resistance change of the element.

$$I_F = \sqrt{\frac{I_i V_i}{R_F}} \quad (5.10)$$

5.12 Laser-Treatment Processing methods

There are various methods trialed within the project to generate a processing method for the treatment of the elements. This section outlines how the processing method works and show the resultant temperature profile measurements. As discussed in the implementation of system design section, the camera takes the thermal image data, the processing method analyses this data and then outputs an image for the laser path to follow.

All the methods work along this basis with the final method, the Greyscale hybrid with memory (GM) method, including an additional step that uses the treatment from previous trials to affect the treatment it delivers in the next cycle. Table 5.3 summarises the processing methods used to alter the element.

5.12.1 Abrasion baseline

The abrasion baseline is used so that the results of the laser processing methods can be understood in comparison to a baseline. This allowed for the comparisons of the methods against what is already achieved by the company to determine the advantages and disadvantages of the laser processing processing methods. The abrasion method works by a silicon carbide sandpaper being applied to the areas of the element with the lowest heat production by hand.

What is interesting to not is that within the laser method there is a definite change in the oxidation and phase of the material but in the abrasion method the change in the elements thermal profile is solely due to the thickness reduction of the element. This provides a useful comparison.

Table 5.3: Summary of the differences between the processing methods.

Ablation Method	Summary
Abrasion Baseline	The abrasion method is carried out by the analysis of the thermal profile of the element and abrading with an abrasive medium the coolest regions of the element temperature profile.
20% Threshold (20%)	All regions at temperatures lower than the 20th percentile of the distribution of temperature were ablated at the optimised output of a pulsed beam in a raster pattern.
50% Threshold (50%)	All regions at temperatures lower than the 50th percentile of the distribution of temperature are ablated with a pulsed beam in a raster pattern.
Greyscale (GS)	The element is ablated in a raster pattern with the coldest areas receiving more treatment than hotter areas through altering the duty cycle of the pulsed beam, areas at the highest temperature regions receive 0% of the power output with a linear scale between.
Greyscale-Threshold (GT)	The Greyscale algorithm is used to find the levels of treatment in the areas between a threshold value (set at the hottest 20th percentile) and the lowest temperature.
GT + Memory (GM)	The GT method was used but previous treatments (n-1) reduced the intensity of subsequent treatments (n) by upto 10% of the output of the previous treatment.

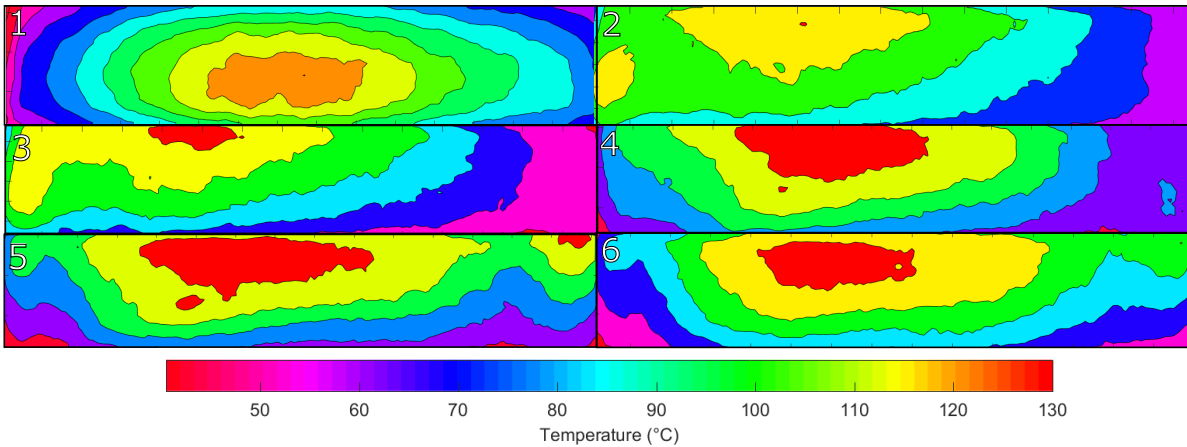


Figure 5.23: The Abrasion method is used to ablate element, contour plots of the surface temperature profile measurements shown after each cycle of ablation. The initial element is seen in the top left plot, reading from left to right in rows the element is ablated in each step, these are marked by numbers in the plots.

The Abrasion method is inherently imprecise because it relies upon the thermal image analysed by an operator and then the element is given an unknown amount of treatment in those areas to change its heating profile. In addition, since the element must be cooled before the process can begin there is an appreciable amount of time taken for this step.

The surface thermal measurements have been analysed with a contour plot of their values. The contours are drawn every 10°C with an attached colour bar scale. The first image shows the element before abrasion has taken place. The characteristic hot spot in the centre of the element is shown with the steep thermal gradient along the outside.

It shows an initial thermal variation of 50% between the hottest and coldest areas. The first step in the processing drastically changes the distribution of temperatures and along one edge the element has a good degree of uniformity, although along the other edge there is a wider concentration gradient than before.

This shows how the operator has a large effect on the process and how an operator can introduce unevenness of the profile. Within further processing the thermal profile improves until at the 6th stage the thermal profile is at its optimal within these cycling steps.

The second problem with the abrasion method is that the initial abrasion is very easily carried out, then as the element receives more abrasion less material can be removed with the same amount of work on the element from the abrasion. This means that it is hard to reverse the changes of the abrasion method with further abrasion as seen when comparing the over abrasion in the 1st processing cycle to the subsequent ones.

5.12.2 20% Threshold (20%) Temperature Profile Measurements

All the regions in the lowest 20th percentile are marked in one shade of grey for ablation and the dither mode is used, so that in the regions to be ablated the laser pulses so that each pulse begins where the last pulse ended. This process repeats until the desired uniformity is reached or the peak element surface improvement is reached.

The laser speed is set as high as possible at 300mm/s and the laser power was set at 25%. Since the whole area selected for treatment is treated with the same amount of treatment the hypothesis for this processing method is that these regions will become the hottest regions on the element which will equate with the thermal load on the element. As the element is very inhomogenous the processing has to be repeated in multiple cycles so that the best result can be achieved, this is due to being unable to predict how the element will change when ablated.

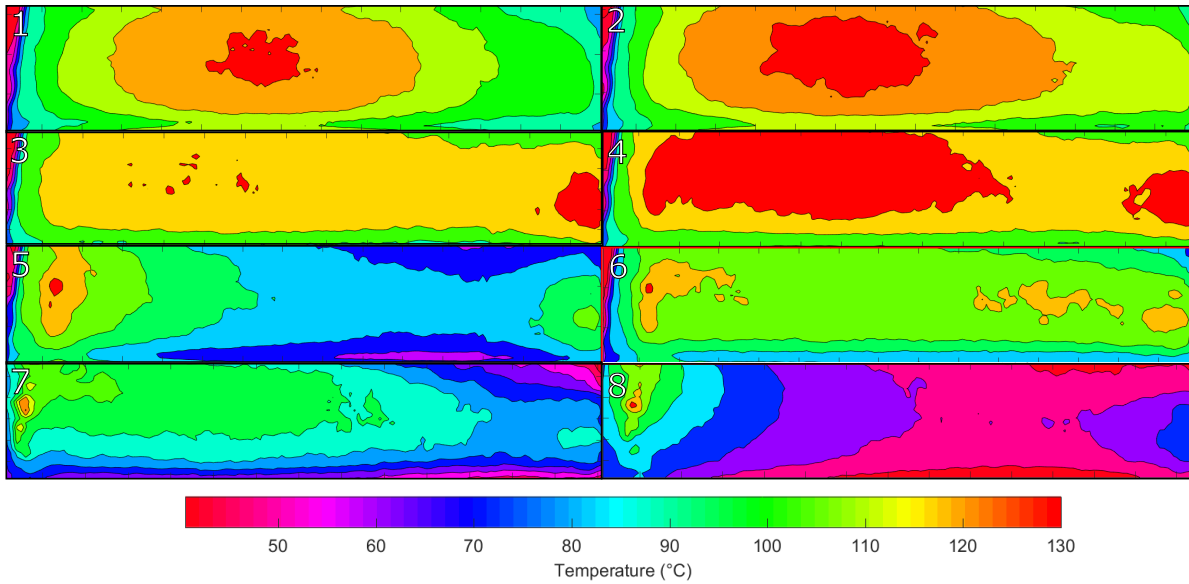


Figure 5.24: 20% method used to treat element, contour plots of the surface temperature profile measurements shown after each cycle of ablation. The initial element is seen in the top left plot, reading from left to right in rows the element is ablated in each step, these are marked by numbers in the plots.

The temperature profile measurements for the 20% method are shown in figure 5.24. Going from ablation cycle 1-3 improvement is seen, 4 has a slight improvement, 6 improves upon 4 but is worse than 3, and 7 is worse than all. Based off these results it appears that this method works well at getting a mild improvement but suffers from not ablating areas that are hot but not near the peak output, this can be improved by either increasing the percentile threshold so more of the element will be affected or by hybridising this technique with the other techniques.

The 20% method shows that by targeting the laser at the coldest areas of the temperature surface the element can become more uniform and the distribution of heat output altered to these regions. Its weakness comes from the fact since it only effects coldest areas of the element it cannot have an effect on regions in the centre of the element that are low heat output but still warm due to their position in the centre of the film and thus require treatment to stretch the heat profile further.

This weakness is compounded when the geometry of the elements are considered. Thus the edges will have a higher heat loss and the central regions have a lower heat loss so will not be as cool as the edges. This means they will not be treated by this algorithm. This leads to the image seen in ablation 3 where one half of the element is cooler than the median, this is reduces in ablation 4 because the ends are being treated and thus getting hotter to warm the central region. To resolve this the threshold for ablation is increased to 50% in the next trial so more areas are ablated and in the modulation of the treatment amount with the greyscale methods.

5.12.3 50% Threshold (50%) Method

All the regions in the lowest 50th percentile are marked in one shade of grey for ablation and the dither mode is used, so that in the regions to be ablated the laser pulses so that each pulse begins where the last pulse ended. This process repeats until the desired uniformity is reached or the peak element surface improvement is reached. The hypothesis behind this processing method is that if all the areas below the median temperature are treated in each cycle the standard deviation and distribution of temperature should become more uniform.

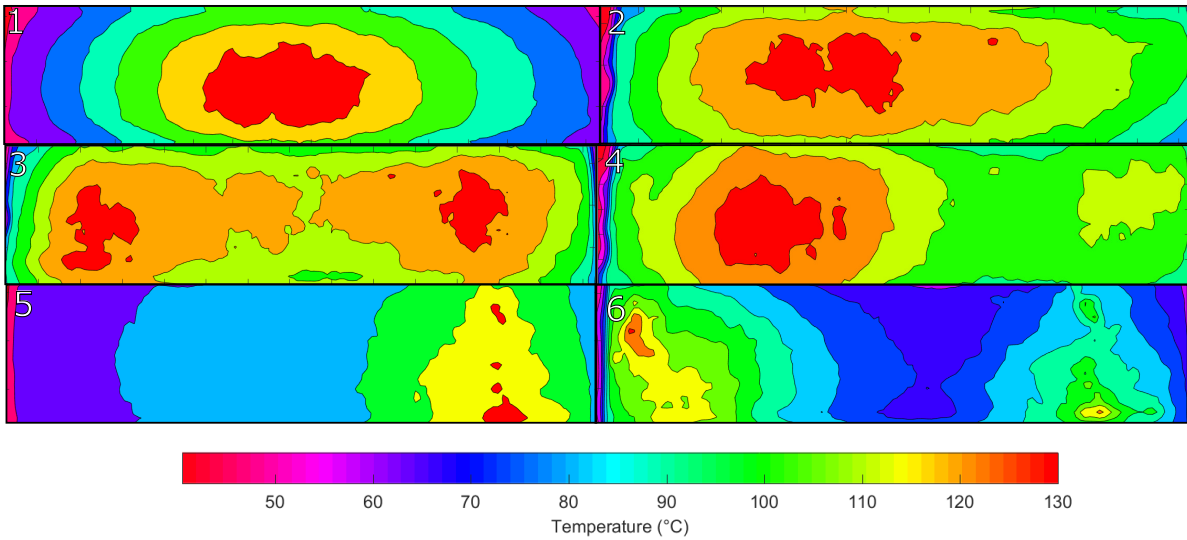


Figure 5.25: 50% method used to ablate element, contour plots of the surface temperature profile measurements shown after each cycle of ablation. The initial element is seen in the top left plot, reading from left to right in rows the element is ablated in each step, these are marked by numbers in the plots.

The data showing the temperature profile of the element after each processing cycle using the 50% method is shown in figure 5.25. Comparing the steady state images of the profiles it is observed that the treatment of these large areas with this power output does not converge the temperature profile to an uniform desired temperature profile.

The most even profile is after one processing cycle. In the 3rd image the heat distribution of the element is centred on the ends of the element with a colder central region which then as the laser interacts again with this area the heat distribution becomes skewed.

Also due to the over treatment in each system the chance of burnout is high, this is seen in images 5 and 6. The images show that the profile can be affected enough so that the temperature profile changes dramatically, this is positive as it shows a different temperature profile can be produced. This lead to the assumption that if an algorithm is developed that is more appropriate to the system then a more even heat profile can be produced. This lead to the development of the Greyscale algorithm.

5.12.4 Greyscale (GS) Method

The greyscale algorithm maps the intensity of the thermal image as an input to the output of the laser in a continuous linear distribution. The coldest regions map to 100% of the desired laser output and the hottest region to 0% of the desired laser output.

Through earlier calibrations the desired minimum output of the laser is set at 25% of the maximum greyscale colour and the desired maximum output of the laser is set at 65% of the maximum greyscale colour. These values were decided from looking at the output of a 0% to 100% greyscale then selecting the minimum and maximum values from where the laser starts pulsing (25%) and where the output becomes continuous (65%). For values between this maximum and minimum the distance between the laser pulses increases. This process repeats until the desired uniformity is reached or the peak element surface improvement is reached.

The data showing the temperature profile of the element after each processing cycle is shown in figure 5.26. The temperature profile of the element improves in each processing cycle until the 5th cycle. Within the 5th and 6th processing cycles areas of high resistance have been created that are called burnouts, these regions provide an irreversible inhomogeneity to the temperature profile of the element. The causes of these are investigated in the burnout section.

The hypothesis is that the film has a high degree of inhomogeneity and when the laser interacts with unstable areas it can be ablated through the enamel layer and provide a path through the substrate providing a short circuit, when this happens in two regions the current flows through the substrate and back through the film, if the current flow is high enough the film temperature increases rapidly and the film is irreversibly damaged.

The GS method is susceptible to this because the amount of treatment delivered to the element is high. This is because the laser ablates the whole element and does not stop within the thresholds so as the element temperature is optimised the laser is treating the central areas too, all be it with less treatment. This means the laser ablates the element to a high degree and thus the chance of burnout increases.

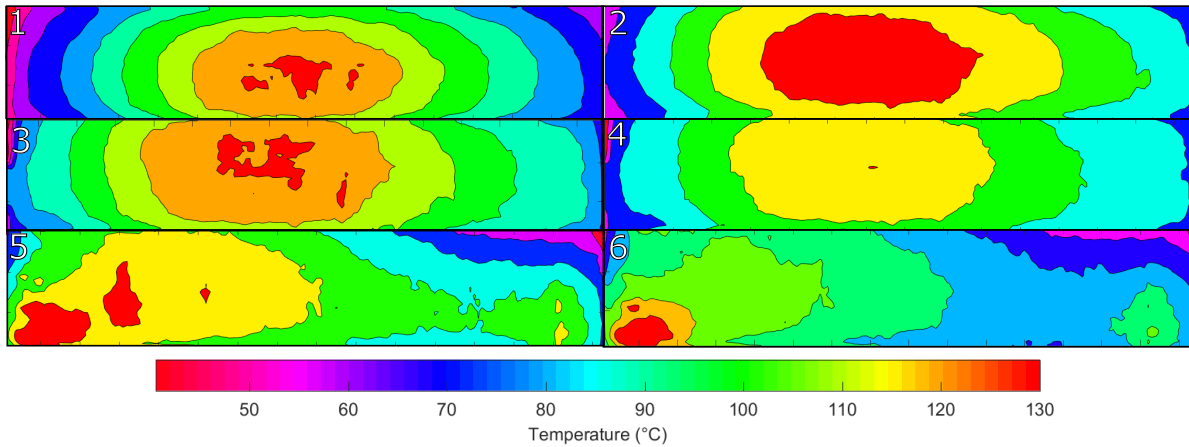


Figure 5.26: Contour plots of the surface temperature profile measurements after each cycle of ablation using the Greyscale method. The initial element is seen in the top left plot, reading from left to right in rows the element is ablated in each step, these are marked by numbers in the plots.

Through observing the most improved ablation (ablation 4) the ends of the element are still at a temperature lower than the average, these areas are receiving the largest amount of treatment but are still cooler. The hypothesis for this is that all the areas of the element are receiving treatment so the cold ends are not receiving enough treatment in relation to the whole element. This indicates an error in the calibration of the greyscale to the areas for treatment.

In addition, the lateral bias of the element is not corrected, I believe this is because of the problem stated above, the ends/ edges are not receiving enough treatment in relation to the whole element. The problem of burnouts is still present in the Greyscale method of which it was developed as a way to reduce, this is due to the problem of over-treatment of central areas.

To rectify this problem a region in the centre of the element (in the hot spot) will be left un-ablated. This means the ends will have a greater effect of treatment as they will receive more treatment in relation to the whole element. This lead to the development of the Greyscale-Threshold method.

5.12.5 Greyscale-Threshold(GT) Temperature Profile Measurements

This algorithm uses a greyscale to alter the duty cycle to give greater treatment in areas of the lowest temperature. The region this operates between is the minimum values to the median value so only areas lower than the median are ablated. The hypothesis is that this is an improvement to both the median and greyscale methods above.

The exact value of the threshold can be altered to percentiles greater or lower than the median. The hypothesis within this test is that the introduction of a upper threshold will stop the laser from over treating the central areas an concentrate on the outer areas more leading to a lower amount of overall treatment and a overall lower chance of a burnout.

These tests were carried out three times to determine how reliable the processing of the elements is. The first trial the laser power was set at 25% this was so that comparisons of the effect of the laser power with different processing methods. Within the second and third trials the power is set at 20%.

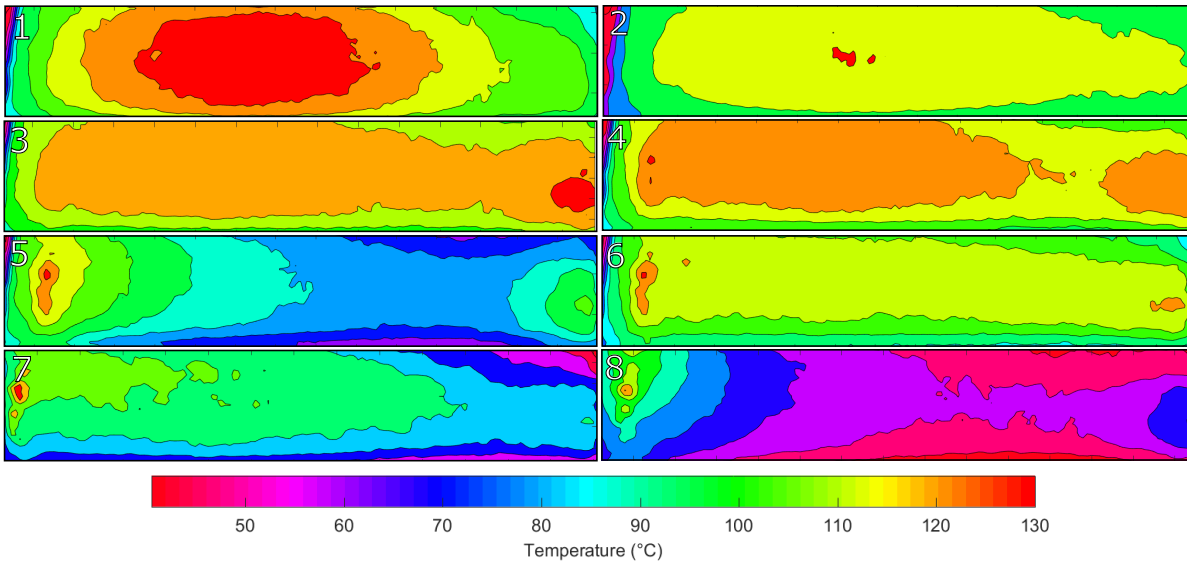


Figure 5.27: The first repetition of the Greyscale - threshold hybrid (GH) method is shown in the contour plots of the surface temperature profile measurements shown after each cycle of ablation. The initial element is seen in the top left plot, reading from left to right in rows the element is ablated in each step, these are marked by numbers in the plots.

The surface temperature profile contour plots are shown in figure 5.27,5.28 and 5.29. Within the first trial the temperature profile of the element increases, after 6 cycles the temperature profile is at its optimal. There is a 10% temperature variation across the element at this stage. What is also interesting to note is that the element temperature becomes higher at the edges in the 5th cycle. Then when processed again the element is much more uniform. This is an example of how the method incorporated negative feedback and has the ability to process the element to both make the edges a higher temperature and the centre a higher temperature.

The laser power of this test is 25%, the element reaches a burnout on its 7th and 8th trial, this shows that this laser power is too high for this processing level if more than 6 cycles are to be achieved. Although if the number of cycles is being minimised the use of a higher power shows that the element will be treated in less cycles with the higher chance of a burnout.

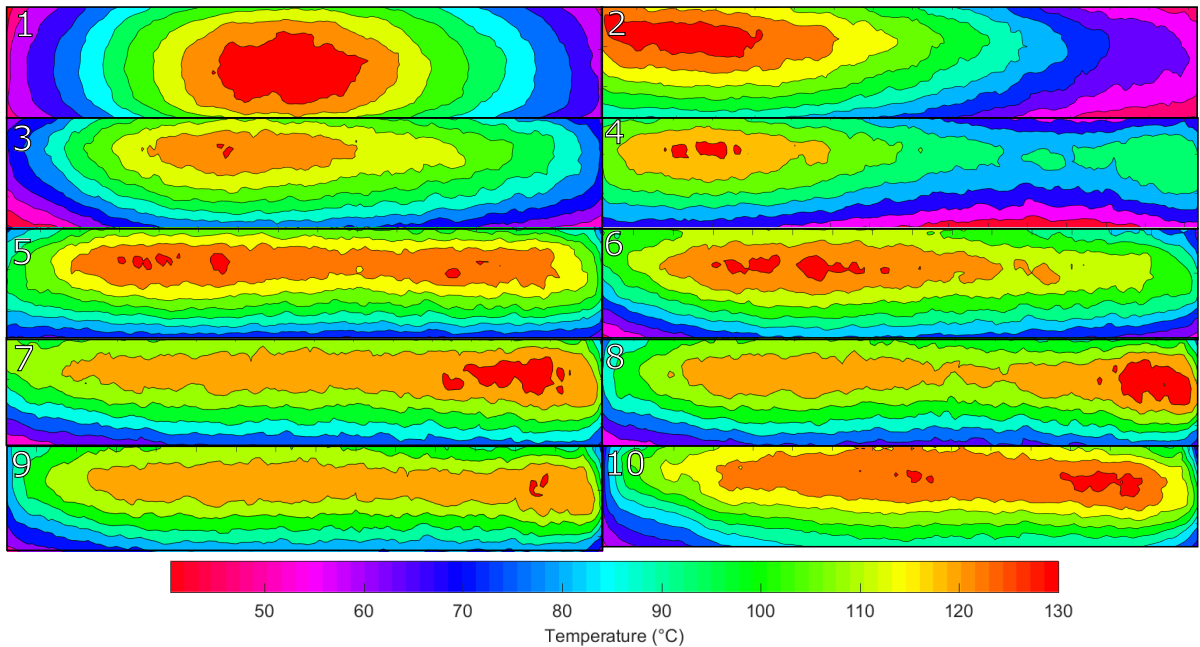


Figure 5.28: The Second repetition of the Greyscale - threshold hybrid (GH) method is shown in the contour plots of the surface temperature profile measurements shown after each cycle of ablation. The initial element is seen in the top left plot, reading from left to right in rows the element is ablated in each step, these are marked by numbers in the plots.

Within the second trial the element has a higher initial variation of temperature across its profile. This is shown by the hot spot in the centre and the cooler regions on the edges. The method takes 9 cycles to reach an optimal profile. This trial was done on 20%, at this power the element is being treated less than in the first trial.

More cycles are thus needed to reach the same level of treatment but the amount of treatment is more specific, when comparing the temperature profiles of the trials the first trial appears to be more uniform than the second trial, it is worth while to consider that the element did start off more inhomogenous though.

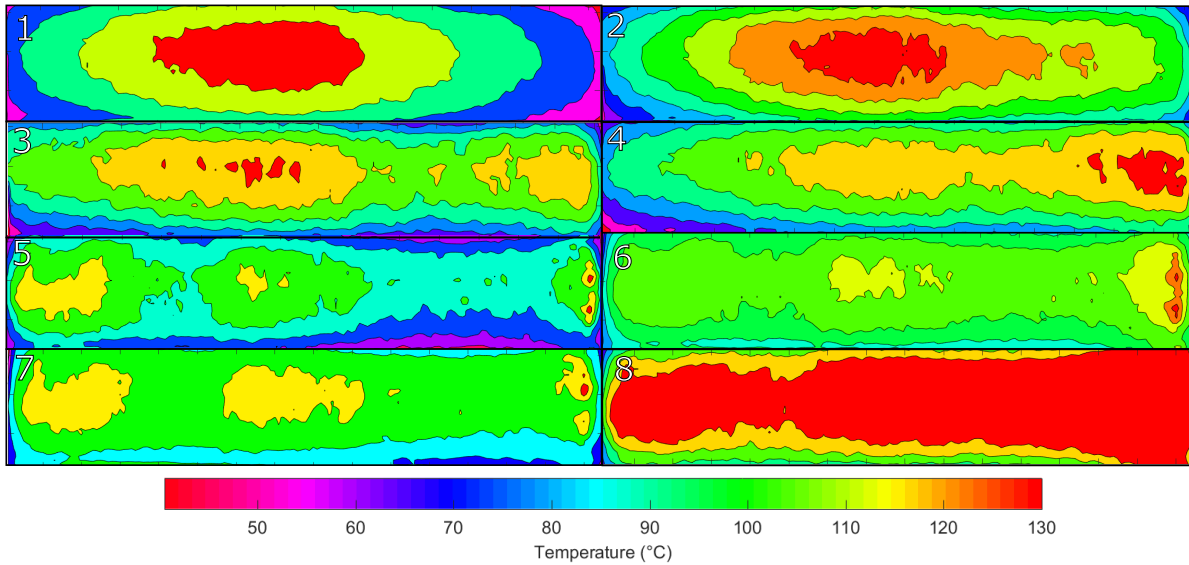


Figure 5.29: The third repetition of the Greyscale - threshold hybrid (GH) method is shown in the contour plots of the surface temperature profile measurements shown after each cycle of ablation. The initial element is seen in the top left plot, reading from left to right in rows the element is ablated in each step, these are marked by numbers in the plots.

In the third trial the optimum profile is reached first in the 6th cycle. This shows a similar pattern to the other trials, this also shows how the method can optimise a profile with the centre of the element ablated. One area to focus upon is the hot spots on the edges of the profiles. These are areas that previously have lead to burnouts. This shows that the processing method requires some alteration to reduce the chance of a burnout. This is the motivation of the greyscale memory processing method.

5.12.6 Greyscale Threshold + Memory (GM)

The Greyscale Threshold + Memory method adds an additional step in the processing of each element cycle. In calculating the level of treatment required from the greyscale threshold algorithm the method compares the image it has output with the last cycle of ablation, in the areas that the laser ablated last time the element reduces by a multiple of 20% in the greyscale value so the overlap of the pulses is reduced by 20%.

This means if the laser ablated a section at 100% previously it will now ablate it at 80% of the treatment amount designated by the greyscale threshold algorithm. If this region now needs a 50% greyscale output the method after using the memory step will reduce this to $80\% \times 50\% = 40\%$. This works in a continuum until the element is ablating at 80%.

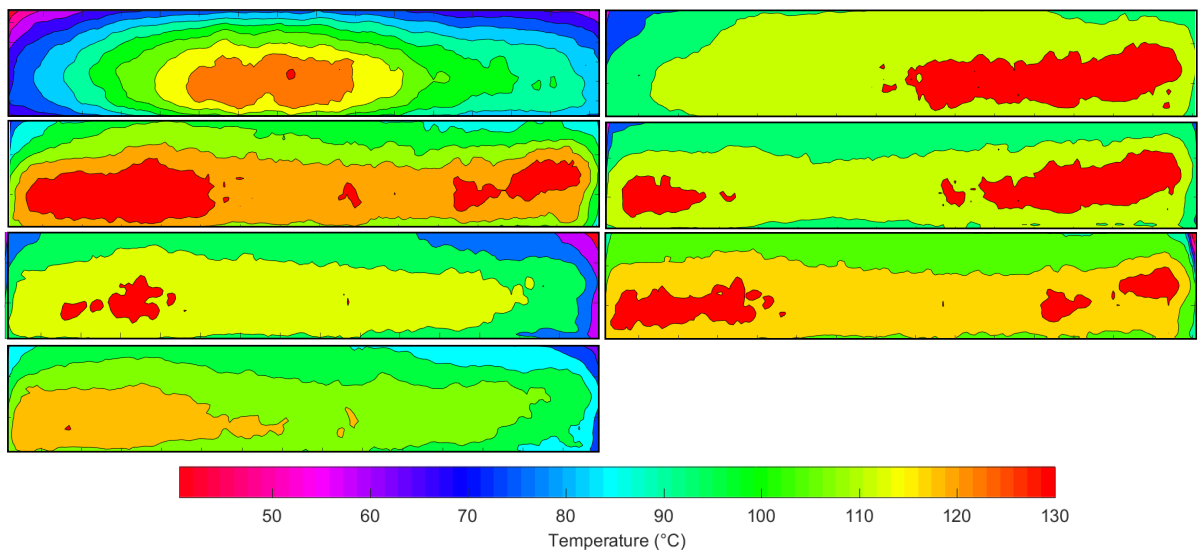


Figure 5.30: The Greyscale - threshold hybrid method plus memory processing is used to treat the element. The result is visualised in contour plots of the surface temperature profile measurements shown after each cycle of ablation. The initial element is seen in the top left plot, reading from left to right in rows the element is ablated in each step, these are marked by numbers in the plots.

In subsequent ablations (when the # of ablations in one area >1) the areas treated previously are either left untreated or their treatment is scaled so that chance of burnouts are reduced. The temperature profile contour plot for the GM method is shown in figure 5.30.

The optimised profile is reached in the 6th cycle. The variation of temperature is again similar to that of the GT method. The key difference is the reduction of the hot spots on the edge of the element, this means that there is a lower chance of burnout on the edges of the element as less high temperature regions are being created. The profile is as uniform as in the greyscale threshold results. This indicates the method does not compromise on the production of a uniform surface for the reduction in burnout chance

5.13 Processing Method Metrics

The metrics of the processing methods are given in table 5.4. The table shows that all methods improve the profile of the raw element. The method that produced the lowest standard deviation improvement was the 50% method which is due to creation of regions of high temperature and low temperature due to the over-processing. This as explained when looking at the contour plots is attributed to the method effecting too large an area of the element with the same treatment amount.

The method that improves the standard deviation the most was the GT and GM methods. These methods thus apply most relevant treatment of the element to improve the standard deviation of the element. This is due to focusing on improving the heat production of the lowest temperature regions of the temperature profile whilst applying a targeted and specific treatment value to each position on the element.

Table 5.4: The performance metrics of the various processing methods used to compare the total improvement of the temperature profile from the initial element to the optimised profile.

Metric	20% Threshold	50% Threshold	Greyscale	Greyscale Threshold	GT with Memory
Abbreviation	20%	50%	GS	GT	GM
% Standard deviation improvement	62.1	-25.1	57.4	65.8	71.2
% Standard deviation improvement/cycle	15.5	-6.3	7.1	11.1	11.9
Optimised profile kurtosis	2.71	2.08	3.57	3.37	2.71
Time / cycle (mins)	1.5	2.0	3.0	3.0	3.0
Average amount of cycles	4	8	4	6	6

The kurtosis of the optimised profile shows how much the profile has become peakier or an even profile. values closer to 3 indicate more even profiles. The peaked profiles are given by the 20%, 50% and GM algorithms, the value of their kurtosis is less than 3.0 indicating the distribution of the temperature across the element is centred in the centre of the element.

The elements with more of the temperature distributed on the outsides of the element have a kurtosis more than 3, the methods that produced a optimised profile with this pattern were the GS and GT methods. These methods concentrate most of their treatment along the edges of the element indicating that the regions on the edges of the element receive greater treatment and thus become regions of higher heat production.

The quickest per cycle method is the 20% method. This is because the size of the treatment area is smaller, this is because the laser has to just raster over the lowest 20% of temperature which is usually centred on the edge of the element or grouped in the centre of the element after the initial cycles. This shows that the 20% method could be used in scenarios where the time of processing needs to be reduced above all other considerations.

In addition this is compounded by looking at the amount of cycles needed to reach a optimised profile. The 20% method takes the least time to reach an optimised profile whilst the 50% method takes the longest. The GS,GT and GM method take more cycles. The improvement per cycle is highest in the 20% method but the end result standard deviation improvement is lower than the GM and GT methods.

Within each cycle of ablation, the value of the standard deviation and the kurtosis changes due to the new temperature profile produced by the element. The standard deviation for the various processing methods after each cycle of ablation is shown in figure 5.31.

The standard deviation is illustrated relative to the initial standard deviation, this allows for easy comparison to see how the profile changes as a result. There is a trend of decline in the standard deviation across processing cycle up to a certain point. At this point the standard deviation starts to increase.

The standard deviation also oscillates as it decreases. The three repeats of the GT method shown with the dotted lines display the variance between the processing of the element. Due to the inherent difference in the raw elements different result can be obtained, which is shown in these dotted lines. The trend of oscillation of standard deviation follows a similar trend for the three GT methods. If all lines are compared against the abrasion method all significantly decrease the standard deviation of the elements except the 50% method which leads to a runaway of the standard deviation.

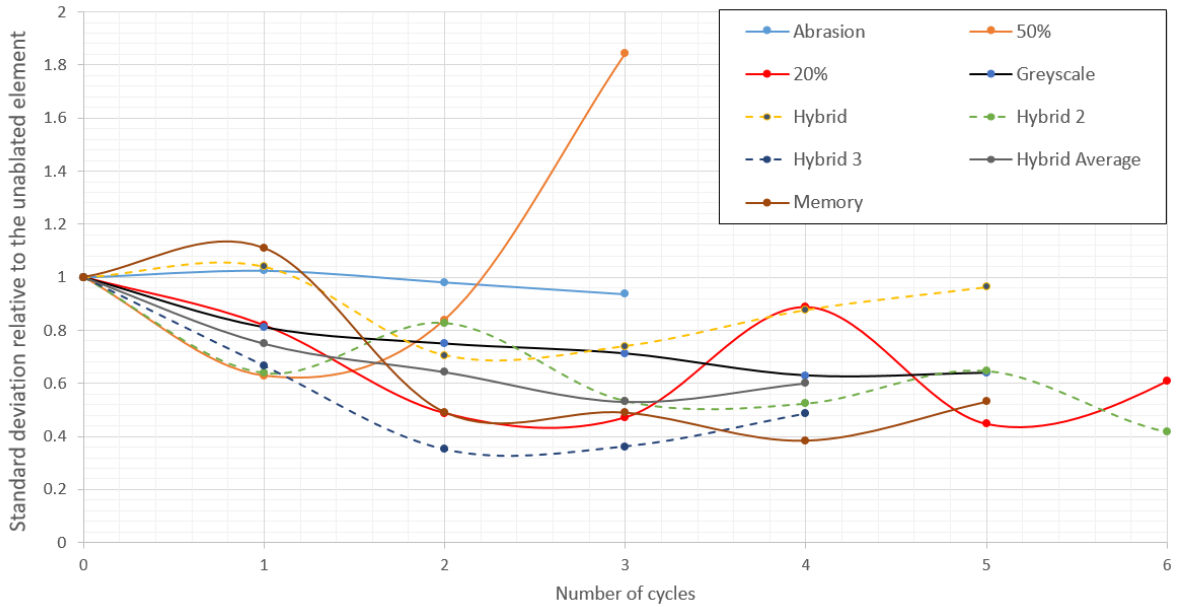


Figure 5.31: The standard deviation of the element after ablation relative to the unablated element.

The kurtosis of the elements is graphed along for each processing cycle. A kurtosis of 3 indicates an temperature distribution similar to a normal distribution. It can be seen here that the GS, GT and GM methods show a convergence towards a kurtosis of 3 after 4 cycles of ablation whereas the other profiles diverge substantially until decreasing towards a kurtosis of 3. The hypothesis is that optimal treatment means the kurtosis rises slowly towards ideal kurtosis value and then when the kurtosis becomes larger than 3 the distribution has achieved a normal distriution.

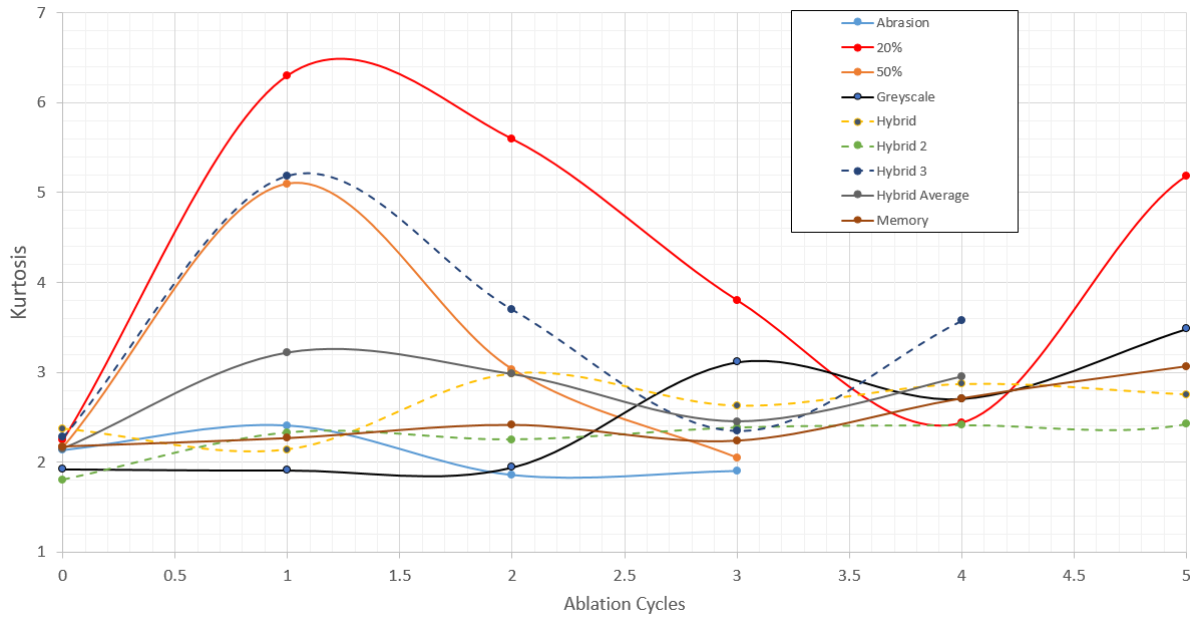


Figure 5.32: The kurtosis of each element after each cycle of ablation from various processing methods.

5.13.1 Resistance Change Through Various Processing Methods

The resistance change per cycle and the resistance of the optimised profile had been tabulated in 5.5, this shows that all methods drastically change the resistance of the elements. The Greyscale method shows the greatest change in the resistance of the element, this is due to the method ablating large portions of the element.

This was the motivation for the development of the GT method. The least change is seen from the GM and GT methods showing that the change within these methods to reduce the amount of treatment applied to the element was a success. These even have a lower resistance change than the abrasion method.

The resistance change of the various elements has been charted in figures 5.33 and 5.34.

Table 5.5: Change in resistance per cycle for various ablation processing methods

Method	Resistance change change per cycle (Ω)	Average Resistance when optimised (times initial resistance)
Greyscale (GS)	0.8	5.6
20% Threshold (20%)	0.6	3.2
50% Threshold (50%)	0.9	4.3
Abrasion (Ab)	0.4	1.8
Greyscale-Threshold(GT)	0.4	1.7
GT + Memory (GM)	0.4	1.6

The first graph compared the averaged fit of the resistance change of the elements in the GSH (GT) processing cycle. This shows how the fit of the average curve follows the trend of the increase in resistance of the data, with a variation after 5 cycles.

The second graph shows the change in resistance of all of the processing methods of the elements. The change in resistance indicates the amount of treatment given to the element from the laser as that is the primary objective of the laser process. The GS, 20% and 50% methods initially increase the resistance of the element by a large amount. Then the increase in resistance is small for a few cycles and then increases after four cycles.

In comparison the Abrasion, GM, and GT Avg methods increase the resistance of the elements slowly. This means that the treatment given in the latter processes is much lower than in the former processes. In addition there is a consistent increase to the resistance indicating a more appropriate treatment of the element by the laser processing. The GT and GM methods show a similar increase in the resistance of the element as in the abrasion methods.

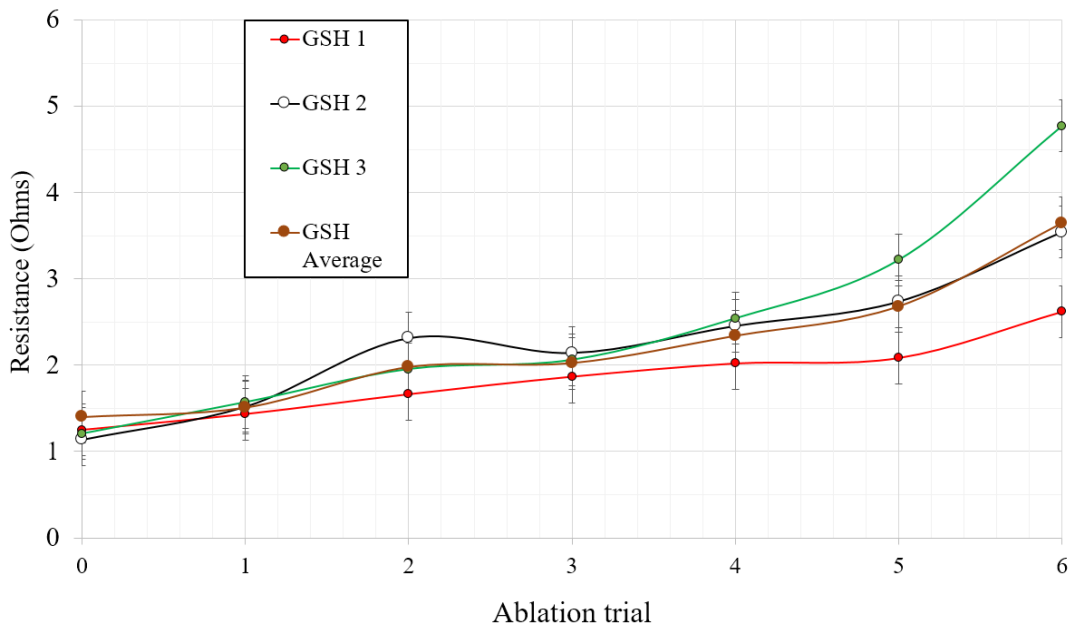


Figure 5.33: The electrical resistance of the device after ablation by the Greyscale Hybrid method in multiple trials with an averaged line added.

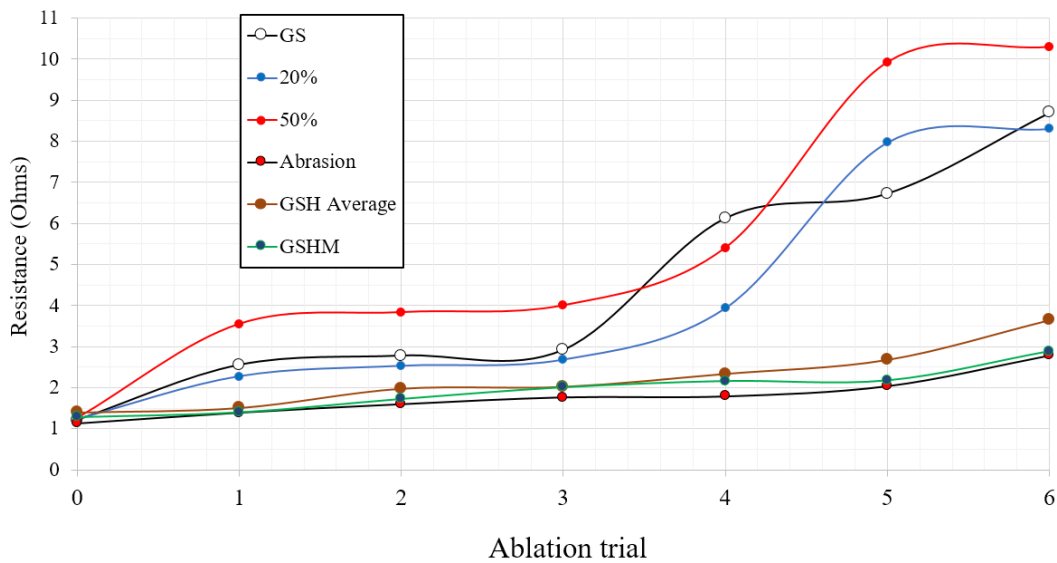


Figure 5.34: The electrical resistance of the device after each iteration of ablation by various processing methods.

5.14 Discussion of the Various Processing Methods

Within this section all of the various hypothesis and results are collated together to evaluate which processing methods are better suited to different circumstances.

It was found that the least successful method is the 50% method, as this produces a less uniform temperature distribution than the element displays at the start of the process. This is seen through the negative improvement value in the table of standard deviation improvements. The distribution of the less uniform temperature profile across the element is more even than in the original element as shown by the improvement in the kurtosis value; Although the kurtosis value of 2.08 indicates a peaked profile. In addition, the amount of cycles used is much larger than with other methods as this method is not converging the element sufficiently in each cycle to reach an optimised profile.

There is an argument that depending upon the application the 20% method or the GM method is the most successful. The case for the GM method's success is the achievement of the greatest improvement in the standard deviation in less processing cycles than the other greyscale methods, and the increase in total element resistance is less than for the other methods. There is also evidence that this method has the lowest chance of burnout production due to not developing high temperature hot spots. In addition, the GM method's kurtosis is the closest to the even level kurtosis of 3. This indicates that the temperature profile of the optimised element from the GM method produced the most even profile.

On the other hand the 20% method produces the greatest standard deviation improvement per processing cycle. In addition if the standard deviation improvement of the 20% method is within the acceptable limits of that elements application the 20% method is able to optimise the elements at the fastest rate. This is because the 20% method has the lowest processing time per cycle of all the elements.

The total time for optimisation scales linearly with the time for each processing cycle, this means that this method could save significant time. Although the results are worse. The 20% method also produced burnout after multiple ablations thus the method is likely, unless more work is done on its development to be a large factor in the choice of element as the destruction of the element can be a costly mistake.

The GS method ablates the whole area with only the very hottest of areas receiving no treatment. This means the element is over-treated across the whole area with the element becoming very thin and oxidised. The standard deviation improvement of the method was the lowest of the other methods that had a positive improvement. The kurtosis of the optimised profile of this method was 3.5 this indicates that the element has a temperature profile with the temperatures along the edges of the element higher than in the middle on average.

Chapter 6

Conclusion

This work investigated the CO₂ laser ablation of a Ni-Cr-Fe-O flame sprayed heating element film. The primary goal of this research was to develop various processing methods of automated laser ablation using infrared imaging to alter the surface of the element so its heat output, uniformity, and distribution of temperature across the element were improved.

This goal has been achieved through the development of the laser system and five distinct processing methods which improve the uniformity and distribution of temperature across the element from the element heating. In order to start to design the system the film properties were initially investigated.

The morphology of the film has been examined through the microscopy techniques described in the previous sections, and the changes due to the laser ablation processing methods have been tabulated. It was found that the film consisted of a 7% alloyed metal, 62% oxide, and 21% porous (by volume within the film) which matched the values obtained through other work reviewed in the literature section [2]. X-ray diffraction of the film confirmed that the element composition primarily consisted of a metallic phase (Fe-Ni-Cr) as well as an oxide phase (NiO).

The film was observed with an optical microscope from different angles. The cross sectional image analysis of the film cross sections suggested the film was 17% alloyed metal, 62% oxide, and 21% porous. The morphology of the structure of oxide and metallic regions shows the regions grouped into layers that were likely deposited through the flame spray. The upper surface of the film has an oxide layer on it developed through the cooling of the flame spray process. The polished scanning electron microscopy and optical microscopy of the polished face of the film shows that within the oxide regions there is a milky consistency of the metallic components running through the oxide.

The EDX maps confirmed that the lighter regions consisted of high proportions of Nickel and Iron whereas the oxide regions were confirmed to be the darker within the image. The chromium was shown to be distributed throughout the metallic and oxide regions, this was predicted by the theoretical model that the NiO lattice can absorb the Chromium ions on the interstitial site which is also found through work previously done on comparable films [2].

Through optical profilometry of the material surface the average roughness of the material has been found. The measurements indicated a significant variation of the element's profile height and therefore roughness. The root mean square of the surface height was found at 3.4 (μm), the focus depth of the laser was larger than this value which indicated the average height of the film was in the focus of the laser.

When investigating the morphology changes caused by the laser ablation, changes such as the melting of the surface and dross formation were identified. It was found that there was a reduction in the amount of voids within the film as the material appeared to have been melted within these regions.

The phase changes for the XRD measurements showed a trend towards a decrease in metallicity from the laser ablation and an increase in the oxidation of the film. This primarily affected the Nickel metallic regions as compared to the Iron and Chromium samples. The proposed hypothesis is that the nickel has a lower melting and boiling point so was thus ablated and oxidised in higher proportion. Parallels were found from the heat treatment in other work undertaken on the material where this change was also observed [2].

This was correlated with EDX images of the lines of ablation showing the decrease in the amount of Nickel in the laser tracks and an increase in the amount of oxides in this region providing further proof of this hypothesis. Through the connection to the properties of oxides and metals it was shown that this increase of oxidation decreased conductivity of the film around the laser tracks adding to the model of resistance increase through the laser ablation of the sample.

When the resistance increase of the sample was modelled, taking into account the resistance increase due to the thickness reduction of the conductor, and compared against the experimental results for the resistance increase, it was found that the resistance increase could not be caused solely by the thickness reduction of the conductor. To explain the resistance increase, the conductivity changes must also be taken into account.

This was compared to the optical, XRD and EDS measurements which confirmed the growth of the oxide regions around the laser ablated regions. It was found due to the in-homogeneity of the film and the response of the film to microsecond inferred pulsed radiation that a 'clean' processing method under the constraints of the project were not possible and instead developed a stochastic method to analyse and treat the film.

Evidence was found that the main current carrying material within the raw film was the Nickel and Iron in the regions of high metallicity. This evidence was provided through comparisons of the film component's electrical resistivity and the temperature dependence of the resistance of the element.

The electrical resistivity of Nickel Oxide samples was found through literature to be 10x that Nickel. The resistance-temperature dependence coefficient of the element was found $\alpha = 0.0057$. The value found for Nickel samples is 0.005 [11] which is much closer to the value than the value of 0.5 for Nickel Oxide [61].

This was used to create a laser processing strategy for the targeted laser ablation of the film. Since the Nickel is the primary current carrier material the maintenance of these current paths is crucial to avoid stopping the current flow through a region of the element.

This means that the pulsed ablation of the film is preferable to the continuous ablation with a matrix of holes in the element created so that the current paths can be maintained. Within these areas around the pulse regions and under the pulse region the current paths are reduced, thus, through the mechanisms outlined, the heat output within the region increases. Crucially, this method removes a minimum volume of material to affect the temperature profile and causes the minimum change in the film oxidation and resistance.

As a result of this laser processing strategy, the processing methods were designed to operate with multiple operation cycles with the minimum effect delivered to the element in each cycle. The principles of the processing method is that the processing time should be minimised, the amount of energy delivered and thus changes to the material minimised, and the uniformity of temperature profile optimised. In order to do so, five processing methods were produced that use a pulsed carbon dioxide laser to treat the element. The processing methods use infrared data from an infrared camera to determine the areas with the lowest heat output.

These areas are given a proportional treatment according to the processing method so that the local resistance of the cold area increases. Due to the higher resistance the cooler areas gain a higher proportion of the voltage applied over the element than before. This means the colder areas now have a higher proportion of heat production and thus reach a higher temperature than before. In addition, due to the lower volume of material in that area caused by the ablation treatment, less volume requires to be heated up so the ablated area reaches a higher temperature.

There are three types of processing methods developed. First, the threshold process which ablated all areas below either 20% or 50% percent of the maximum temperature reached by the device with a constant power and speed. Secondly, the Greyscale method which ablates the element in proportion to the temperature within that area. Finally the hybridised method of the Greyscale-hybrid method that alters the amount of treatment delivered within a set range of threshold (e.q targets the coolest 50%).

The processing methods were analysed by looking at the change in the element temperature profile after each treatment and looking at the change in resistance of the element. It was found that all methods improve the temperature profile of the elements except the 50% method. To quantify the difference between the improvements, two metrics were used, the standard deviation and the kurtosis. Standard deviation measures the uniformity of the temperature output and the kurtosis was used as a measure of the distribution of temperature output.

The greatest reduction in the standard deviation of the element's temperature profile is found in the Greyscale Threshold with memory method. The method generates a 71% reduction in the standard deviation of the temperature profile, through the kurtosis and contour imagery the method had the most uniform temperature distribution across its surface. This method showed evidence that its use leads to less burnouts on the element surface as it produced less high heat zones . Although this method takes the longest time per cycle, since the result achieved is the best this method is determined the optimal processing method. If the time reduction of the process is crucial then the 20% method and the GT methods provide alternatives.

6.1 Further Work to be Done

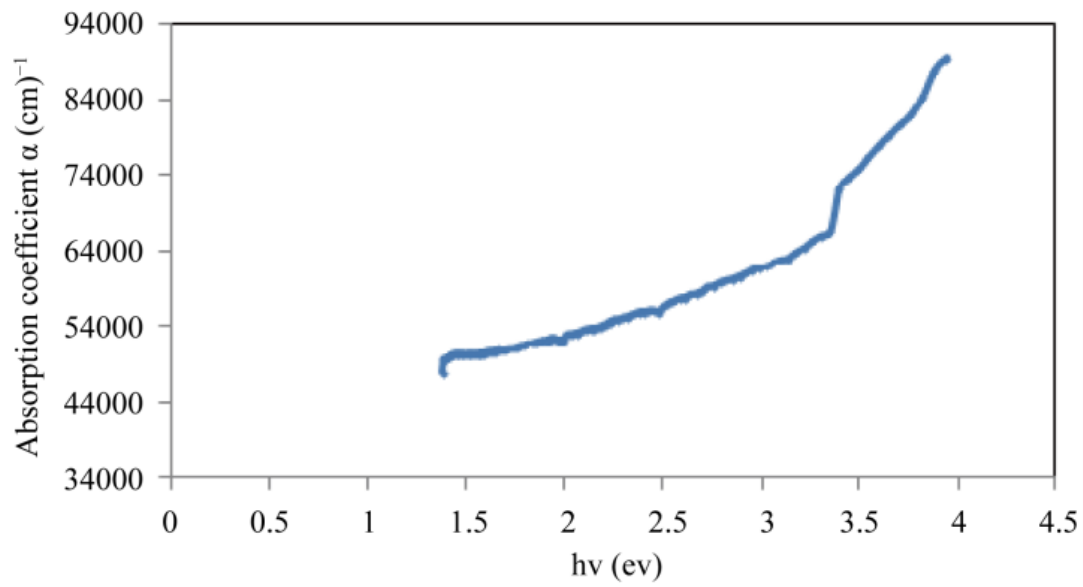
I have optimised only a selection of the possible combinations of factors affecting the processing of the element, these have been optimised towards the 40W laser system with only one element being processed at a time. It is likely that for a larger scale system a greater degree of optimisation of these factors will need to take place and due to the selection of devices in that system, the optimised system may look very different to the system described here. One example would be the use of a higher powered laser with a larger spot size to treat greater areas quicker, perhaps the use of a laser of different wavelength would give very different results as discussed in the laser theory section.

The effects of altering the range of laser would be very interesting to investigate in this material as the use of a UV laser has been shown to lead to a thermal processing [34]. The use of laser induced breakdown and Ramman analysis would provide some interesting results about some of the effects of the laser processing and provide some additional evidence of how the structure of the film changes after laser ablation.

In addition 2DHeat Ltd. are continually developing new films and structures; this provides a way to experiment and generalise the technique for different films. This would be useful so that the resistance alteration method can be generalised and so combined with their expertise of element production generate elements with a specific heat structure and a specific resistance. They are also experimenting with different geometries, the current implementation of the processing method cannot ablate areas with sections cut out, only rectangular polygons can be treated. The generalisation of the system to work with non trivial geometries would enhance this method, a possible route would be the identification of the element area with a visual camera which then feeds the data to the processing method.

Appendix A

Appendix

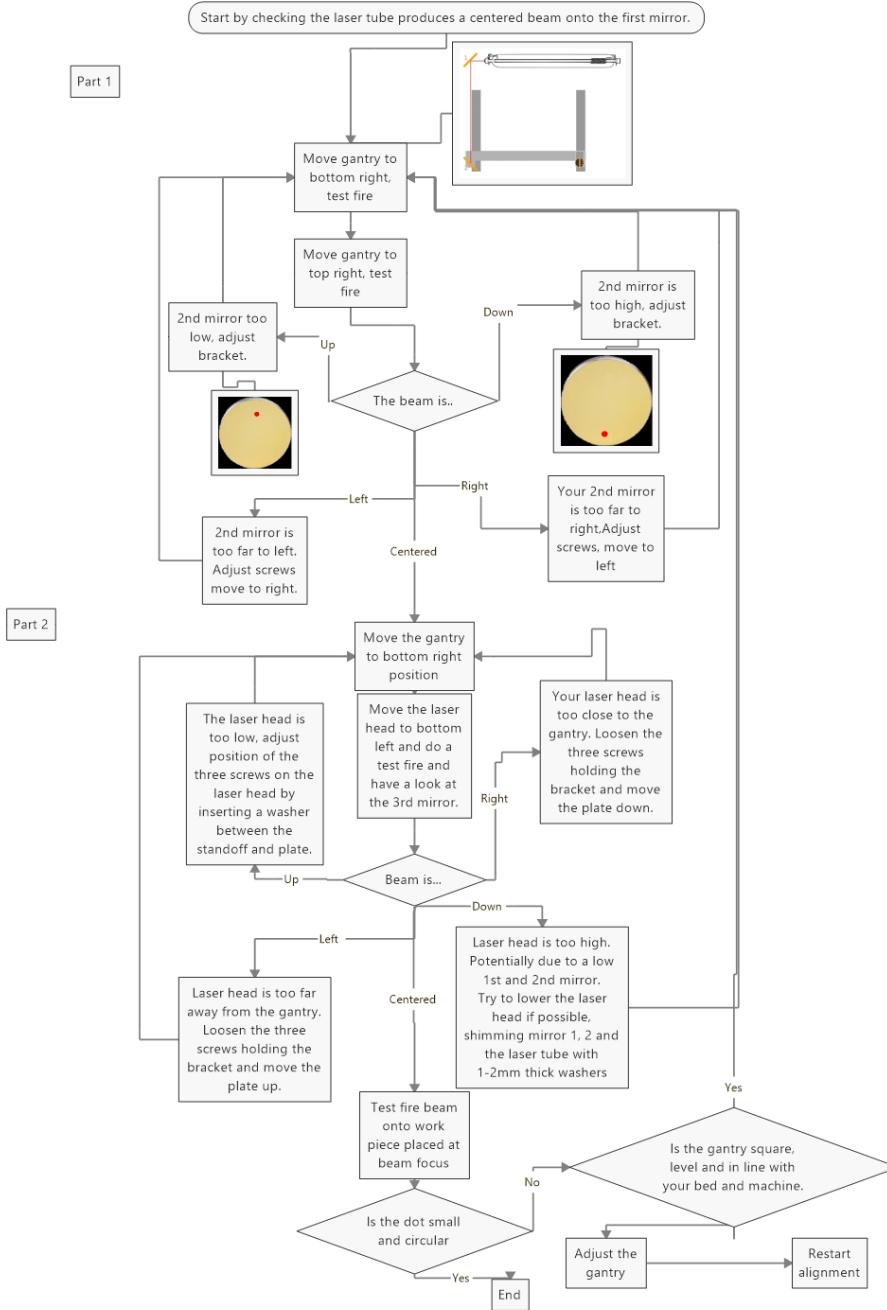


A1) Absorption of 200 μm NiO films to various wavelengths of light. [40]

A2)Tape placed over the mirror to carry out alignment tests.



A3) Laser alignment procedure.



Bibliography

- [1] Kemper Heiner, Lasi Hans-Georg. Recommendations for implementing the strategic initiative industrie 4.0. *Business & Information Systems Engineering*, 4 (6),:pp. 239–242, 2013.
- [2] Mark E. Duffield, Gordon J. Tatlock, and John F. Lewis. High-temperature decomposition of fe- and cr-doped nio produced by a novel flame spray technique. *Oxidation of Metals*, 88(3):351–360, Oct 2017. ISSN 1573-4889. doi: 10.1007/s11085-017-9747-z. URL <https://doi.org/10.1007/s11085-017-9747-z>.
- [3] Department for Business, Energy & Industrial Strategy. *Energy Consumption in the United Kingdom-2017*. United Kingdom Government, 01 2018.
- [4] Pachauri Rajendra. *Global warming of 1.5°C*. Intergovernmental Panel on Climate Change, 2018.
- [5] Department for business, Energy & Industrial strategy. *United Kingdom Energy statistics 2017*.
- [6] Clifford Tennenhouse. Design and maintenance of electric heating elements. *Industrial Heating*, 67(1):34, 01 2000. URL <https://search-proquest-com.ezproxy.lancs.ac.uk/docview/217252089?accountid=11979>.

- [7] ASM International and the Thermal Spray Society. *Handbook of Thermal Spray Technology*. ASM International, 2011.
- [8] Satoshi Sasaka and Kiyoshi Fujino. X-ray determination of electron-density distributions in oxides, mgo, mno, coo, and nio, and atomic scattering factors of their constituent atoms. *Proceedings of the Japan Academy, Series B*, 55(2):43–48, 1979. doi: 10.2183/pjab.55.43.
- [9] S Mrowec and Zbigniew Grzesik. Oxidation of nickel and transport properties of nickel oxide. *J. Phys. and Chem. Solids*, 65:1651–1657, 10 2004. doi: 10.1016/j.jpcs.2004.03.011.
- [10] Karl Hauffe. *The Mechanism of Oxidation of Metals—Theory*. Springer US, Boston, MA, 1995. ISBN 978-1-4684-8920-0. doi: 10.1007/978-1-4684-8920-0_3. URL https://doi.org/10.1007/978-1-4684-8920-0_3.
- [11] A. Atkinson, R. I. Taylor, and P. D. Goode. Transport processes in the oxidation of ni studied using tracers in growing nio scales. *Oxidation of Metals*, 13(6):519–543, Dec 1979. ISSN 1573-4889. doi: 10.1007/BF00812776. URL <https://doi.org/10.1007/BF00812776>.
- [12] Mark Duffield. *Novel metal-metal oxide thick film heating elements produced by dual-stage flame spray processing of a gas atomised Ni-Cr-Fe alloy*. PhD thesis, University of Liverpool, 2017.
- [13] V Raghavan. Fe-ni-o (iron-nickel-oxygen). *Journal of phase equilibria and diffusion*, 31(4):369–371, 2010.

- [14] Lina Kjellqvist, Malin Selleby, and Bo Sundman. Thermodynamic modelling of the cr-fe-ni-o system. *Calphad*, 32(3):577 – 592, 2008. ISSN 0364-5916. doi: <https://doi.org/10.1016/j.calphad.2008.04.005>. URL <http://www.sciencedirect.com/science/article/pii/S0364591608000230>.
- [15] R. D. Shannon. Revised effective ionic radii and systematic studies of interatomic distances in halides and chalcogenides. *Acta Crystallographica Section A*, 32(5):751–767, Sep 1976. doi: 10.1107/S0567739476001551. URL <https://doi.org/10.1107/S0567739476001551>.
- [16] The Engineering Toolbox. Thermal Conductivity of Metals, Oxides and Alloys. Available at https://www.engineeringtoolbox.com/thermal-conductivity-metals-d_858.html (23 October 2018), 2018.
- [17] David J Griffiths. *Introduction to electrodynamics; 4th ed.* Pearson, Boston, MA, 2013. URL <https://cds.cern.ch/record/1492149>. Re-published by Cambridge University Press in 2017.
- [18] B Sasi, K.G Gopchandran, P.K Manoj, P Koshy, P Prabhakara Rao, and V.K Vaidyan. Preparation of transparent and semiconducting nio films. *Vacuum*, 68(2):149 – 154, 2002. ISSN 0042-207X. doi: [https://doi.org/10.1016/S0042-207X\(02\)00299-3](https://doi.org/10.1016/S0042-207X(02)00299-3). URL <http://www.sciencedirect.com/science/article/pii/S0042207X02002993>.
- [19] C. Breck Hitz. *Introduction to laser technology [electronic resource]*. John Wiley & Sons, Hoboken, 4th ed. edition, 2012. ISBN 9781118219461.
- [20] Wikipedia. Gaussian beam. Available at https://en.wikipedia.org/wiki/Gaussian_beam Licensed under the Creative Commons Attribution-Share Alike 3.0 (23 October 2018), 2018.

- [21] J. (John) Wilson. *Lasers, principles and applications*. Prentice Hall international series in optoelectronics. Prentice Hall, New York, 1987. ISBN 0135236975.
- [22] J Palmer and I Cooper. *United Kingdom:Housing energy fact file*. Department for Energy and Climate Changes, 2013.
- [23] J. Dutta Majumdar and I. Manna. Laser processing of materials. *Sadhana - Academy Proceedings in Engineering Sciences*, 28(3-4):495–562, 2003. ISSN 02562499.
- [24] Laser Institute of America and Magnolia Publishing. *LIA handbook of laser materials processing*. Laser Institute of America, 2001. ISBN 0912035153.
- [25] Karl-Heinz Leitz, Benjamin Redlingsh ufer, Yvonne Reg, Andreas Otto, and Michael Schmidt. Metal ablation with short and ultrashort laser pulses. *Physics Procedia*, 12:230 – 238, 2011. ISSN 1875-3892. doi: <https://doi.org/10.1016/j.phpro.2011.03.128>. URL <http://www.sciencedirect.com/science/article/pii/S1875389211002070>. Lasers in Manufacturing 2011 - Proceedings of the Sixth International WLT Conference on Lasers in Manufacturing.
- [26] *Laser Materials Processing*. McGraw-Hill, 2015. ISBN 9780071839778. URL http://search.credoreference.com/content/entry/mhmeh/laser_materials_processing/0.
- [27] R. Indhu, V. Vivek, L. Sarathkumar, A. Bharatish, and S. Soundarapandian. Overview of laser absorptivity measurement techniques for material processing. *Lasers in Manufacturing and Materials Processing*, 5(4):458–481, Dec 2018. ISSN 2196-7237. doi: 10.1007/s40516-018-0075-1. URL <https://doi.org/10.1007/s40516-018-0075-1>.

- [28] Irving Langmuir. Oscillations in ionized gases. *Proceedings of the National Academy of Sciences*, 14(8):627–637, 1928. ISSN 0027-8424. doi: 10.1073/pnas.14.8.627. URL <https://www.pnas.org/content/14/8/627>.
- [29] H.J. Raterink. Physical processes in laser-materials interactions. *Optica Acta: International Journal of Optics*, 31(1):4–5, 1984. doi: 10.1080/713821402. URL <https://doi.org/10.1080/713821402>.
- [30] W. M Steen. *Laser material processing [electronic resource]*. Springer, London ; Dordrecht ; Heidelberg ; New York, 4th ed. edition, 2010.
- [31] Henning Klank, Jǎúrg P. Kutter, and Oliver Geschke. Co2-laser micromachining and back-end processing for rapid production of pmma-based microfluidic systems. *Lab Chip*, 2:242–246, 2002. doi: 10.1039/B206409J. URL <http://dx.doi.org/10.1039/B206409J>.
- [32] A. Cser and A. Otto. Analysis and modeling of laser beam melt ablation. In Elso Kuljanic, editor, *AMST'05 Advanced Manufacturing Systems and Technology*, pages 397–402, Vienna, 2005. Springer Vienna. ISBN 978-3-211-38053-6.
- [33] Abubaker Hamad. *Effects of Different Laser Pulse Regimes (Nanosecond, Picosecond and Femtosecond) on the Ablation of Materials for Production of Nanoparticles in Liquid Solution*, page 21. Taylor & Francis, 09 2016. doi: 10.5772/63892.
- [34] Ashish Chhaganlal Gandhi and Sheng Yun Wu. Strong deep-level-emission photoluminescence in nio nanoparticles. *Nanomaterials*, 7(8), 2017. ISSN 2079-4991. doi: 10.3390/nano7080231. URL <http://www.mdpi.com/2079-4991/7/8/231>.

- [35] Ming He and Toh-Ming Lu. *Metal–Dielectric Diffusion Processes: Fundamentals*, pages 11–22. Springer New York, New York, NY, 2012. ISBN 978-1-4614-1812-2. doi: 10.1007/978-1-4614-1812-2_2. URL https://doi.org/10.1007/978-1-4614-1812-2_2.
- [36] M. Cerchez, M. Swantusch, M. Toncian, X. M. Zhu, R. Prasad, T. Toncian, Ch. RĂúdel, O. JĂd'ckel, G. G. Paulus, A. A. Andreev, and O. Willi. Enhanced energy absorption of high intensity laser pulses by targets of modulated surface. *Applied Physics Letters*, 112(22), 2018. ISSN 0003-6951.
- [37] David Bergström. *The absorption of laser light by rough metal surfaces*. PhD thesis, Luleå tekniska universitet, 2008.
- [38] Zhanliang Sun, Matthias Lenzner, and Wolfgang Rudolph. Generic incubation law for laser damage and ablation thresholds. *Journal of Applied Physics*, 117:073102, 02 2015. doi: 10.1063/1.4913282.
- [39] Chanae Park, Juhwan Kim, Kangil Lee, Suhk Oh, Hee Jae Kang, and Nam Seok Park. Electronic, optical and electrical properties of nickel oxide thin films grown by rf magnetron sputtering. *Applied Science and Convergence Technology*, 24:72–76, 05 2015. doi: 10.5757/ASCT.2015.24.3.72.
- [40] R. Newman and R. M. Chrenko. Optical properties of nickel oxide. *Phys. Rev.*, 114:1507–1513, Jun 1959. doi: 10.1103/PhysRev.114.1507. URL <https://link.aps.org/doi/10.1103/PhysRev.114.1507>.
- [41] Bureau of Industry and Security. *Export Control Classification Number 6A993*. Government of the United States of America, 01 2018.
- [42] H. Stanjek. Basics of x-ray diffraction. *Hyperfine Interactions*, 154(1):107–119, 2004. ISSN 0304-3843.

- [43] Dongyue Wang Min Yao and Min Zhao. Element analysis based on energy-dispersive x-ray fluorescence. *Advances in Materials Science and Engineering*, pages 495–562, 2015.
- [44] K. M. Knowles. Electron microscopy and analysis. *Journal of Microscopy*, 203(2):232–233, 2001. doi: 10.1046/j.1365-2818.2001.0936b.x. URL <https://onlinelibrary.wiley.com/doi/abs/10.1046/j.1365-2818.2001.0936b.x>.
- [45] Wikipedia. Electron Microscopy. Available at https://commons.wikimedia.org/wiki/File:Electron_Interaction_with_Matter.svg Licensed under the Creative Commons Attribution-Share Alike 3.0(23 October 2018), 2018.
- [46] Wikipedia. Scanning Electron Microscope. Available at [https://commons.wikimedia.org/wiki/File:Schema_MEB_\(en\).svg](https://commons.wikimedia.org/wiki/File:Schema_MEB_(en).svg) Licensed under the Creative Commons Attribution-Share Alike 3.0 (23 October 2018).
- [47] Lawrence L Lapin. *Modern engineering statistics*. Duxbury Press, Belmont, CA, 1996. ISBN 0534508839.
- [48] Richard B. Darlington. Is kurtosis really peakedness? *The American Statistician*, 24(2):p19–22, 1970. doi: 10.1080/00031305.1970.10478885. URL <https://doi.org/10.1080/00031305.1970.10478885>.
- [49] Wikipedia. Kurtosis. Available at <https://en.wikipedia.org/wiki/Kurtosis> Licensed under the Creative Commons Attribution-Share Alike 3.0 (23 October 2018), 2018.
- [50] William L. Wolfe. *Introduction to Infrared System Design*. SPIE, 1996. ISBN 978-0-8194-2106-7. URL <https://app.knovel.com/hotlink/toc/id:kpIISD0005/introduction-infrared/introduction-infrared>.

- [51] Honeywell Inc, G.G. Gubareff, J.E. Janssen, and R.H. Torborg. *Thermal Radiation Properties Survey: A Review of the Literature*. Honeywell Research Center ; Minneapolis-Honeywell Regulator Company, 1960. URL <https://books.google.co.uk/books?id=6wKHQgAACAAJ>.
- [52] Gregory K. McMillan. *Advanced temperature measurement and control*. International Society of Automation, Research Triangle Park, NC, second edition. edition, 2011. ISBN 9781937560775.
- [53] R. Keys. Cubic convolution interpolation for digital image processing. *IEEE Transactions on Acoustics, Speech, and Signal Processing*, 29(6):1153–1160, 1981. ISSN 0096-3518. doi: 10.1109/TASSP.1981.1163711.
- [54] H. Hou. Cubic splines for image interpolation and digital filtering. *IEEE Transactions on Acoustics, Speech, and Signal Processing*, 26(6):508–517, 1978.
- [55] Scorchworks. K40 Whisperer software. Available at <http://www.scorchworks.com/K40whisperer/k40whisperer.html> (23 October 2018), 2018.
- [56] Feng-Bin Sun, Steve Lock, and Wendai Wang. Duty cycle definition and application in reliability engineering – a unified review, classification, and clarification.(correction notice). *International Journal of Reliability, Quality and Safety Engineering*, 20(05), 2013. ISSN 0218-5393.
- [57] LBP Optics. Reflectance of molybdenum mirrors. Available at <http://www.lbp.co.uk/materials/molybdenum.html> (23 October 2018), 2018.
- [58] THOR Laboratories. Zese lens transmission to infrared. Available at <https://www.thorlabs.com/tutorials.cfm?tabID=ba49b425-f85b-4549-8c1a-f111ddbb9099> (23 October 2018), 2018.

- [59] Manoj Kumar, A.K. Biswas, Pankaj Bhargav, T. Reghu, Shashikiran Sahu, J.S. Pakhare, M.S. Bhagat, and L.M. Kukreja. Theoretical estimation and experimental studies on gas dissociation in tea co2 laser for long term arc free operation. *Optics & Laser Technology*, 52:57 – 64, 2013. ISSN 0030-3992. doi: <https://doi.org/10.1016/j.optlastec.2013.04.006>. URL <http://www.sciencedirect.com/science/article/pii/S0030399213001254>.
- [60] Glynis C. Lough, James J. Schauer, June-Soo Park, Martin M. Shafer, Jeffrey T. DeMinter, and Jason P. Weinstein. Emissions of metals associated with motor vehicle roadways. *Environmental Science & Technology*, 39(3):826–836, 2005. doi: 10.1021/es048715f. URL <https://doi.org/10.1021/es048715f>. PMID: 15757346.
- [61] R. Newman and R. M. Chrenko. Optical properties of nickel oxide. *Phys. Rev.*, 114: 1507–1513, Jun 1959. doi: 10.1103/PhysRev.114.1507. URL <https://link.aps.org/doi/10.1103/PhysRev.114.1507>.